UNIVERSITY OF TRENTO

Doctoral School in Civil, Environmental and
Mechanical Engineering

Curriculum 3. Modelling and Simulation

Ilaria Corridori

Mechanics of biofunctionalised bioconducting microfibres for the treatment of spinal cord injury

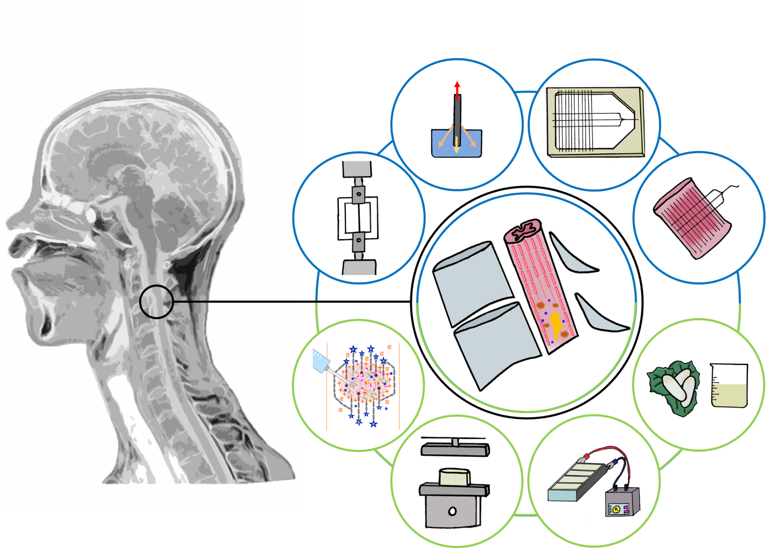

2021 - Doctoral thesis

UNIVERSITY OF TRENTO - Italy
Department of Civil, Environmental and Mechanical Engineering

Doctoral School in Civil, Environmental and Mechanical Engineering
Topic 3. Modelling and Simulation - XXXIII cycle 2017/2021

Doctoral Thesis - November 2021

Ilaria Corridori

Mechanics of biofunctionalised bioconducting microfibres for the treatment of spinal cord injury

Supervisors
Nicola M. Pugno, University of Trento
Antonella Motta, University of Trento

To my family

Acknowledgements

During the years of Doctorate School, I met several persons that I would like to thank, who drove, inspired, and mentored me in the difficult but beautiful path of research.

Thanks to prof. Nicola Pugno and prof. Antonella Motta for supervising and guiding me throughout the Doctorate and this work of thesis.

Thanks to prof. Claudio Della Volpe and prof. Claudio Migliaresi for the precious support and suggestions.

Thanks to Dr. Maria Fiorella Pantano, Dr. Diego Misseroni, Dr. Gianluca Costagliola, and prof. Maniglio for the help and discussions.

Thanks to prof. Federico Boschi and prof. Alessandro Daducci for encouraging me moving the first steps in research.

Thanks to Elena, who is always willing to listen and help.

Thanks to Sara, my images expert.

Thanks to Alice, who has always time for me.

Thanks to all my colleagues who are now friends, that took this path with me and made it better.

Finally, I gratefully acknowledge who was there for me when I needed, and especially when I thought I did not need it.

Thanks to Emily and Paola, with who I share the best times since kindergarten.

Thanks to Claudia, Michele, and my high school friends, who make me laugh like no one else.

Thanks to Sara and Anna, my adventures partners in the everyday life and around the world.

Thanks to Alice, who is a precious listener.

Thanks to Tiziano, who gave me the strength when I needed it.

Thanks to my Mum and Dad, who are always ready to push and catch me.

Thanks to Federico, my wise brother and forever solace.

Table of contents

List of Figures

List of Tables

Abstract

Spinal cord injury causes the partial or total loss of the anatomical and functional continuity of the spinal cord tissue, leading to the damage of the organs controlled by nerves that branch off downstream the injury. This thesis analyses the mechanics of two possible treatments based on two different approaches: intraspinal microstimulation and tissue engineering. These two approaches have a common rationale, the delivery of electrical stimuli to the injured spinal cord.

Intraspinal microstimulation (ISMS) is a promising technique for the treatment of spinal cord injury. The technique is based on a device composed of interconnected electrodes (i.e., microfibres) implanted in the injured spinal cord and connected to an external electrical generator. This external component produces electrical stimuli, that are delivered to specific neural networks through the electrodes.

A comprehensive study of the mechanics of an innovative device for intraspinal stimulation developed within the European project “Neurofibres” is performed, aiming at providing a comprehensive method for the evaluation of the mechanical performance of electrodes for ISMS before the final implantation. The electrodes are usually implanted perpendicularly to the longitudinal axis of the spinal cord, and thus the stiffness is the mechanical property considered in the literature to evaluate the feasibility and the correct targeting of the specific regions. The mechanical validation of the electrodes is then focused on the step after the implantation, considering the interplay with the surrounding tissue. In this work, the mechanical performance of the electrodes, useful for the selection of the best candidate, is evaluated thoroughly before the in vivo step, to avoid the waste of material, animals, and time.

The study involves the characterisation of the single components (electrodes) of the device, prototypes of the device, and the interplay between the device and the embedding spinal cord matrix. Tensile tests were performed on different types of bare and coated microfibres, and an analytical description of practical issues is proposed. The data obtained with the experimental and analytical studies were used to define a method to evaluate the mechanical performance of the electrodes and identify the best one. Changes in the bulk and surface properties after coating fibres were also found.

An experimental and theoretical study describes the behaviour of single and multiple interconnections between microfibres.

The possible failure mechanisms of the intraspinal microstimulation device and its components caused by the interplay with the surrounding embedding matrix are outlined. Experimental measurements were performed to make a qualitative and quantitative description of possible dangerous conditions, such as the breakage of the device due to physiological movements of the spine, the migration of the electrodes, and the dislocation of the device due to applied external forces.

A work on silk fibroin hydrogels for the regeneration of the spinal cord is also presented. The final aim of this work is the production of fibroin piezoelectric hydrogels capable of imposing electrical stimuli to the injured spinal cord, avoiding an external generator. Silk fibroin is largely used in tissue engineering due to its easy processability, biocompatibility, biodegradability, that guarantee a highly versatile material for biomedical purposes. Since structures with soft mechanical properties and high deformability are suitable for specific biomedical applications, silk fibroin hydrogels are studied in the regeneration of the central nervous system, blood, and skin. High water content, gas, and nutrients exchanged, an increased cell-cell interaction, and the tuneable mechanical properties are some of the features that encourage the use of hydrogels in tissue engineering and spinal cord regeneration.

Electrical stimulation was proven useful to achieve a favourable environment for the regeneration of the spinal cord after injury. The different approaches studied in literature often require the use of implanted electrodes to reach specific neural circuits, and external devices to generate the electric stimulation. Thus, the presence of an intrinsic current or a voltage produced during small deformations of the material in contact with the spinal cord tissue could avoid external stimuli supply. The piezoelectricity of silk was proven due to the overall β-sheets content and the uniaxial molecular alignment. However, in very few cases the piezoelectricity of hydrogels was studied and evaluated for the regeneration of the spinal cord.

This work aims to study the mechanical properties of a silk fibroin hydrogel obtained by applying an electric field to silk fibroin solutions, to investigate the eventual increase of the microstructure orientation and consequent improvement of the piezoelectric effects of silk. An ad hoc experimental setup was built to stimulate silk fibroin solutions with different electrical fields. Changes in the mechanical properties were reported, and further analyses are needed to evaluate the causes of these modifications.

Graphical abstract

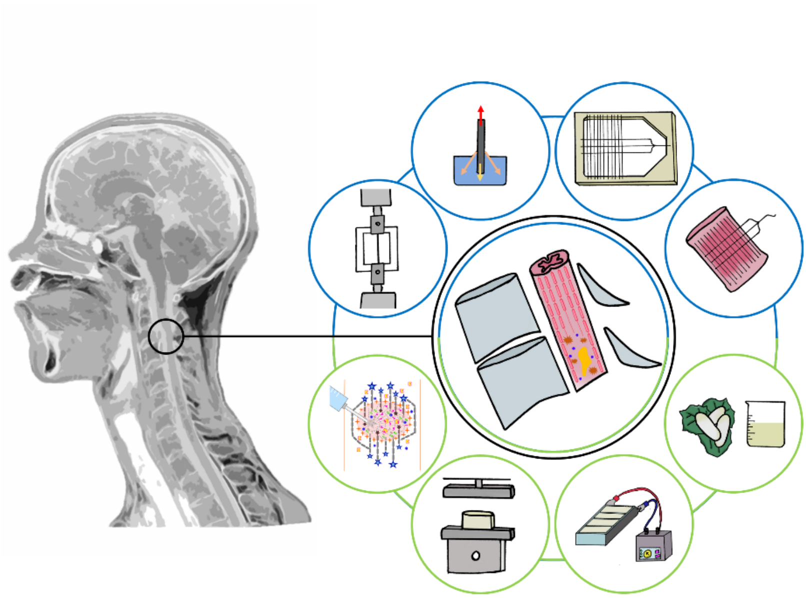

Introduction

Every year in the world, from 250˙000 to 500˙000 people suffer from spinal cord injury (SCI) [1]. Vehicle crashes, falls, acts of violence, and sports/recreation activities are the main causes of injury [2], but non-traumatic spinal cord injuries exist either. Spinal cord injury is not in the top ten causes of death [3], nevertheless, respiratory infections are only an example of the many complications due to spine lesions and the third cause of death in 2016 [3].

The demand for an effective treatment for SCI was analysed from an economic point of view. The lifetime cost of a spine injured patient varies with the age and the severity of the lesion, but still ranges between 4.9 (high tetraplegia, 25 years old) and 1.2 (motor functional at any level, 50 years old) millions of dollars per year [2]. These calculations include health care costs and living expenses; indirect costs (losses in wages, fringe benefits, and productivity) are not considered. However, after decades of intense research activities, a gold standard for the treatment of this pathology has not been defined yet [4].

Many reasons made this goal extremely difficult. First, the central nervous system has a very low regenerative potential. Furthermore, SCIs lead to the development of a hostile environment for the intrinsic healing mechanisms of the tissue. In addition, the formation of fibrotic tissue creates impenetrable barriers for axon regrowth [5]. Suddenly after injury, the physiological tissue regeneration begins but a degenerative aggressive environment leads to poor regrowth of axons, migration of neural cells, and neurites outgrowth [6]. Spinal injuries cause the partial or total loss of anatomical and functional continuity of the spinal cord tissue.

Therapies in use try to contrast the degenerative process and address tissue dynamics toward a proper regeneration. Conventional therapies include surgical decompression, therapeutic hypothermia, and pharmacotherapy with the use of anti-apoptotic, anti-inflammatory, and anti-oxidation drugs [4].

To date, neuro-regenerative strategies include cell-based therapies (cell delivery and cell therapy), as well as implantable synthetic and biological scaffolds [4], [7].

Microfibres (MFs) are now intensively studied for the regeneration of the spinal tissue [8]–[10]. This approach has shown many advantages in the regeneration of the spinal cord. MFs create a bridge along the injury reconnecting the functional upstream and downstream sections of the spinal cord [9]. Their geometry and dimensions support axons and neurites' growth. Biofunctionalising the surface of the MFs, migration of glial cells and neurons was reported [11].

Collagen MFs engrafted with neural stem/progenitor cells have been studied as a biocompatible and biodegradable scaffold for neural tissue regrowth [12]. Local drug delivery was investigated employing microfibrous patches capable of a systematic and slow release of an anti-inflammatory and cyclic adenosine monophosphate, preserving small molecules [13]. Paclitaxel incorporated in poly L-lactic acid (PLA) MFs have been studied in vitro to improve axons regrowth across the injured area [14]. Bare PLA MFs obtained better outcomes in terms of spinal tissue re-healing when compared with film controls [8]. However, even if MFs seem a promising solution for the treatment of SCI, the obtained results are not optimal. Indeed, motoneurons regrowth has not been achieved yet, pointing out that something more than mechanical, biological, and chemical stimuli is needed.

Several studies proved that the electrical stimulation of the neural tissue supported the anatomical and functional recovery after SCI [15], [16]. Through the application of weak electric fields, direct current fields, and oscillating fields, several studies showed an increase in axons and neurites growth and regeneration after an injury. The rationale of these studies was the presence of extracellular voltage gradients in the physiological environment of the central nervous system during the development in the first stages of life [17].

The electrical stimulation is thus studied to achieve a favourable environment for regeneration after the loss of functional and structural continuity due to SCI through different approaches, such as Functional Electrical Stimulation (FES) and ISMS.

Intraspinal microstimulation (ISMS) is a promising technique to restore tissue continuity and thus achieving the functional regeneration of the spinal cord after an injury [18]–[20]. This technique aims to deliver electrical stimuli to specific neural networks below the injured area [1]. As a result of ISMS, motor functions [6], [18], bladder voiding [21], and resetting of the respiratory functions [22] were achieved after spinal cord injury (SCI).

The ISMS is performed through devices composed of microfibres (MFs)-electrodes that are inserted below the damaged area and provide electrical stimuli to the tissue. These electrodes are connected to an external component capable of generating electrical signals with specific frequencies and amplitudes [15].

An innovative ISMS device has been studied in Neurofibres project (www.neurofibres.eu), funded by the European Commission under the H2020-FETPROACT-01-2016 call (grant number 732344). The goal of the project is the design and the development of a new implantable device for the treatment of spinal cord injuries. This device combines electrical stimuli and regenerative medicine, applying the innovative approach of inserting the electrodes parallel to the longitudinal axis of the spinal cord, thus bridging the gap produced by the injury [9], [24]. Once implanted, the material, the shape, and the stimuli imposed by the device bridges the injured area and permit the regrowth of the axons [9]. The Neurofibres ISMS device is composed of microfibres-electrodes, that are planned to be interconnected through microwires to link the implanted device with the external generator of electrical stimuli. The project is positioned in TRL 3 (experimental proof of concept) and is designed from the type of electrodes to the type of interconnections. The University of Trento focussed on the work package concerning the mechanical characterisation of the device and its components. Thus, the presented work, developed within this Ph.D. thesis, followed the tasks and milestones defined in the work package.

The mechanical behaviour of the device must be comprehensively studied to design and develop a structure with high performance, efficacy, and efficiency. To obtain a comprehensive mechanical characterisation of the device, a hierarchical approach was used. Starting from the single components, moving to the prototypes of the device, and finally studying the interactions between the device and the surrounding environment enables the complete mechanical description of the proposed solution.

Different types of microfibres are available for ISMS purposes [18]–[20]. To evaluate which microfibre is the most suitable for the Neurofibres device, each mechanical property is considered. The project requirements included robust microfibres capable to be inserted in the stumps upward and downward the damaged area. The literature is focused on the mechanical validation of the electrodes through their interplay with the surrounding tissue [18], [21], [22], but a first evaluation could be performed before the in vivo steps. avoiding the waste of material, animals, and time. The method here proposed is based on experimental data and analytical calculations, creating a comprehensive evaluation of the mechanical performance of the electrodes by considering the standard mechanical properties and ad hoc calculated practical properties. Tensile tests on microfibres were performed to obtain their mechanical characterisation. Analytical models were developed to describe possible issues when handling and implanting the electrodes. Then, all the collected data were summarised in a table, in which every potential electrode was reported, and related properties, highlighting the best-achieved performances to obtain the optimal candidate for the device.

The performance of the electrodes could be improved by specific coatings. The possible changes in the bulk and surface properties were here analysed in the case of carbon microfibres coated with graphene. The mechanical properties of the fibres were measured with tensile tests. The surface energy of the fibres was calculated using the Wilhelmy balance method [25], [26] combined with the Lewis acid/base multicomponent approach [27].

A step forward in the investigation of the mechanical performance of the device was made by characterising the behaviour of several prototypes under tensile loads. These prototypes were characterised by different combinations of electrodes (i.e., different materials) and interconnections (i.e., connection techniques).

Once the device and its components were described from a mechanical point of view, an analysis of the interplay between the device and the surrounding environment was performed. The ISMS device must be implanted in the damaged spinal cord and will be thus subjected to external stimuli, such as physiological body movements (bending, traction, etc.), vibrations, heart beating, variable chest pressure, cellular processes associated with tissue healing. These micro and macro movements could cause the failure of the device and consequent partial or total failure of the treatment. Three different failure mechanisms were identified and analysed: the failure of the device due to the imposed strains, the dislocation of the electrodes, and the device-surrounding matrix debonding.

The failure of the device due to the physiological movements of the spine was studied comparing the strain calculated from the tensile tests on the prototypes with the strain reachable by the different portions of the spinal cord [28]. The second failure mechanism here considered was a direct consequence of the first: the migration of the implanted electrodes. To study this phenomenon, an ad hoc experimental setup was designed and developed to simulate small movements of the spine and to study the effect of the embedded electrodes. The last considered failure mechanism was the possible pull-out of the device from the implant site. Indeed, the device is designed to be connected to the external environment with a wire, and its pull-out is a possibly dangerous condition.

A fundamental feature of the Neurofibres device is the capability of imposing electrical stimuli. The effects of weak electric fields, oscillating fields, and direct current fields were studied on the functional and anatomical regeneration of neural tissue, resulting in the favourable environment for the restoration of specific functions [24], [29], [30]. Literature shows the need for an external device to impose the electrical stimuli to the electrodes and consequently to the neural tissue [16]. The connection with the environment and the generator necessitates further wires and connectors that are susceptible to many risks, such as the joints between different wires or possible bacterial attacks. A possible alternative solution, which avoids external connections, was studied, by exploiting the intrinsic piezoelectricity of *Bombyx mori* silk [31]. *Bombyx mori* silkworm silk can increase in crystallinity and high orientation with a high degree of β-sheet [32]. Silk fibroin *Bombyx mori* is a fibrillar protein composing the core part of the silkworm filament, and many techniques have been studied to improve the β-sheet crystallinity [32]–[34]. This work focused on the production of silk fibroin hydrogels to obtain structures suitable for neural tissue applications [35]. An ad hoc experimental setup was designed to impose an electric field during the gelation of hydrogels: 24V and 220V were indeed proven capable of imposing an aligned structure to silk fibroin films [36]. Compression tests were performed to evaluate eventual changes in the bulk structure of hydrogels caused by the application of the electric fields.

Aims and structure of the thesis

This thesis aimed at performing a comprehensive mechanical study of the components of the device (i.e., electrodes), of the prototypes of the device, and the interplay between the device and its components and the surrounding embedding environment (i.e., the spinal cord). The mechanical performance was analysed to provide fundamental information for the design and development of the optimal device. Both experimental and theoretical approaches were used to achieve the final goal. Moreover, this thesis aimed at obtaining *Bombyx mori* silk fibroin hydrogels with microstructures imposed by the application of electric fields during gelation. Different concentrations of silk fibroin were tested, as well as different electric fields. The mechanical characterisation of these hydrogels was performed with compression tests. Moreover, possible treatments of the spinal cord injury were studied in a review on injectable hydrogels applied to the spinal cord tissue. The thesis is structured as follows.

A further step forward in the study of a non-invasive possible solution for spinal cord injuries was done, and **Chapter 1** reports a review study on injectable biomaterials for the treatment of spinal cord injuries.

Chapter 2 includes the mechanical characterisation of bare and coated microfibres proposed as electrodes for the ISMS device. An analytical description of the MFs behaviour in specific practical scenarios is proposed. The combination of the experimental and analytical data resulted in a method for the complete mechanical validation of the electrodes. This approach includes the standard mechanical properties and practical information useful for the operators who handle the electrodes. Moreover, an experimental and theoretical study on the interconnection between the electrodes was conducted.

Chapter 3 focuses on the experimental evaluation of the bulk and surface properties of bare carbon microfibres and carbon microfibres coated with graphene oxide.

The final device produced by Neurofibres is composed of interconnected microfibres. Several prototypes were tested to obtain the adhesion energy of the interconnections and **Chapter 4** reports the applied methods and the results obtained.

Once described the device and its components, **Chapter 5** includes the mechanical characterisation of the device, adding the embedding tissue component. The issue of the mechanical interplay between the device and the surrounding neural tissue is addressed in terms of failure. The study focuses on three failure mechanisms: the breakage of the device, the migration of the electrodes, and the delamination between the device and the embedding matrix through the pullout of the device. *Ad hoc* experimental setups were designed and developed to study these phenomena.

Neurofibres proposes an ISMS device in which the electrical stimuli are provided by an external device. This approach may lead to many issues such as the joints between different wires or infections. Thus, a possible solution with reduced invasiveness for a wireless electrical stimulation of the injured spinal cord is proposed in **Chapter 6**. Given the intrinsic piezoelectricity of silk, a first attempt to produce a piezoelectric scaffold capable of generating electrical stimuli when subjected to loads or strains was done. *Bombyx mori* silk fibroin hydrogels underwent electric fields, and eventual changes in their structure were investigated with compression tests

Chapter 1 Injectable scaffold-systems for the regeneration of spinal cord: advances of the last decade

1. Introduction

The incidence of spinal cord injury (SCI) is approximately 17,730 new cases each year in the United States [37]. The leading causes of injury are vehicle crashes, followed by falls and the case of violence. Damages of the spinal cord often lead to permanent functional and sensory loss due to the limited regenerative capacity of the central nervous system (CNS).

The clinical therapeutic guidelines of neurorestoration in the case of SCI are focused on alleviating secondary injury. They consist of restricting active and passive movement, early fixation, combined extramedullary and intramedullary decompression, suitable cell therapies, early rehabilitation, or electric stimulation therapy [38]. In particular, repetitive and rhythmical movements during early rehabilitation activate the spinal networks thanks to the sensorimotor information, which allows functional recovery and remodels the function of the cerebral cortex [39]. The neuroprotection aims to minimize secondary injuries by pharmacological therapy (i.e., erythropoietin, ibuprofen, indomethacin, antioxidants) [40] to avoid cellular apoptosis or necrosis and promoting neuronal survival. These clinical guidelines are very important to facilitate treatments by using prostheses or scaffolds to promote the regeneration of neural cells. The neuroregenerative therapies, instead, differ from the neuroprotective ones since they aim to create the best conditions for the neural tissue to maximally express its regenerative potential. The neuroregenerative approach is a younger discipline and thus few clinical trials have been performed. However, neuroregenerative methods seem to have less side effects than neuroprotective techniques. Given the advantages of both methodologies, the research is going toward combinatorial and interdisciplinary approach [41]–[43].

Currently, most of the clinical trials are based on stem cell therapy [42] or in situ pharmacological treatments. The main difficulty of the cell transplantation regards the inhospitality of the environment at and around the damaged tissue: inhibitory molecules and an inflammatory status prevent tissue regeneration, limit the cell survival, and the clinical efficiency of cell therapy. Instead, pharmacological treatments such as i) neuroprotective agents [44] (i.e. sodium salicylate, polyphenols, aspirin), ii) growth factors as well as iii) suppressors of inhibitory molecules of the inflammatory response (i.e. suppressors of NOGO-A, myelin-associated glycoprotein (MAG), oligodendrocyte-myelin glycoprotein (OMgp), and chondroitin sulfate proteoglycans (CSPGs) digestion with the administration of chondroitinase ABC (ChABC) or hyaluronidase) [45]–[48] are hindered by the blood-brain barrier or blood spinal cord barrier (BSB) that limit their diffusion. Furthermore, high systemic doses to reach a therapeutic concentration at the site of the injury could induce tumor formation, fibrosis or other negative effects caused by the off target of the molecules injected [49].

Researchers are pushing towards solutions avoiding further damages to the tissue. Non-invasive injectable biomaterials can be precisely positioned in the lesion site, and eventually repetitively injected to obtain the complete regeneration of the tissue. Moreover, the therapeutic advantages of directly injecting therapies in the parenchyma of the spinal cord were proven superior concerning the systemic delivery of materials. [50].

Some examples of injectable systems are i) self-assembling peptide materials (SAPs), whose gelation process is charge dependent; ii) amphiphilic diblock copolypeptide hydrogels (DCHs), which have a shear-thinning property, allowing the injection; iii) gel containing multiple tryptophans and proline-rich peptide domains, which undergo a sol-gel phase transition upon mixing or iv) injectable thermosensitive hydrogel of PEG–PLGA–PEG triblock copolymers [51], [52]. The aim of this review is to provide an overview on the in situ injectable scaffold-systems. The possible injectable solutions analysed belong to four categories: hydrogels, nanoparticles, self-assembly peptides, and composites.

2. Pathophysiology

The SCI following trauma is characterized by four subsequent stages: immediate, acute (0-7 days), sub-acute (7-14 days), and chronic (months) (Figure 1.1).

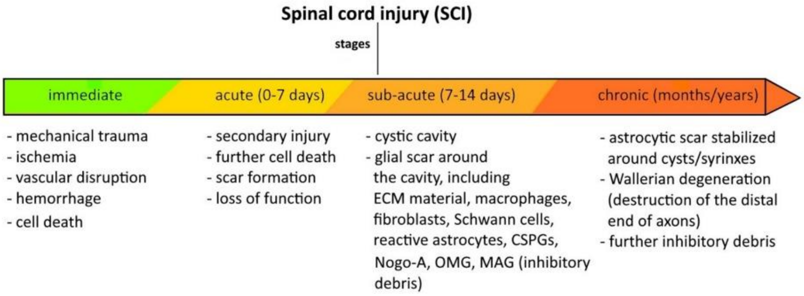

Figure 1.1 Timeline of the events following a SCI. Four stages characterize the injury progression: immediate, acute (0-7 days), sub-acute (7-14 days), and chronic (months).

In particular, a spinal cord contusion leads to an inflammatory reaction at the lesion site with the infiltration of leukocytes and activation of glial cells which limit the damage by reestablishing blood brain barrier and ionic homeostasis [53] (Figure 1.2). However, the dense scar and inhibitory molecules such as chondroitin sulphate proteoglycans (CSPGs), Nogo-A, OMgp, MAG, which appear at later stages, are detrimental towards regeneration [54]–[56] (Figure 1.2). In particular, CSPGs interact with proteins in the extracellular matrix due to its negative charges and these interactions could inhibit the neurite outgrowth following CNS injury [56]. Thus, the inhibition of CSPGs by using the bacterial enzyme ChABC seems to be very promising for enhancing axonal regeneration [57].

In the CNS, microglial cells are much slower compared to the peripheral nervous system (PNS) in clearing this debris, which may be present as long as three years post-injury [51].

External the CNS, macrophages derived from circulating monocytes reach injured tissues and some of them seem to represent controlled recruitment needed for repair [58] (Figure 1.2).

M1 monocyte macrophages were found to derive from monocytes that entered the injured spinal cord (SC) via monocyte chemoattractant protein 1 (MCP1) through the adjacent SC leptomeninges [58]. M1s possess proinflammatory, phagocytic, and proteolytic functions, essential for damaged tissue digestion and debris removal. M2 macrophages instead, came from monocytes that transit through the brain-ventricular choroid plexus (CP), via VCAM-1-VLA-4 adhesion molecules and epithelial CD73 enzyme [58],[59]. Along with the CP, leukocytes extravasate across the endothelium, interact with the tightly connected epithelial cells, and enter the blood-cerebrospinal-fluid

(CSF), facilitating the CNS immunosurveillance [58], [60]. M2 possess anti-inflammatory functions and are involved in tissue regeneration, growth, angiogenesis, and matrix deposition, supporting tissue remodeling [58],[61].

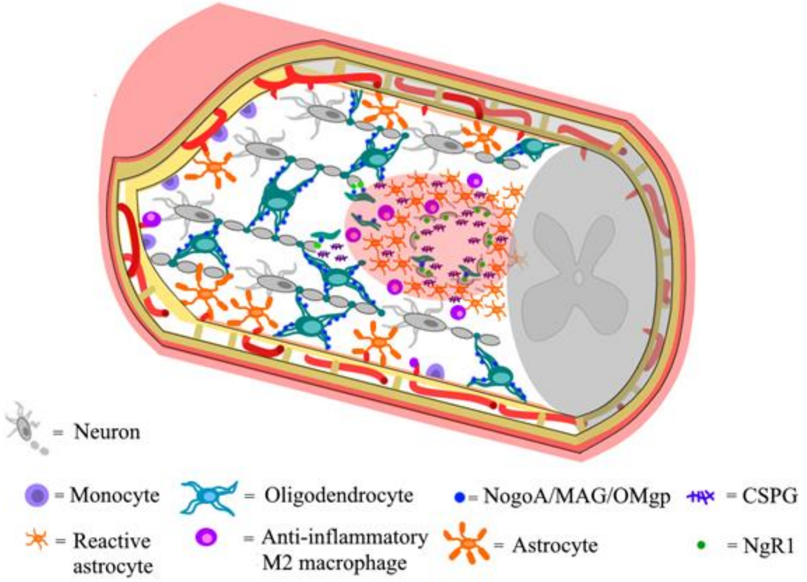

Figure 1.2 Pathophysiology model during the regenerative phase, involving the polarization of the monocytes in anti-inflammatory M2 macrophages to start the healing process.

During these detrimental phenomena, the neuroplasticity of the SC promoted in some cases spontaneous recovery of locomotor function after SC contusion3.

The reasons could be the variation of existing neuronal pathways, the formation of new connections, dendritic arborization remodeling, and axonal sprouting, regulating the expression of neurotrophin-3/4 (NT-3, NT-4), brain-derived neurotrophic factor (BDNF), and the glial cell-derived neurotrophic factor (GDNF) [62]. The spontaneous recovery also involves the presence of proliferating ependymal cells at early postinjury times, which later may have contributed to the expansion of the ependymal zone and the formation of cellular trabeculae within the lesion cavity [63]. The cellular trabeculae may serve to guide fibres from the CNS (like the corticospinal tract) into the centre of the lesion. The dorsal roots likely represent the main source for axons and Schwann cells which provide most of the myelin [63].

The presence of several regenerating axons within the lesion matrix after severe contusion injuries strongly suggests that under some conditions, the tissue repair response in the adult provides a substrate for growth.

3. Injectable materials for SCI treatment: description and results

A traditional surgery often requires a large incision with intrinsic risks, pain for the patient, perduring functional mobility, long hospital stay, long time of recovery and large costs for the healthcare system.

Minimally invasive surgical procedures have root in the middle of last century, with the experimental use of arthroscopy, but only in the 80’s minimally invasive surgery emerged as preferred alternative to open surgery procedures, to reduce trauma, surgery associated risks, pain for the patient and also treatment cost. Nowadays, the use of minimally invasive surgical procedures is considered of paramount importance as also evidenced in international research and innovation roadmaps and programs. For the spinal cord minimally invasive treatments, in situ injectable materials such as nanoparticles [57], smart hydrogels [39], [64], injectable lipid microtubes [65], self-assembling peptides [66], and self-assembling nanofibres [67]–[69] have been widely investigated and proposed. Injectable materials allow minimally invasive implantation procedures and present shape versatility; some of them can have stiffness comparable to the human spinal cord and possess water retention [51]. Moreover, they can be injected repeatedly until the complete functional tissue formation. Many of them can be functionalized or combined with adhesion ligands (i.e., IKVAV, RGD, CQAASIKVAV), growth factors (ex. fibroblast growth factor-2, FGF2, Neurotrophin-3, NT3), enzymes (es. chABC), and anti-inflammatory molecules (i.e., minocycline) to allow cell attachment, renewal, sprouting and extra cellular matrix (ECM) regeneration. However, several problems have been reported with the use of injectable materials: for instance, the injected materials could form aggregates, creating barriers to the tissue regeneration, as observed for collagen gels stabilized by carbodiimide that causes endogenous collagen deposition; an excessive swelling of the material could increase the local pressure causing secondary damages to the parenchyma [39].[70].

The electrical stimulation of neuronal cells [71], [72], and the formation of a controlled 3D structure along the longitudinal axis of the spine seem to be important requirements for i) surviving and maintaining the cells active [73],[74], ii) promoting long-distance axonal elongation [75], and iii) achieving oriented axons regeneration [76] for a natural tissue structure. It is still a challenge for injectable materials.

Non-invasive biomaterials-based systems that have been used for SCI therapies can be classified in hydrogels, smart hydrogels, nanoparticles, composites, and self-assembling peptides often combined with cells and specific signals. These systems are discussed below, summarized in Table 1.1 and the achievements obtained are represented in Figure 1.3.

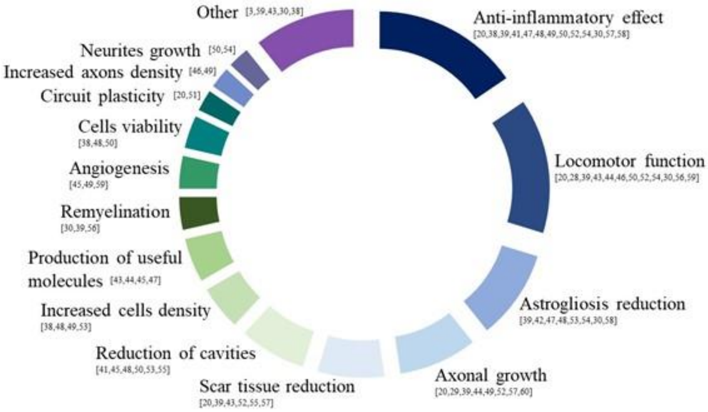

Figure 1.3 Achievements reported in the cited papers.

Table 1.1 Non-invasive biomaterials-based scaffold for the treatment of SCI. The table highlights many features of the systems: the animal and related SCI model, the material and the shape of the scaffold, eventual signals and cells used. The obtained achievements and the associated observations are also summarized.

Reference	**Animal model**	**SCI model/ location**	**Material**	**Shape**	**Cells**	**Signals**	**Achievements**	**Observations**
Azizi, M., et al. (2020) [57]	Rat	Contusion, T10	PLGA	Nanoparticles		chABC	↑ Anti-inflammatory M2 macrophages ↑ Axonal growth scar digestion in the injured site ↑ Locomotor function ↑ Circuit plasticity	Failure of extensive axonal regeneration Incomplete cleavage of the CSPG, MAG, OMgp and Nogo
Bonnet, M, et al. (2020) [39]	Rat	Contusion, T10	PNIPAAm-g-PEG	Thermo-responsive hydrogel			Unmodified inflammatory reaction ↓ Spasticity	No sensorimotor benefits after PNIPAAm-g-PEG combined with training Control+training and PNIPAAm-g-PEG+training had similar locomotor and ladder climbing test results

Führmann, T., et al. (2016) [77]	Rat	Compression, T2	HA + MC	Hydrogel	OPCs	PDGF-A RGD	Cell survival, integration, and differentiation (glial phenotype) ↓ Teratoma	Teratoma formation not avoided Teratoma caused no improvements in motor function
Vismara, I., et al. (2020) [78]	Mice	Compression, T12	PEG + PEI	Nano-structured gel	iPs human-derived	Rolipam	NG internalisation in 24 hours Selective internalisation in pro-inflammatory phenotypes (in vitro) ↓ Pro-inflammatory response NG internalisation in activated astrocytes, few in microglia none in neurons ↓ Production of inflammatory molecules by astrocytes (in vivo) Neuroprotective effect (in vivo)	The motor improvement observed at early stages after injury NG was not internalised in microglia and neurons
Wang, C., et al. (2019) [79]	Rat	Compression, T9	Laponite + heparin hydrogel	Hydrogel		FGF4	↑ Axonal regrowth ↑ Remyelination ↓ Astroglyosis ↓ Glial fibrotic scar ↓ Inflammatory response Motor functional recovery	

Hong, L.T.A., et al. (2017) [80]	Rat	Contusion, T10-11	imidazole-poly (organophosphazenes) (I-5)	Thermo-responsive hydrogel			↓ Cavity spaces Structural stabilisation ↑ Macrophages in the lesion for wound healing processes and ECM remodelling	
Boido, M., et al. (2019) [81]	Mice	Transection	Chitosan+ β GP	Thermo-responsive hydrogel	MSCs		Fast gelation ↓ Reactive astrocytes in the injury site ↑ MSCs survival in the injury site	Preliminary in vivo tests Locomotor recovery not evaluated
Li, X., et al. (2019) [82]	Rat	Hemisection, T9	P10R5-LA	Thermo-responsive hydrogel		Cabazitaxel	↑ Bladder functions ↓ Fibrotic scarring ↓ Axons growth inhibitory molecules ↓ Demyelination adjacent to the injury site Locomotor recovery	
Donaghue, I.E., et al. (2015) [83]	Rat	Impact/ compression, T1-2	HA + MC + PLGA nanoparticoles	Composite		NT-3 Anti-NogoA	↑ Bladder functions ↓ Fibrotic scarring ↓ Axons growth inhibitory molecules ↓ Demyelination adjacent to the injury site Locomotor recovery	

Kang, C.E., et al. (2012) [84]	Rat	Compression, T2	HA + MC + PLGA nanoparticles	Composite		FGF2	↑ Angiogenesis, ↓ cavity No proliferative lesion Sustained and long-term release of FGF2	No functional improvements
Ansorena, E., et al. (2013) [85]	Rat	Hemisection	Alginate + fibrinogen + (PLGA microspheres)	Composite		GDFN	↑ Number of neurofilaments Functional recovery Slow release of GDFN Homogeneous and dense regenerated tissues	Fast release kinetics Growing neurites absent within the lesion Free-GDNF hydrogels induced superior functional recovery compared to GDNF-microspheres hydrogel
Jain, A., et al. (2011) [86]	Rat	Hemisection, T8-10	Agarose + lipid microtubes	Composite		BDNF, CA-Cdc42, or CA-Rac1	↓ Number of astrocytes ↓CSPG deposition Presence of neurofilaments across the lesion, ↑ Axons in the CSPG-rich regions	↑ Immune/ inflammatory response Dosage of the three proteins not optimized

Chen, S., et al. (2020) [87]	Rat	Hemisection, T9-10	Silk fibroin + PDA	Composite			↑ Axons length ↑ Cell density ↑ Cell viability ↓ Glial cells High porosity Lesion cavity filled Fibrous distribution of neurons	Further in vivo studies needed Mechanical and morphological properties depend on PDA
Li, X., et al. (2020) [88]	Rat	Contusion, T9	PCL + MAL (fibres) + HA-SH + PEGDA	Composite			Limit spinal cord thinning ↑ Cells infiltration and interaction Suitable porosity Shift of macrophages from M1 to M2 ↑ Neovascularisation ↑ Differentiation of endogenous stem cells in immature neurons ↑ Number of axons	Role of nanofibres not fully known
Wang, C., et al. (2018) [89]	Mouse	Tissue removal, T12	[P(DLLA-co-TMC)) (fibres) + GCP	Composite	MN-ESC		Cell survival and engraftment in vivo NF inducedr ESC differentiation Neurite grew parallel to the axia direction Lesion cavity totally filled ↓ Tissue loss ↓ Inflammatory response Motor function recovery	Slow degrading dynamic

Khaing, Z.Z. et al. (2016) [90]	Rat	Transection, T2	PLGA (nanoparticles) + HA +MC	Composite		BDNF	Efficient delivery platform of bioactive molecules Material with tunable properties based on the molecular weight of HA Promotion of adaptive plasticity	Inflammatory response not investigated
Nazemi, Z., et al. (2020) [91]	Rat	Hemisection, T8-10	PLGA microspheres + Alginate	Composite		MH PTX	Prolonged release of the drugs (2 months) ↑ Inflammation, ↓ Scar tissue (ECM deposition) ↑ Axonal regeneration and protection reconnection of neural network Functional improvement	No therapeutic effect on cell death, no alteration of reactive astrocytes
Marquardt, L.M., (2020) [92]	Rat	Contusion, C5	C7 recombinant engineered peptide + PEG modified with proline-rich peptides + PNIPAM	Thermo-responsive polymer	SC		↓ Secondary injury ↓ Cystic cavitation ↓ Astroglyosis in the peri-lesion space ↑ Cell retention ↑ Neurons and axonal sparing	Unavoidable cell loss Ligands might be necessary Further full dynamic response of immune cells infiltration is necessary

Hu, H.Z., et al. (2018) [65]	Dog	Chronic severe SCI, L3-4 L4-5	Lipid microtubes + agarose	Composite		chABC-trehalose	↑ Locomotor function No long-term adverse effects	No improvements in detection of sensory evoked potentials
Tavakol, S., et al. (2015) [93]	Rat	Chronic SCI, T10	(RADA)4-GG-BMHP1	SAP	hEnSCs	BMHP1	↑ Neural differentiation Functional recovery ↓ Reactive astrocytes ↓ Inflammatory response	Axon regeneration and myelination limited to the area around the cavity ↓ cell proliferation in more concentrated gels
Cicognini, D. et al. (2014) [67]	Rat	Contusion, T9-10	B24 and biotin-LDLK12	SAP			Haemostatic effect ↑ Axon sprouting/ regeneration	SAP caused compression of the surrounding tissue
Zweckberger, K., et al. (2015) [94]	Rat	Compression/ contusion, C5-6	K2(QL)6K 2 (QL6)	SAP	NPC	BDGF EGF FGF	Cavity is bridged ↓ Scar tissue ↑ NPCs survival and migration	Osmotic micro-pump necessary
Tysseling, V.M., et al. (2010) [68]	Mouse/ rat	Compression, T10/ Compression, T13	Peptide amphiphile	SAP		IKVAV	Axon elongation Functional recovery Suppressed progression of astrogliosis ↑ Remyelination of axons inside the lesion Regeneration of corticospinal motor fibres and sensory fibres ↑ Number of serotonergic fibres caudal to the lesion significantly ↓ Cells undergoing apoptosis	

Ye, J.C., et al. (2016) [95]	Rat	Compression, T10	RADA16 (polypeptide)	SAP	NSC from primates		In vitro differentiation in neurons, olygodendrocytes and glial cells ↑ Myelin production ↑ Motor function recovery	Primate NSCs not easily available
Tran, K.A., et al. (2020) [96]	Rat	Contusion, C5	RADA16I	SAP	Human cerebral microvascular endothelial cells		↓ Inflammatory response ↓ Glial scar Axon growth across the lesion	Not oriented structure New axons could origin from sprouting Perfusion in the microvessel not tested
Hassanejad, Z., et al. (2019) [66]	Rat	Compression, T7-8	CH3(CH2)14 CO-AAAAGGGE IKVAV	SAP		IKVAV BDNF	No inflammatory reaction ↓ Astroglyosis ↑ Migration of astrocytes and oligodendrocytes in the injury Sustained release of BDFN for 21 days	Functional recovery was not statistically significant

Cicognini, D., et al. (2011) [97]	Rat	Contusion, T9-10	RADA16-4G	SAP		BMHP1	Remodelling of ECM Basement membrane deposition ↑ Angiogenesis ↑ Migration of neurons, microglia cells and olygodendrocytes precursors ↑ Locomotor functions recovery	Inflammatory response No cyst and cavities ↓ Partial filling of the injury cavity New axons could origin from sprouting
Sun, Y., et al. (2016) [98]	Rat	Transection, T	(Ac-(RADA)4-CONH2)	SAP	NSC/NPC	IKVAV RGD	↑ Cell viability and survval Differentiation of stem cells into neural and glial phenotypes in vitro Mild assembling process that presrvve the environment	Slow in vivo gelation Axons growth along the graft and not across it
Sever-Bahcekapili, M, et al. (2020) [69]	Rat	Hemisection, T9-10	Peptide amphiphile	SAP		IKVAV heparan sulfate-mimetic epitope	↑ Tissue integrity ↓ Cell loss Neurons toward injection site ↑ Locomotor functions recovery	

3.1 Hydrogels. They are materials characterised by a three-dimensional network with a hydrophilic structure that holds large amounts of water. Hydrogels can be injected before crosslinking with it happening in situ in some seconds/minutes. Some hydrogels can display the so called “smart” behaviour, with a non-reversible or reversible transition from the state of sol to the state of gel following the application of external stimuli. The main component of the extracellular matrix of the spinal cord is hyaluronic acid (or hyaluronan HA) [99], thus this natural polymer is widely used in SCI regenerative medicine. For example, hyaluronan-methylcellulose (HAMC) hydrogels, first studied by Gupta et al. [100], loaded with oligodendrocyte progenitor cells (OPCs), platelet-derived growth factor receptors (PDGF-R), and RGD promoted the survival, integration, and differentiation of cells [77]. However, teratoma formation was not avoided but attenuated concerning the cell-therapy (Figure 1.4).

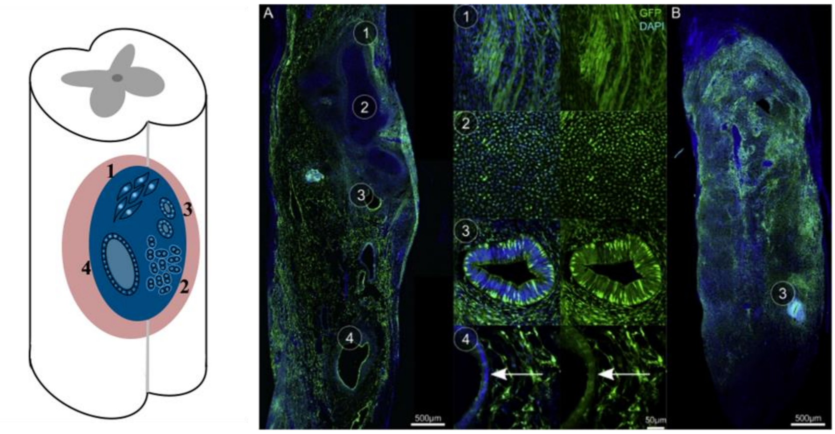

Figure 1.4 Morphology and immunohistochemistry of spinal cord tissue suggests: (1) muscle, (2) cartilage, (3) intestinal-like, epithelium, and (4) epithelium (arrow) within the teratoma. Figure 1.4 (right, A-B) reproduced with permission from ref 41. Copyright 2016 Elsevier.

Other problems could also derive from a “not well cleaned” (full of debris) lesion site, which may impede the gelation of the material [70]. Moreover, considering some injectable hydrogels such as gelling agents (ex. β-glycerophosphate disodium salt hydrate, β-GP) [81] blended with chitosan, imidazole-poly (organophosphazenes) (I-5) [80], [101], or pol*y*-N-isopropyl acrylamide-based thermoresponsive hydrogels, the sol-gel transition could be preferentially promoted by physical factors (ex. temperature, physiological pH). to avoid inflammatory response, generally caused by chemical crosslinkers [39].

To avoid the harmful mechanisms activated by reactive astrocytes after SCI, a PEG (polyethylene glycol)-PEI (poly(ethylene imine)) NanoGel (NG) delivering Rolipram (antidepressant drug) was injected in a mice compression model [78]. The results showed a selective internalization of NG in activated astrocytes, few in microglia, and none in neurons. Motor functional improvement was possibly caused by a reduced production of inflammatory molecules by astrocytes and its consequent neuroprotective effect. This result was observed in the early stage after injury [78].

A biopolymer largely proposed in regenerative therapy strategies is silk fibroin. Chen et al. [87] produced a material coupling the silk fibroin with the quinone structure of oxidized dopamine (DA). DA is a mussel adhesion protein recently studied as a cross-linking medium to obtain injectable hydrogels [102]. Indeed, DA goes towards a self-polymerization of free DA generating an injectable silk fibroin/polydopamine (SF/PDA) hydrogel. This material has favoured neurite growth and neuronal differentiation. This scaffold presents tunable properties by varying the concentration of DA. In vivo tests showed repair of SC tissue after hemisection in rats but further investigation is needed to evaluate possible clinical studies. Recently, a synthetic smectite clay (Laponite XLG, Na+0.7[(Si8Mg5.5Li0.3)O20 (OH)4]-0.7) was also used for SCI repair due to its capacity to aggregate in solution. Laponite XLG consists of interlayer cations (Na+) that balance the net negative charge of a single crystal of Laponite. Its ability in binding heparin is exploited in regenerative medicine applications. Indeed, Wang C., et al. [79] produced an injectable heparin-Laponite hydrogel loaded with a novel neuroprotective factor, the fibroblast growth factor 4 (FGF4). The results showed a motor functional recovery, reduced fibrotic scar tissue, and the inflammatory response with consequent remyelination.

Smart hydrogel polymers present a sol-gel transition responsive to different external stimuli: temperature, light, pH, ionic concentration, magnetic and electrical fields, and chemicals [103]. For thermo-responsive polymers, the transition occurs at specific threshold points: above the critical solution temperature (ex. LCST polymers) or below (ex. UCST polymers). The most common smart hydrogels used in SCI repair are thermoresponsive, such as poly(N-isopropyl acrylamide)

(PNIPAAm) [39] or triblock copolymers based on polyethylene oxide, polyethylene glycol, polypropylene glycol, or polylactic acid (ex. PEO-PEG-PEO or PLA grafted on PPG-PEG-PPG) [104].

PNIPAAm-g-PEG (poly(N-isopropyl acrylamide-g-polyethylene glycol), introduced by Comolli et al. [105], was investigated in contusion SCI cases and results showed an unvaried inflammatory response [39]. The locomotor recovery improved when PNIPAAm-g-PEG was combined with an exercise training program. The electrophysiological recordings indicated reduced spasticity of treated animals, but this benefit was not recorded when the polymer treatment was coupled with exercise.

PPG (polypropylene glycol)-PEG-PPG (P10R5) has been used to deliver a chemotherapic agent (Cabazitaxel) to the injured area [82]. Besides the inhibiting role of Cabazitaxel on prostate cancer, this chemotherapeutic drug was proven to be capable of supporting the neurite extension of cortical neurons in vitro. The treatment creates a protective environment leading to an improvement of bladder and locomotor functions.

Different delivery systems based on PNIPAM are produced to allow cells to reach the target site. Marquardt et al. [92] synthesized an engineered protein (C7), composed by repetitive motives CC43WW (Figure 1.5, left). The motives were separated by a multi-arm of 8-armed PEG tethered with proline-rich peptides, PNIPAMs, and cell-adhesive peptides (IKVAV, RGD, YIGSR). The system, called SHIELD (Shear-thinning Hydrogel for Injectable Encapsulation and Long-term Delivery) [106], represents an example of injectable hydrogel for autologous human Schwann cells (SCs) transplantation. The cell membrane protection promoted by the SHIELD encouraged a decrease of the cystic cavity and an increase of the functional recovery (Figure 1.5, right).

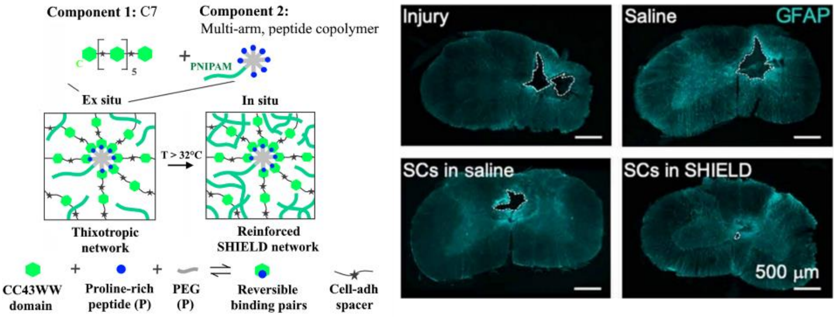

Figure 1.5 SHIELD design (left) and a scan fluorescent images (right) of spinal cord sections display cavity areas across all groups: untreated lesion (injury), injury treated with saline medium (saline), injury treated with saline medium (saline) and Schwann cells (SC in saline), injury treated with SHIELD and Schwann cells (SC in SHIELD), Cyan, GFAP (right). Figure 1.5 reproduced with permission from ref 56. Copyright 2020 American Association for the Advancement of Science.

3.2 Nanoparticles. Given the small dimensions, nanoparticles can be injected in the affected area through the needle of a syringe. The fabrication methods (ex. double emulsion/solvent evaporation technique, thermal decomposition) used to produce these particles give the opportunity of embedding specific signals or cells. Azizi et al. [57] studied the use of poly(lactic-co-glycolic acid) PLGA nanoparticles (273.5 ± 36.4 nm) embedding chABC in a rat contusion model. The anti-inflammatory response was promoted by the enhancement of regenerative M2 macrophages (in a process described above) and caused axonal regrowth (Figure 1.6). The improvement of locomotor functions and the enhancement of circuit plasticity were also observed. However, the PLGA nanoparticles failed in obtaining an extensive axonal regeneration and the complete cleavage of the CSPG, MAG, OMgp, and Nogo. These results were obtained through an ”extrinsic” approach, different from the “intrinsic” one [80] described in Figure 1.7. Additionally, Zhang et al. [107] used nanoparticles to track the position of mesenchymal stem cells (MSCs), investigating their optimal number to transplant in the post-traumatic syrinx caused by SCI. Nanoparticles of 53□9 nm made of ferric oxide (Fe3O4) cores were coated with bovine serum albumin (BSA) covalently conjugated with monoclonal antibodies against vascular endothelial growth factor (mAbVEGF). The results showed a precise transplantation strategy of MSCs thanks to the magnetic resonance imaging (MRI) visualization of magnetic nanoparticles.

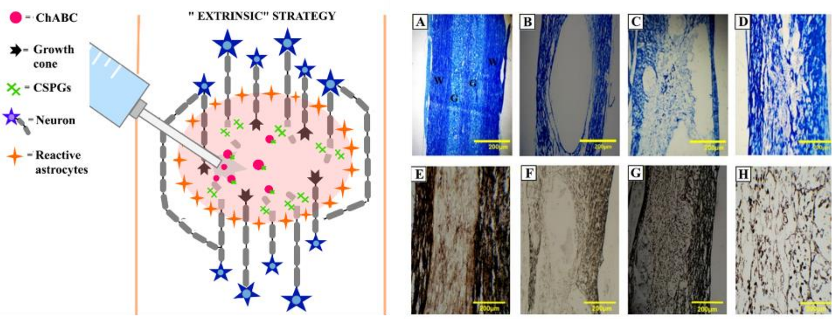

Figure 1.6 Injected drugs such as ChABC delivered by nanoparticles (NPs) showed a local action/extrinsic strategy of CSPGs removal. The remaining inhibitory molecules are not completely removed, and a pathological status is partially present (left), while a regenerative process (plasticity increasing, axonal growth and elongation) can be observed. Luxol fast blue (LFB) (A–D) and Bielschowsky (E–H) staining of longitudinal sections of the injured spinal cord within 8 weeks after treatment (right). The samples observed are (A, E) the sham group, (B, F) untreated spinal cord after injury, (C, G) PLGA NPs injected without ChABC (D, H) the ChABC particle-treated groups. In the Bielschowsky staining, the axons appear brown to black in color. W and G stand for the white and the gray matter of the spinal cord, respectively. Figure 1.6 (right, A-H) reproduced with permission from ref 21. Copyright 2020 Elsevier.

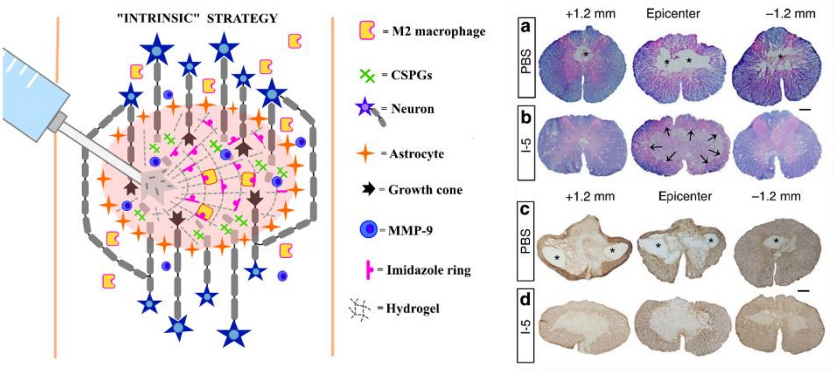

Figure 1.7 . Injection of I-5 hydrogel stimulates an "intrinsic" mechanism of MMP-9 and M2 macrophages recruitment come from the surrounded tissue. The imidazole rings located in the hydrogel matrix interact with the histamine receptors on macrophages that linger for a prolonged time enhancing a wound healing mechanism (left). On the right (a-d) the effects of I-5 injection can be evinced: a cystic cavity reduction, ECM remodelling and inflammatory response decrease. Representative images of transverse spinal cord sections stained with eriochrome cyanine and eosin (a, b) or GFAP antibodies (c, d). Spinal cord sections were obtained from animals 4 weeks after PBS (a, c) or I-5 injection (b, d). The sections shown are from the epicenter and 1.2mm rostral (+1.2 mm) or caudal (−1.2 mm) to it. Asterisks indicate cystic, cystic boundary are indicated by black arrows (b). Scale bars represent 200 µm. Figure 1.7 (right, a-d) reproduced with permission from ref 44. Copyright 2017 Springer Nature.

3.3 Composites. The term refers to the combination of two or more materials with different physical properties resulting in a new material with improved tailored characteristics. Injectable composites for SCI repair are generally made of nanotubes/nanoparticles/nanofibres/microtubes embedded in hydrogels. In particular, microtubes are generated by self-assembly of glycolipids, phospholipids, and other amphiphilic molecules. Variation in concentration, pH, or temperature influences the supramolecular assembly, which is driven by van Der Waals, electrostatic forces, or hydrogen bonding. Microtubes embedded in hydrogels are investigated as drug carriers for SCI repair applications. For example, hemi-sectioned chronic severe SCI in dogs was treated with a hydrogel-lipid microtube based delivery system of chABC combined with trehalose [65], TS-ChABC. Trehalose was found to stabilize chABC activity at 37 °C but the mechanisms are not well known [55]. The thermal stabilization of chABC demonstrated: sustained drug delivery, CSPG inhibition, improvements in locomotor function in dogs with chronic severe SCI, and some sensory recovery, which increased if chABC and NT3 were combined. The chABC long-distance diffusion required into the injured human spinal cord could be a limitation. Generally, chABC is administrated continuously by invasive pumps implanted in vivo but TS-chABC via hydrogel-microtube system could be a less invasive option.

Lipid microtubes associated with different axonal growth cones factors (Cdc42, Rac,1, and BDNF) were also coupled with agarose hydrogel by Jain et al. [86]. In a dorsal over-hemisection lesion, the treated rats showed a reduced number of reactive astrocytes in the injured area, a reduced CSPG deposition, the presence of neurofilaments across the lesion, and a higher percentage of axons in the CSPG-rich regions. The dosage of the three growth factors was not optimal for stimulating the axonal growth in the CST.

Specific molecules proven to be useful in healing and regenerating the spinal cord can also be loaded in nanoparticles, which are eventually embedded in hydrogels to allow a sustained release of drugs or factors. A composite of HA and methylcellulose (MC) hydrogel with PLGA nanoparticles was used to localise the nanoparticles in the specific site of injection and for the sustained release of neurotrophic factors and inflammatory molecules suppressors (embedded in the nanoparticles). [83] The BBB score of treated rats with a compression injury increased with respect to controls, but the inflammatory response was notable. The same composite structure was also coupled with FGF2 [84]. Thanks to the degradation kinetics of the materials, a sustained and long-term release of FGF2 was obtained. Results showed improved angiogenesis, a decrease of the cavity volume, and proliferative lesion, but functional improvements were not recorded.

Ansorena et al. [85] demonstrated that a composite scaffold made of alginate, fibrinogen, and PLGA microspheres increased the number of neurofilaments, gained functional recovery, and more homogeneous and dense regenerated tissues through the slow release of GDFN. However, the functional recovery in hemisected rats was higher with free-microsphere hydrogels.

Instead, a nanofibre-hydrogel composite was produced by mixing fragments of polycaprolactone (PCL) fibres with surface grafted maleimide (MAL) groups, and a gel of thiolated hyaluronic acid (HA-SH) and polyethylene glycol diacrylate (PEGDA) [108], [109]. The material provided mechanical support for spinal cord regeneration and a suitable porosity for cell infiltration. The spinal cord thinning because of the progressive loss of neural tissue following contusion was controlled by the presence of the composite. The authors reported a shift of M1 macrophages to M2, limited to the lesion site, possibly linked to the presence of the PCL fibres. The role of fibres needs to be further investigated, but their presence seemed to encourage neo-vascularisation and differentiation of endogenous stem cells in immature neurons.

A minimally invasive method to deliver mouse embryonic stem cell (mESC) in the injury site was studied by Wang et al. [89]. They embedded an aligned electrospun nanomesh of poly (D,L-lactic acid-co-trimethyl carbonate (P(DLLA-co-TMC)) in gelatin-acrylated β-cyclodextrin (β-CD) polyethylene glycol (GCP) hydrogel, which was formed by the photo-crosslinking process. The high stretchability of this material allows it to be injected. Motor neurons derived from embryonic stem cells (MN-ESC) were also embedded in the composite. Results showed an oriented neurite growth, a dendritic development, a decreased loss of tissue and inflammatory response, synapses formation, and motor function recovery. The material filled the injury cavity, but the degradation kinetics was not optimal.

A hydrogel of hyaluronic acid and methylcelluloseenriched with PLGA microparticles and BDNF was tested in a rat transection model [90].

This material had tunable mechanical properties, gelation, and biological activity by changing the molecular weight of HA. The inflammatory response was not investigated but the scaffold improved the adaptive plasticity.

Nazemi et al. [91] used microspheres of PLGA for the delivery of hydrophobic drugs such as the paclitaxel (PTX). PTX is an anti-cancer drug that leads to axonal growth, functional outcomes, and a reduction of the fibrotic scar when injected at the lesion site of rat’s spinal cord. The microspheres loaded with PTX were included in an alginate hydrogel that interacted electrostatically and by metal-ion chelation with minocycline hydrochloride (MH). This composite showed a prolonged drug release (2 months), a decrease of the inflammation response and scar tissue, an increase of axonal regeneration, protection, and functional improvement.

3.4 Self-assembling peptides (SAP). Amphiphilic molecules can show self-assembly capacity through noncovalent interactions forming 3D structures. Amphiphile peptides (AP) can be designed alternating hydrophilic and hydrophobic amino acids or positively and negatively charged amino acids that can undergo to self-complementary assembly. For example, Yuqiao Sun et al. [98] presented a strategy to create nanofibre hydrogels using two oppositely charged SAPs conjugated with bioactive peptides motifs such as IKVAV [110] or RDG. The use of peptide amphiphile coupled with IKVAV in rat spinal cord transection gave many beneficial results: axon elongation, functional recovery, suppressed the progression of astrogliosis, facilitated remyelination of axons inside the lesion, regeneration of corticospinal motor and sensory fibres, increasing the number of serotonergic fibres caudal to the lesion, and decreased cells apoptosis. Unfortunately, there was a small number of regenerating dorsal column fibres. Tysseling et al. [68], [111] verified also the effect of IKVAV peptide conjugated with amphiphile peptide (PA) on rat spinal cord compression model with similar results.This SAP-based scaffold was first studied by Silva et al. [110], obtaining an efficient differentiation of stem cells into neurons. PA nanofibres were also studied when displaying the heparan sulfate mimetic and laminin mimetic epitopes [69]. The in vivo studies showed this injectable scaffold as a valid ECM substitute after SCI. Indeed, an overall tissue integrity was obtained, and the locomotor functions of the treated animals improved.

Cicognini et al. [67] investigated the use of two SAPs B24 and biotin-LDLK12 for the treatment of a contusion injury in rats. The SAP B24 is derived from the functional motif of the bone marrow homing peptide 1 (BMHP1), whereas biotin-LDLK12 is an ionic SAP (motif: biotin-LDLKLDLKLDLK-CONH2). At the same concentration (1.12 mM), B24 resulted in less viscous than the biotin-LDLK12, which was less permissive to water, free radicals, and immune cell infiltration than B24. Thus, Biotin-LDLK12 formed a dense scaffold after injection without diffusing within the injured tissue as opposed to B24 and showed a slower degradation rate. For these reasons, the hematoma reabsorption was faster where biotin-LDLK12 was injected (Figure 1.8). However, SAPs swelling caused the compression of the surrounding tissue.

Self-assembling peptide (RADA16) nanofibre containing IKVAV motif were also studied for central nervous system applications [112], [113]. Cicognini et al. functionalized RADA 16-I to BMHP1 by using a 4-glycine bridge and observed an increase of vascularization and migration of glial precursor cells, a remodelling of the ECM with consequent decrease of cyst area [97].

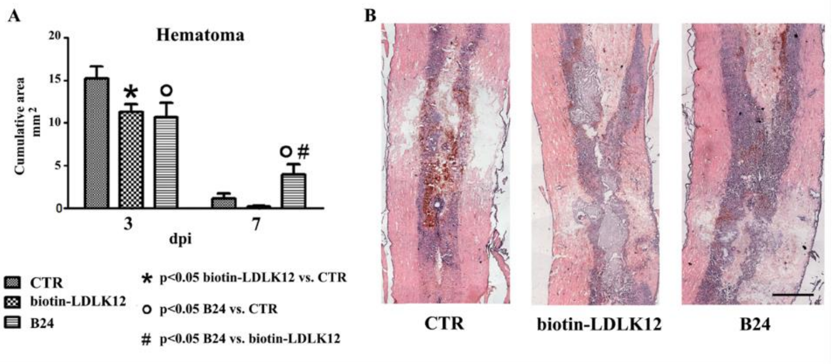

Figure 1.8 Quantification of hematoma. (A) At 3 day after injury (dpi) both SAP-treated groups had a significant lower leakage of red blood cells in comparison with controls. At 7 dpi biotin-LDLK12-treated animals showed the lowest content of red blood cells, while B24 the highest one. (B) Longitudinal sections stained with hematoxylin/eosin showed the presence of extravasated red blood cells (red-brownish coloured). Scale bar: 700 µm. Figure 1.8 reproduced with permission from ref 31. Copyright 2014 American Scientific Publishers.

Tran et al. [96], investigated instead the use of pH-responsive self-assembly hydrogel, RADA-16I (Ac-RADA4-CONH2), to primarily provide a favourable environment for capillary formation. Indeed, the damage of the blood spinal barrier (BSCB) causes inflammation and glial scar formation that inhibit tissue regeneration. The results showed the presence of microvessels from 9.0 ± 3.1 μm to 100 ± 46 μm within the RADA-161 hydrogel, depending on the cell density condition. The formation of the BSCB within the RADA-161 hydrogel reduced inflammatory response and scar formation and increased axon infiltration into the SCI site. An improvement of this system could be the control of microvessels orientation because the axon growth specifically in the rostral-caudal direction could be essential for SCI treatment. Arginine-alanine-acid aspartic-alanine (RADA)4 SAP was also used by Tavakol et al. [93] in combination with IKVAV or with a longer laminin motif (CQAASIKVAV (CQIK)) [93] to form a hydrogel-based material with nanofibre structure. CQIK resulted in improved cellular response compared to IKVAV peptide due to the greater similarity to the laminin active site. In both cases, it was observed neurite outgrowth, myelination, and inhibited astrogliosis. The locomotor recovery was significantly less than (RADA)4 combined with bone marrow homing peptides (BMHP).

Ye et al. [95] cultured isolated primate NSCs in polypeptide RADA16 (AcN-RADARADARADARADA-CNH2) that can be assembled at physiological pH. The in vivo tests on the rat compression model showed differentiation of NSCs to neurons, oligodendrocytes and astrocytes, myelin production, and motor function recovery.

A type of SAP used to minimize SCI damages is also represented by K2(QL)6K2 or QL6 [94]. It is characterized by alternating ionic hydrophilic and hydrophobic amino acids that self-assembly into beta-sheet at physiological pH. After the acute stage, QL6 was injected into the center of the lesion, whereas the neural precursor cells (NPC) into adjacent dorsal columns. The cell survival is promoted by continuous subdural administration of growth factors through an osmotic micropump for 7 days. The presence of the scaffold improved the inhibitory environment, reducing the scar tissue and the inflammation with consequent cell survival and differentiation up to functional recovery.

Amphiphilic peptides (CH3(CH2)14CO-AAAAGGGEIKVAV PA) functionalized with the laminin motif IKVAV were investigated by Hassannejad et al. [66] in order to produce an injectable hydrogel for a sustained release (21 days) of brain-derived neurotrophic factor (BDNF). This latter neuroprotective protein-enhanced neurite outgrowth from the dorsal root ganglion (DRG) explants and the presence of the hydrogel resulted in considerable axon preservation at 6 weeks post-injury. The functional recovery was not statistically significant between IKVAV-PA hydrogel injected and saline-injected animals.

4. Spinal cord injury models

Different types of trauma can be simulated in vivo, generally on the spinal cord of adult rats. These injuries are contusions, compressions, hemisections, or complete sections of the spinal cord and they are performed following standard protocols to obtain reproducible results.

4.1. Severe and moderate contusion model. A reproducible contusion model on rat spinal cord via the weight-dropping method could be performed by using a stereotactic frame and computer-controlled impactor. A severe contusion is, generally, caused by an impactor tip of 3.0 mm at a speed of 4 cm/s with a depth of 2 mm and a dwell time of 0.3 sec towards an exposed and well stabilized spinal cord surface [114]–[116]. A severe contusion induces the highest gray matter losing, few white matter sparing, and biochemical changes such as free radicals, prostaglandins, calcium-activated proteases, loss of myelin proteins [117], extracellular potassium and calcium concentrations changes. Blight and Decrescito (1986) [118] had observed that large, myelinated axons are more damaged at the nodes of Ranvier than the axons closest to the pial surface. Damaged axons caused calcium entry through tetrodotoxin-sensitive channels and consequent secondary reactions due to the calcium entry [119], [120]. A moderate contusion model, instead, preserves most of the ventral and ventral-lateral descending pathways that led to post-injury locomotor recovery in both trained and untrained animals [39].

Mechanical disruption via weight-dropping method was universally accepted to be clinically relevant [114], [115], because it simulates human contusion due to their ability to mimic both primary mechanical damage and secondary reactive phase of injury.

4.2. Compression model. The compression is generally induced by an aneurysm clip closed around the exposed spinal cord of rats for 1 min until the generation of an extradural compression of 30 xg pressure. This model also simulates clinical conditions observed in several human cases but causes moderately severe acute compression injury [121].

4.3. Unilateral and hemisection model. The unilateral and hemisection of the spinal cord simulate an injury clinically observed in human cases and allow to compare injured and healthy fibres in the same animal [114] but shows disadvantages concerning model uniformity [122].

4.4. Complete model. The complete spinal cord injury model is generally performed at the T9-T10 segment, and a gap of 2 or 4 mm allows the insertion of the scaffold [99]. The complete transection interrupts axon fibres and propriospinal neurons resulting in permanent paralysis. This model is considered by many researchers as the gold standard for validating axonal regeneration, but it is not clinically relevant and it shows high variability in the results [122],[115].

5. Severe contusion model as the new gold standard: how?

During the past decade, the complete transection SCI model has been used for validating axonal regeneration, but this model is far from a real case of human spinal cord injury [123],[114], [119]. A contusion model, instead, reflects a traumatic human SCI but it is unsuitable for validating axonal regeneration because it is difficult to discriminate the contribution of the scaffold to the axonal regeneration from the spontaneous regeneration of the tissue [114],[122]. Thus, matching a reproducible and reliable axonal regeneration with the use of a realistic SCI model is still a challenge. Some researchers proposed studies based on the contusion model to have clinical relevance (as described above) and in vitro models to obtain reliable results on the neuronal regeneration.

The commonly used in vitro cell culture models of SCI include i) primary isolated neurons, oligodendrocytes, astrocytes, or microglia cells; ii) co-culture of neuronal cells with different cell types, which are present in the glial scar; iii) co-cultivation with meningeal cells in in vitro scar formation model, called scratch model; iv) rat spinal cord cells onto a confluent monolayer of neurosphere derived astrocytes for investigating the CNS axonal myelination; v) neurite outgrowth assays for the phenotypic expression of regeneration progress [124].

However, the in vitro evaluation lacks the complexity and physiological relevance of in vivo system, but the results are reliable and reproducible. Unfortunately, animal studies offer complexity, which is very difficult to model in vitro, and high variability, which prevents reproducible studies [125],[126]. For this reason, organotypic cultures of spinal cord explants could be an option to obtain reproducible results after a contusion injury [124], [127]. The spinal cord explants are cut to obtain slices, called organotypic slices (OTSs), that preserve the basic structural and connective organization of their original tissue (organotypic). OTSs represent an interim system sharing the properties of the cell culture in vitro and an animal in vivo model. Organotypic spinal cord slice (OTS-SC) are generally cultivated on a semi-porous membrane at the air-medium interface to allow nutrition and gas exchanges, under appropriate conditions the slices can survive for a week to months [124].

The OTS-SC model is suitable for axonal growth evaluation because the typical ventrodorsal polarity of the SC is maintained after a culture period of 2 weeks, and intrinsic spinal cord axons formed a strong fibre tract extending along the longitudinal axis of the slice [124], [127] (Figure 1.9).

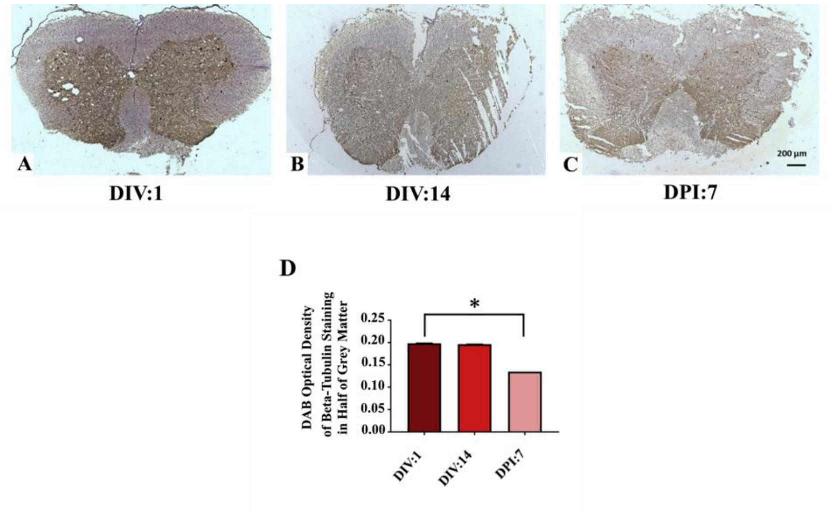
DIV:1 **DIV:14** **DPI:7**

Figure 1.9 The first day of OTS-SC culture (A) is compared with the slice observed seven days after injury (DPI:7) (B) and its uninjured counterpart (DIV:14) (C). In the diagram (D) is reported the expression of βIII Tubulin in spinal cord slices. Figure 1.9 reproduced with permission from ref 90. Copyright 2019 Elsevier.

A well-defined in vitro evaluation could contribute to understanding the results of in vivo analysis, for example, Basso, Beattie, and Bresnahan locomotor score (BBB), ladder climbing test, electrophysiological recordings such as the rate-dependent depression (RDD) of the Hoffmann’s reflex (H-reflex), defined as “the decrease in reflex magnitude relative to repetition rate” [39], suitable for evaluating sensorimotor improvements and spasticity. Moreover, this model could highlight the real contribution to the neuroregeneration of the material implanted, because the mechanism leading to post-lesional adaptive plasticity might be avoided. Mechanical disruption via weight-dropping was also tested on OTSs [127]. The results confirmed the use of this model as a simulation of a human contusion due to their ability to mimic both primary mechanical damage and the pathophysiological mechanisms after SCI. However, OTSs are harvested from animals and their treatment is expensive and time consuming [124],[129]. These few limitations allow the use of OTS as a relevant platform before in-vivo testing [127], [130].

The validation of injectable biomaterials for an eventual advanced therapy medical product (ATMP) or medical device passes through different levels, including a period of nonclinical and pre-clinical research studies, involving parametric data collection and analysis in well-defined systems [131]. In the future, we will need to establish high throughput test platforms for biomaterials, that comprise standardised testing protocols for ex vivo, in vivo, pre-clinical, and clinical testing. In the case of the SCI contusion model, there is a standardised method to elicit the lesion [114], [115], [119], [132] but the effects of biomaterials are not completely understood once tested in vivo due to the high neural tissue complexity. To reach the application of biomaterials on patients, OTC-SC or 3D neural cell culture models could be used to validate the results obtained from BBB locomotor score, ladder climbing test, electrophysiological recordings and acquire reliable data in well-defined system.

6. Conclusions

Non-invasive materials for SCI treatments have gained interest due to their in situ safe procedure of administration, which might be done more than once until the complete ECM formation. Repetitive injections, still now, are expected just for cell therapy, failing the cooperation with supporting materials.

Future studies might be focused on the optimization of injectable material production such as i) swelling control, which may cause secondary damages, ii) use of non-toxic crosslinkers, iii) gradients applied on the deposited scaffold to induce a growth directionality, iv) more precise mimicking of the ECM composition and mechanical properties; v) combination of multiple fabrication methods, vi) control of the 3 D structure, vii) non-invasive electrical stimulation.

These non-invasive systems are generally injected during the sub-acute stage, when the injured site is characterized by a cystic cavity surrounded by a glial scar of ECM material, macrophages, cell, and inhibitory debris and a spontaneous regeneration process begins. In vivo models show the variability of outcomes even if the defects are standardized. Moreover, the SCI pathology in this model is sensibly different from humans, and the regeneration shows distinct differences in terms of axon elongation and mechanisms of sprouting [70]. Thus, in vivo results could be accompanied by ex vivo validation such as OTC-SC after compression model or 3D neural cell culture models that might give more reliable data.

Clinical trials are difficult to reach mainly due to the high cost and variability of in vivo testing and the complexity of the biological environment where materials are tested.

Reprinted (adapted) with permission from Santi, S., Corridori, I., Pugno, N. M., Motta, A., & Migliaresi, C. (2021). Injectable Scaffold-Systems for the Regeneration of Spinal Cord: Advances of the Past Decade. ACS Biomaterials Science & Engineering, 7(3), 983-999. Copyright 2021 American Chemical Society.

Chapter 2 Comprehensive mechanical characterisation of intraspinal microstimulation electrodes

1. Introduction

The loss of continuity in the spinal cord following an injury avoids the execution of functions controlled by the spine and nerves below the damaged area. ISMS is a promising technique to restore tissue continuity and thus achieving the functional regeneration of the spinal cord [133]. The ISMS is performed through devices composed of MFs-electrodes that are usually implanted below the damaged area and provide electrical stimuli to specific areas of the neural tissue.

Different materials are used for the electrodes, which are usually inserted vertically in the spinal cord to reach the targeted neural network [18]–[20]. However, an innovative use sees the ISMS device as a bridge between the two functional stumps of the spinal cord (above and below the injury), passing through the injured area. This device is developed in the project Neurofibres.

In the initial planning of ISMS devices, the choice of the high-performance electrode is crucial. Since the electrodes are usually implanted perpendicularly to the longitudinal axis of the spinal cord, the stiffness is the adopted mechanical property to test the feasibility of the electrodes and the targeting of the specific region [6], [18], [22]. The mechanical validation of the electrodes is then focused on the step after the implantation, considering the interplay with the surrounding tissue. However, the mechanical performance of the electrodes, useful for the selection of the best candidate, could be evaluated thoroughly before the in vivo step, avoiding the waste of material, animals, and time. This work aims at providing a comprehensive method for the evaluation of the mechanical performance of electrodes for ISMS before the final implantation. The here proposed method focuses on a complete mechanical characterisation, not only concerning the standard properties extrapolated from tensile tests (ultimate strength, strain at break, Young’s modulus, and toughness modulus) but also providing practical and useful information for the operators (i.e. surgeons, engineers), who handle the electrodes. Indeed, an analytical description of the MFs behaviour in specific real scenarios is proposed, such as the insertion in the spinal cord tissue, their handling and eventual contacts, the bending limits. The output of the method is a matrix including the information acquired during tensile tests and with the analytical model. This approach was developed to evaluate the mechanical performance of ISMS electrodes in the innovative modality of insertion in the tissue proposed by Neurofibres, but also to have a comprehensive universal procedure to evaluate their mechanical performance. Moreover, since the ISMS device is formed by interconnected MFs, an experimental and theoretical study of the single interconnection unit is presented.

2. Materials and methods

2.1. The device: components and features

The ISMS device here studied is composed of MFs with two different roles: electrodes and connectors. The electrodes-MFs are placed parallel to the longitudinal axis of the spinal cord. The connectors-MFs (even called wires or microwires to distinguish them from the electrodes) are perpendicular to the electrodes. These wires connect the MFs among each other’s and to the external instrument that imposes the electrical current. Figure 2.1 describes a prototype of the final system and how it will be implanted in the human spinal cord. The x-y notation used below does not correspond to the final use of the device, but it was chosen coherent with the configuration of tensile tests.

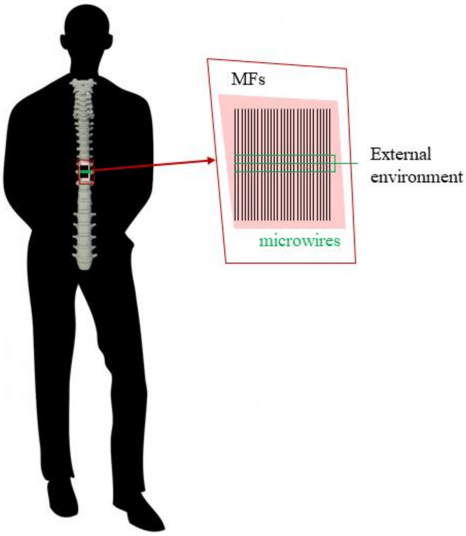

Figure 2.1 The ISMS device will be grafted in the injured area of the spinal cord, where it supports and increase the regeneration of the tissue. The device is composed of MFs (electrodes) positioned parallel to the longitudinal axis of the spine connected with microwires arranged perpendicularly to the MFs. The microwires have two roles: joining the MFs and connecting them to an external tool that imposes the electrical stimuli.

Commercially available MFs of different materials were mechanically characterised. MFs coated with a conductive polymer to increase electrical conductivity [24] were also characterised. These MFs (provided by the Neural Repair and Biomaterials Laboratory, Hospital Nacional de Paraplejicos de Toledo, ES) were coated with poly[(4-styrenesulfonic acid)-co-(maleic acid)]-doped (PEDOT:PSS-co-MA) or the PEDOT-borontrifluoridediethyletherate (PEDOT:BFEE). The tested specimens are summarised in Table 2.1.

Table 2.1 Summary of the microfibres subjected to a tensile test: Polyacrylonitrile carbon, stainless steel (316LVM), cobalt based alloy (35N LT), gold, platinum, carbon coated with PEDOT:PSS-co-MA, carbon coated with PEDOT:BFEE, stainless steel coated with PEDOT:PSS-co-MA, stainelss steel coated with PEDOT:BFEE, cobalt based alloy coated with PEDOT:BFEE.

Bare fibre	Coating	Diameter [μm]
PAN carbon		7
Stainless steel 316LVM		12.7
Cobalt chrome 35N LT		12.7
Gold 99.9%		10
Platinum 99.9%		10
PAN carbon	PEDOT:PSS-co-MA	8
PAN carbon	PEDOT:BFEE	8
Stainless steel 316LVM	PEDOT:PSS-co-MA	13.7
Stainless steel 316LVM	PEDOT:BFEE	13.7
Cobalt chrome 35N LT	PEDOT:BFEE	13.7

2.2. Mechanical characterisation of the electrodes

The mechanical behaviour of the MFs was studied with tensile tests (Figure 2.2a). The fibres were glued to a paper frame with a 11x11mm square window (Figure 2.2b). The samples were mounted on an Agilent T150 UTM nanotensile machine and the testing speed was 0.1%-gauge length/second (i.e., around 0.01 mm/s). The gauge length of the fibres was 11 mm (equal to the side of the square window of the paper frame). The diameter of the bare fibres was provided by the manufacturer, the diameter of the coated microfibres was measured with SEM images; the cross-sectional area was considered circular. The engineering stress was computed by dividing the force for the cross-sectional area of the microfibre, and the engineering strain was obtained by dividing the displacement for the gauge length of the sample. The force-displacement curves obtained with the tensile tests were processed to obtain the ultimate strength (σ_u), the strain at break (ε_u), the Young's modulus (E), and the toughness modulus (T). The ultimate strength was the engineering stress reached before fracture and the strain at break was the correspondent strain. Given the linear elastic behaviour of the fibres, Young's modulus was calculated as the slope of the stress-strain curve. Finally, the toughness modulus is associated with the area under the stress-strain curve and was calculated as:

$$T = \frac{1}{m}\int_0^{\delta_u} F dx = \frac{Al}{m}\int_0^{\varepsilon_u} \sigma d\varepsilon = \frac{1}{\rho}\int_0^{\varepsilon_u} \sigma d\varepsilon \qquad (2.1)$$

Where m is the mass of the microfibre, δ_u is the displacement at break, F is the recorded force, A is the fibre cross-sectional area, l is the fibre initial length, ρ is the volumetric density of the fibre, ε_u is the strain at break, and $\int_0^{\varepsilon} \sigma \, d\varepsilon$ is the area subtended by the stress-strain curve.

2.3. Mechanical properties of interconnected microfibres

The final configuration of the device designed and developed in Neurofibres and many other ISMS devices [9], [19]–[21] includes several interconnected MFs, to maximise the efficiency and efficacy of the intraspinal micro-stimulation. To evaluate the effect of fibres junctions in its final configuration, tensile tests were performed on carbon MFs interconnected with a small drop of cyanoacrylate glue. The samples were composed of two perpendiculars (one *y*-directed MF and *x*-directed MF) MFs, interconnected in the midpoint (Figure 2.2c) and forming a Greek cross. The aim was to evaluate the mechanical behaviour of a single junction. The MFs ends were attached to the paper frame (11x11 mm square window). The length of each arm of the so formed cross was 5.5 mm (L_0). The tensile tests were performed by pulling the *x*-MF, to evaluate the stiffness of the joint. Thus, before testing, the *y*-MF was cut around 2 mm after the junction, and the lateral parts of the paper sample holder were cut 2 mm above the attached *x*-MF (red lines in Figure 2.2c). Tensile tests were performed with 0.1%-gauge length/second displacement speed, and force-displacement curves were obtained. Moreover, one sample of a more complex configuration was tested: three *x*-directed MFs glued to one *y*-directed MF (1 mm distant), perpendicular to the three MFs (Figure 2.2d).

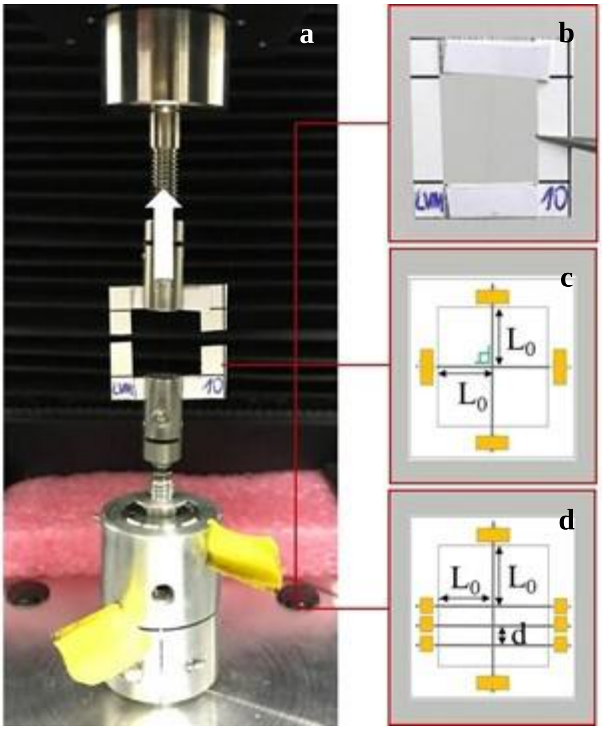

Figure 2.2 a) Nanotensile machine used to perform tensile tests on single and interconnected fibres. On the right the samples mounted on the paper frame are schematised: b) single fibres, c) two perpendicular fibres joint with glue and. The red lines mark where the sample is cut before being tested. d) Sample with one y-directed fibre and three x-directed fibres (d=1mm), joint with glue at each intersection point.

2.4. Analytical model of the single and interconnected microfibres

2.4.1 Analytical model of the mechanical behaviour of the microfibres

Given the mechanical properties obtained with tensile tests (paragraph 3.1), an analytical model of the mechanical behaviour of the fibres was defined. Since the final users of this work are surgeons and technicians who handle and position the device, a practical description of the mechanical performance of the electrodes is proposed. Three main issues were identified in handling and grafting the electrodes. First, the electrodes are pulled in the spinal cord tissue when the device is being grafted, and damages to the device could occur. To be placed, the electrodes undergo bending. When the device is handled, the fibres undergo damages caused by their contact. Considering the described issues, the behaviour of the different tested electrodes was modelled through three parameters: Easy initial penetration, Easy manipulation, and Curvature.

MFs location is performed by pulling the ends of the MF-based device inside the healthy tissue upward and downward the damaged spinal cord, bridging the lesion [9]. During this delicate procedure, the detriment of the fibres could occur, causing delays in the procedure and waste of material. The Easy Initial Penetration (*EIP*) parameter was defined to quantify if an electrode is suitable to be pushed in the host tissue without damages. This condition is associated with a beam of length l pinned at the two ends, loaded with a load reaching elastic instability (i.e., buckling). The buckling critical stress (σ_{cr}) defines the maximum axial stress that a long, slender, ideal beam can carry without buckling:

$$\sigma_{cr} = \pi^2 E/\lambda^2 \tag{2.2}$$

where E is the Young's Modulus of the beam and λ is the slenderness ratio, defined as $\lambda = l/\rho_{min}$. The cross-section minimum radius of gyration ρ_{min}^2 of the beam is defined as

$$\rho_{min}{}^2 = \frac{I_{min}}{A} \tag{2.3}$$

where I_{min} is the minimum moment of inertia ($I_{min} = \frac{\pi R^4}{4}$ for a filled circular area of radius R) and A is the cross-sectional area of the beam. By replacing the slenderness ratio formula in σcr the result is

$$\sigma_{cr} = \frac{\pi^2 E R^2}{4L_0^2} \tag{2.4}$$

Under the assumption of fibres with equal length and a circular cross-sectional area, it is possible to avoid geometrical and constant factors, common to every type of fibre. Thus, considering these simplifications, the Easy Initial Penetration results in $EIP \propto ER^2$, showing that increasing the radius of the fibre decreases damages.

A detrimental condition for the electrodes is their contact when handled. Hertzian Theory of contact mechanics focuses on the deformation of solids in contact at one or more points, and fibre-fibre contact could be studied as the generic case of contact between two cylinders of equal radius *R*. This generic case is equivalent to the contact between a sphere of the same radius *R* and a plane [134]. When an elastic sphere of radius *R* is in contact with an elastic half-space, the normal maximum contact pressure (p_0) in the contact area is given by:

$$p_0 = \frac{1}{\pi}(\frac{6FE^2}{R^2})^{1/3} \qquad (2.5)$$

The worst-case was analysed: the ultimate normal stress of the MF (σ_u) equal to the maximum contact pressure $p_0^3 = \sigma_u^3$. The maximum force exerted during contact (*F*) corresponding to the normal stress σ_u was obtained:

$$F = \frac{{\sigma_u}^3\pi^3R^2}{6E^2} \qquad (2.6)$$

Neglecting the constant values, the Easy Manipulation (*EM*) term is defined as $EM \propto \frac{{\sigma_u}^3R^2}{E^2}$, thus identifying the maximum force that can be applied to fibres in contact with each other's while avoiding their breakage. This parameter is useful to control how to handle the device: the higher is the value of *EM*, the lower is the probability of damages due to contact. Moreover, *EM* identifies which tools (i.e., tweezers) should be used to pick the device, in terms of maximum pressure and force applied.

The manipulation (e.g., by the surgeon) of MFs while being placed in the injured area can be modelled as an applied bending moment (*M*). The curvature (*X*) quantifies the maximum bending of a structure before breaking. *X* is linked to the bending moment through the relation $X = \frac{M}{EI}$. Under the assumption of a bending moment operating in the yz plane, the *y*-linear strain (ε) along the *z*-axis is defined as $\varepsilon = \frac{yM}{EI}$. Considering the ultimate strain (ε_u) and thus $y_{max} = R$:

$$\varepsilon_u = \frac{M}{EI}y_{max} = \frac{M}{EI}R \qquad (2.7)$$

Using a linear elastic relation, the ultimate strain is defined as $\varepsilon_u = \frac{\sigma_u}{E}$. Combining the latter equations, $\frac{\sigma_u}{E} = \frac{M}{EI}R = XR$. Thus, the curvature *X* becomes:

$$X \propto \frac{\sigma_u}{ER} \tag{2.8}$$

Curvature is also defined as the inverse of the radius of curvature (r): $X = \frac{1}{r}$, which quantifies the minimum radius of the circle drawn by bending the MF: the smaller is the radius, the more the MF bends without breaking.

2.4.2 Analytical calculations on the simplified prototype

The behaviour of samples composed of two interconnected MFs during tensile tests was described with an analytical model. The stiffness of the joint is here considered infinite, and the system tested with tensile tests (Figure 2.2c) is simplified. Indeed, the model considers a single elastic fibre (the length is $2L_0$) clamped to a scaffold and pulled by a force F from its midpoint, along the orthogonal direction (Figure 2.3, left).

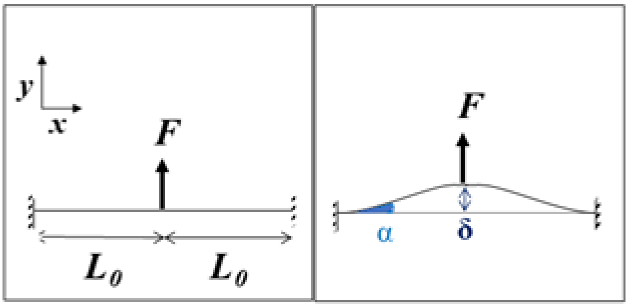

Figure 2.3 Schematic of the force acting on a simplified junction before (left) and during (right) the tensile test.

If T is the elastic force of the fibre, the equilibrium is obtained by the condition:

$$F = 2Tsen\alpha \tag{2.9}$$

The force can be expressed in terms of the displacement δ of the midpoint (Figure 2.3, right), observing that $\delta = Lsin\alpha$ and $L^2 = \delta^2 + L_0^2$, where L is the length of one arm of the fibre after the force is applied. Bending phenomena were not considered. Moreover, given the elastic constant K of the fibre, the elastic force can be written as $T = K(L - L_0)$. By substituting these relations into equation 2.9 the following equation is obtained:

$$F = 2\,K\,(L - L_0)\frac{\delta}{L} = 2\,K\,\delta\,(1 - \frac{1}{\sqrt{1 + \frac{\delta^2}{L_0^2}}}) \qquad (2.10)$$

Finally, the two limits by Taylor are calculated by expanding the expression on the right side of (2.10):

$$F = f(x) = \begin{cases} 2\,K\,\delta & if\ \frac{\delta}{L_0} \to \infty \\ K\,\delta^3 L_0^{-2} & if\ \frac{\delta}{L_0} \to 0 \end{cases} \qquad (2.11)$$

Thus, for the force-displacement law, a linear elastic behaviour with elastic constant 2*K* for large δ and a cubic power law for smaller values are expected. As a first approximation, in the presence of n fibres pulled from the midpoint, the same formulas hold if the elastic constant *K* is substituted with *nK*. This approximation assumes that all the fibres have the same deformation and angle α. The maximum force reached during each test was defined as the resistance of the junction.

2.5. Numerical model of the ISMS device prototype

2.5.1. Numerical model formulation

An ad hoc in-house developed numerical model for the interconnected MFs used in the experimental tensile tests was developed. The model considered *N* fibres placed along the *x*-axis (labelled with x-fibre$_i$, i=1,2,3…), whose edges are attached to a rigid scaffold, and one fibre orthogonal to the x-fibres$_i$ and pulled along the *y*-axis. The letters x and y identify the initial alignment concerning the pulling direction, i.e. along the *x* or *y* direction, respectively. The *x* and *y* directed fibres are attached at their intersection points, as displayed in the example with three *x*-fibres of Figure 2.4. Geometric parameters are the following:

- Length of the x-fibres$_i$: $2L_0$=11 mm
- Distance between the *x*-fibresi: *d* = 1 mm
- Length L_0 from the junction with *x*-fibres3 to the edge of the *y*-fibre: = 5.5 mm
- Total length of *y*-fibre: $L_y = L_0 + (N - 1) \cdot d$ mm.

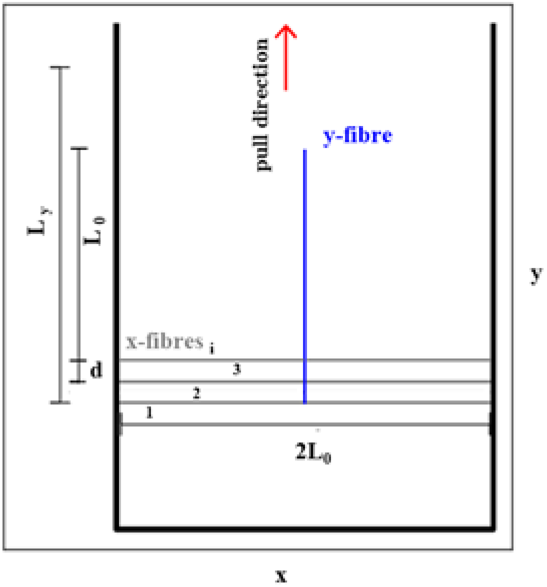

Figure 2.4 Schematic of the simplified model of the final device with three x-directed fibres.

Material parameters are Young's modulus E, the mass density ρ, and fibre diameter $\varnothing$, so that the section is$A = \pi \varnothing^2/4$. To simulate the system behaviour during the tensile test, each fibre was discretised into a one-dimensional chain of springs and masses. Given a discretization length l, each fibre will be divided into $N = L/l$ segments, characterized by a stiffness $K = EA/l$. Thus, each fibre was characterized by $N+1$ masses $m = Al\rho$, except those located at the edges of the fibre, having mass $m/2$. Denoting the position vector of a generic mass i with $r_i = (x_i, y_i)$, the force exerted on i by a neighbouring mass j can be written as

$$F_{junction}^{ij} = K(r_{ij} - l)(r_i - r_j)/r_{ij} \qquad (2.12)$$

where $r_{ij} = |r_i - r_j|$ is the modulus of their distance.

The junctions between orthogonal fibres were composed of two masses i and j belonging to a x and y- fibre, respectively, located at their intersections. These are attached using a spring with zero rest length and stiffness K_{junc}, so that the force exerted between them is $F_{junc}^{IJ} = K_{junct}(r_i - r_j)$. Finally, a viscous damping force is applied to each

mass to avoid artificial oscillations, $F_d^i = \gamma m v_i$, where v_i is the velocity vector.
To perform the tensile test, the mass at the right edge of y-fibre, concerning Figure 2.4, was shifted along the positive y-direction with a rate v, while masses at the edges of x-fibres were attached to the scaffold and cannot move during the time evolution. These are the boundary conditions of the system. Thus, Newton's equations for generic block i, except those involved in the boundary conditions, can be written as:

$$m\,\ddot{r} = \sum_j F_{int}^{ij} + F_{junc}^{ij} + F_d^i \qquad (2.13)$$

where the sum includes only the neighbouring masses and F_{junc}^{IJ} must be included only for blocks belonging to the intersections. The system of equations can be solved with a fourth order Runge-Kutta algorithm. An integration time step $dt = 10^{-9} s$ was sufficient to avoid integration errors.
The unknown parameters were damping parameter γ, the stiffness K_{junc}, and the discretization length l. The first one can be arbitrarily fixed with the $\gamma < \sqrt{K/m}$, i.e., in the underdamped regime, and $\gamma = 50\ \mathrm{ms}^{-1}$ was adopted. Based on experimental data, suggesting that the junction stiffness is larger than the fibre ones, K_{junc} is fixed to $10K$, so that it can be considered inextensible. The rate of the tensile test was fixed at the same value of the experimental measurements, $v = 0.01$ mm/s. The discretization length was fixed to $l = 0.11$ mm, which, given the material parameters, was sufficient to calculate the stress distribution and the global observables to be compared with experiments avoiding discretisation errors.

3. Results and discussions

3.1. A comprehensive description of the mechanical performance of the electrodes for ISMS

The mechanical properties obtained with the tensile tests and the analytical practical parameters of the MFs are summarized in Table 2.1. This table aims at identifying the more suitable MF to be used as an electrode in the final design of the ISMS device. The best value obtained for each parameter is identified with ranking from 1 (best) to

10 (worst) (*Rank* row). Differences among types of MFs are reported, and the percentage of each value with respect to the best one is included (*%* row). The best value obtained for ultimate strength, strain at break, Young's modulus, toughness modulus, Easy Initial Penetration, Easy manipulation, and curvature is the highest value. Table 2.2 summarises all the MFs information, being also the final tool for the users (i.e., surgeons, technicians, engineers) who have to choose the best MF to be used as an electrode, i.e., the golden mean. Carbon fibres reach first place in the greater number of properties. Considering the coated fibres, carbon MFs coated with PEDOT:PSS-co-MA reached the highest ranking in most of the properties considered, followed by cobalt alloy MFs coated with PEDOT:BFEE.

Table 2.2 Mechanical properties of the tested microfibres. σu is the ultimate strength, εu is the strain at break, E is the Youg's modulus, T is the toughness modulus, EIP is the Easy Initial Penetration, EM is the Easy Manipulation, X is the curvature. Every type of tested fibre presents, for each property, the property directly or indirectly calculated with the tensile test. The percentage of the value with respect to the best one (i.e. the highest one, for example, the stainless steel fibres presents an ultimate strain that is the 50% of the carbon MF one, which has the highest value) are listed in the % row. The values obtained for the specific property are also ranked from 1 (lowest) to 10 (highest) (rank row) to help the recognition of the MF with the best mechanical performance (i.e. the "golden mean").

	Bare carbon	Stainless steel	Cobalt-based alloy	Gold
σ_u [GPa]	4.203±0.674	2.121±0.425	2.728±0.309	0.373±0.026
%	100.00%	50.47%	64.91%	8.88%
rank	**1**	5	3	10
ε_u [mm/mm]	0.017±0.003	0.019±0.006	0.020±0.003	0.017±0.221
%	27.28%	30.28%	32.19%	27.10%
rank	8	6	5	9
E [GPa]	272.478±33.454	185.151±13.709	197.867±25.469	71.784±12.180
%	100.00%	67.95%	72.62%	26.34%
rank	**1**	3	2	10
T [J/g]	15.351±4.240	2.874±1.316	3.464±0.781	0.146±0.071
%	100.00%	18.72%	22.57%	0.95%
rank	**1**	5	4	10
EIP $E \cdot R^2$ $[Pa \cdot m^2]$	3.338	7.466	7.979	1.795
%	41.84%	93.57%	100.00%	22.49%
rank	7	2	**1**	10
EM $\sigma^3 \cdot R^2 / E^2$ $[Pa \cdot m^2]$	$1.225*10^{-5}$	$1.122*10^{-5}$	$2.091*10^{-5}$	$2.518*10^{-7}$
%	35.89%	32.89%	61.26%	0.74%
rank	5	6	2	10
X $\sigma / E \cdot R$ $[1/m]$	4406.791	1804.080	2171.112	1039.229
%	94.10%	38.52%	46.36%	22.19%
rank	2	7	6	10

	Platinum	Carbon+ PEDOT:PSS-co-MA	Stainless steel+ PEDOT:PSS-co-MA
σ_u [GPa]	0.864±0.102	2.857±0.294	1.321±0.947
%	20.55%	67.98%	31.43%
rank	9	2	7
ε_u [mm/mm]	0.017±0.009	0.025±0.008	0.039±0.018
%	27.29%	39.85%	62.16%
rank	7	4	2
E [GPa]	160.305±22.253	152.520±13.523	124.832±18.229
%	58.83%	55.98%	45.81%
rank	4	5	7
T [J/g]	0.154±0.052	11.676±2.291	2.023±0.788
%	1.00%	76.06%	13.18%
rank	9	2	8
EIP $E\cdot R^2$ $[Pa\cdot m^2]$	4.008	2.440	5.857
%	50.23%	30.59%	73.42%
rank	6	8	4
EM $\sigma^3\cdot R^2/E^2$ $[Pa\cdot m^2]$	$6.267*10^{-7}$	$1.604*10^{-5}$	$6.941*10^{-6}$
%	1.84%	47.00%	20.34%
rank	9	4	7
X $\sigma/E\cdot R$ [1/m]	1077.533	4682.992	1544.850
%	23.01%	100.00%	32.99%
rank	9	**1**	8

	Carbon+ PEDOT:BFEE	Stainless steel+ PEDOT:BFEE	Cobalt+ PEDOT:BFEE
σ_u [GPa]	1.024±0.018	1.585±0.207	2.386±38.179
%	24.37%	37.72%	56.76%
rank	8	6	4
ε_u [mm/mm]	0.013±0.005	0.039±0.009	0.063±0.027
%	20.72%	61.59%	100.00%
rank	10	3	**1**
E [GPa]	113.675±49.030	98.070±6.498	136.618±4.312
%	41.72%	35.99%	50.14%
rank	8	9	6
T [J/g]	2.625±1.421	2.587±0.563	3.732±0.362
%	17.10%	16.85%	24.31%
rank	6	7	3
EIP $E \cdot R^2$ [$Pa \cdot m^2$]	1.819	4.602	4.411
%	22.80%	57.68%	80.35%
rank	9	5	3
EM $\sigma^3 \cdot R^2 / E^2$ [$Pa \cdot m^2$]	$1.330*10^{-6}$	$1.943*10^{-5}$	$3.413*10^{-5}$
%	3.90%	56.93%	100.00%
rank	8	3	**1**
X $\sigma / E \cdot R$ [1/m]	2252.034	2359.531	2549.041
%	48.09%	50.39%	54.43%
rank	5	4	3

The coated MFs resulted in a minor Young's modulus than the corresponding bare fibres. Considering the bare fibre and the coating as two strings in parallel, the total tensile force (F) is distributed on the coating (F_c) structure and the bare MF (F_f), namely:

$$F = F_c + F_f \tag{2.14}$$

Thus, the Young's modulus results:

$$E = E_c(1 - \frac{{R_f}^2}{{R_c}^2}) + E_f \frac{{R_f}^2}{{R_c}^2} \tag{2.15}$$

Where R_c is the radius of the coated fibre and R_f is the radius of the bare MF. The tensile tests results showed that the coated MFs rigidity (EA) is smaller than that of the corresponding bare MFs. The meaning of such results is a decrease in the elastic modulus of the bare MF due to the coating treatment. MFs coated with PEDOT:BFEE are thus strongly affected by the treatment that considerably reduces the elastic modulus of the bare MFs.

A likely pullout phenomenon was recorded while testing the coated MFs. Indeed, one sample of each type of coated fibre presented a stress-strain curve characterised by a first linear tract with a higher slope with respect to other similar samples, followed by a stress plateau or a tract with a significantly lower slope, then followed by a slope increase.

Considering the coating-fibre joint as a tubular adhesive joint, the adhesion energy of the coating on the bare MF was calculated according to Pugno et al [135]:

$$F_p = 2\pi R\sqrt{ERG} \tag{2.16}$$

Where F_p is the force recorded during pullout, R is the radius of the bare MF, E is Young's modulus of the bare fibre, and G is the adhesion energy of the delaminated interface (Table 2.3). Visual inspection suggests that the MF-coating interface is the weakest, and the G value is a measure of their interaction.

Table 2.3 Estimation of the interface adhesion energy (G).

	Carbon+ PEDOT: PSS-co-MA	**Stainless steel+ PEDOT: PSS-co-MA**	**Carbon+ PEDOT: BFEE**	**Stainless steel+ PEDOT: BFEE**	**Cobalt+ PEDOT: BFEE**
***G* [N/m]**	9.68	0.77	20.78	5.14	7.82

Comparing the two types of coating, the adhesive energy was higher in PEDOT:BFEE compared to PEDOT:PSS-co-MA.

3.2. Mechanical properties of the interconnected microfibres

Tensile tests were performed on two perpendicularly interconnected MFs to investigate the behaviour of the joint and the overall system. The results obtained with tensile tests on two cross connected MFs (Figure 2.2c) showed a reduction in the maximum force compared to the single fibres (22.10±9.38 mN VS 161.74±25.96 mN). The maximum displacement reached by the interconnected MFs under tensile load was 3-fold higher (0.84±0.33 mm) than the one reached by the single MFs (0.26±0.04 mm). A more complex system composed of one *y*-directed fibre and 3 *x*-directed fibres, connected with glue, was tested. However, not repeatable results were obtained due to technical difficulties during the production of the sample and the test. Indeed, high variability was obtained in the force-displacement curves. However, Figure 2.5 shows that the tensile force of this more complex system behaved as the samples with one single joint up to the breakage of the first joint, suggesting a cumulative behaviour of the force. The joints broke from the bottom toward the applied force, the one in the middle and the upper one broke almost simultaneously.

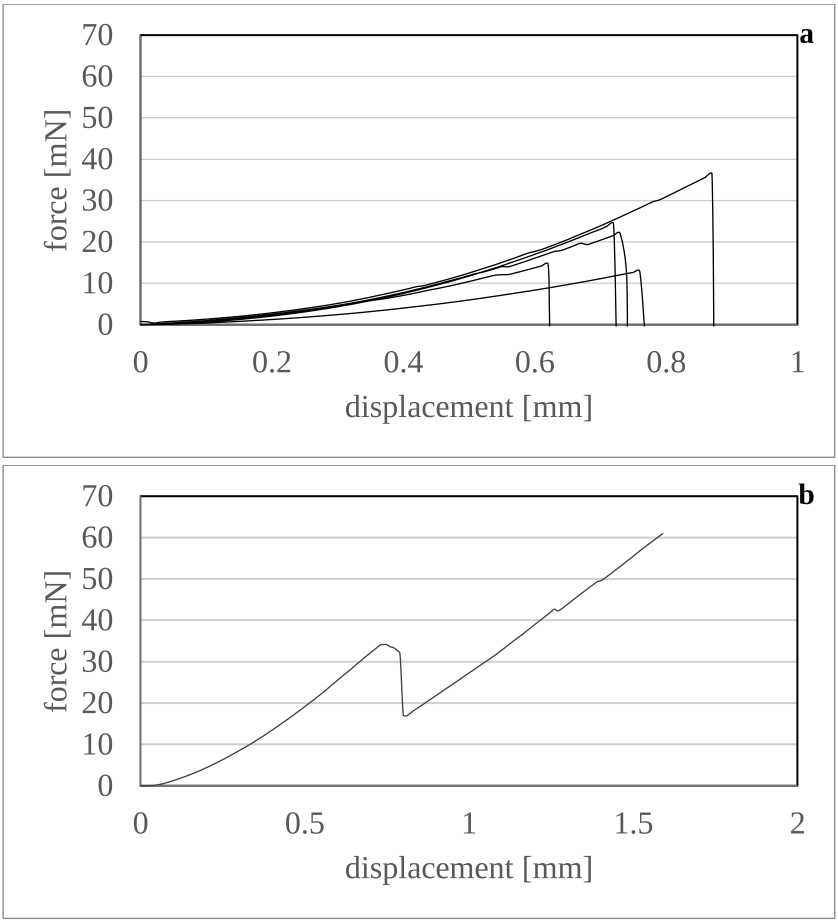

Figure 2.5 Force-displacement curve of two perpendicularly interconnected carbon MFs (a) and a system of one y-directed MF and three x-directed MFs (b).

3.3. Analytical model results

The analytical model was applied to the expected theoretical data and the results obtained are presented in Figure 2.6.

Moreover, the best fit was performed on the experimental data. During tensile tests, the measured displacement (by the machine) is the one of the trailing edge of the *y*-fibre (i.e. the total displacement composed by the one of the midpoint *δ* (Figure 2.3) and the one due to the deformation of the *y*-fibre). Thus, in equation 2.10, δ was replaced with the machine displacement. After this substitution, a numerical implicit best fit was performed, where parameter a represents the stiffness K of the carbon MF. The fitting equation resulted:

$$y - 2a\left(x - \frac{y}{a}\right)\left(1 - \frac{1}{\sqrt{1 + \frac{\left(x - \frac{y}{a}\right)^2}{L_0^2}}}\right) = 0 \qquad (2.17)$$

Where y is the force, x is the displacement, and L_0 is the length of one of the two arms of the fibre. The force (y) was calculated considering the experimental displacement recorded during tensile tests.

Using equation 2.17, a resulted in 1544.68±797.61 N/m and the R^2=0.98. The theoretical stiffness of the single MF under uniaxial tensile load is $K = EA/l_0 = 1906.60\, N/m$, and thus the result obtained by fitting the experimental data is consistent with the expected K, within the experimental uncertainty. Back calculating Young's modulus of the system, a value of 220.76±113.99 GPa was obtained (Young's modulus of the single fibre is 272.48 GPa).

Furthermore, the fitting was also performed considering the expression for $\delta/l_0 \to 0$, $y = bx^3/L_0^2$. Since $\theta \sim \sin\theta \sim \tan\theta$ (Figure 2.3). The parameter b, states for the stiffness of the fibre K, resulting in 1461.48±782.03 N/m, similar to a, obtained with the first approach. Figure 2.6 reports the results obtained with the best fit and the analytical model.

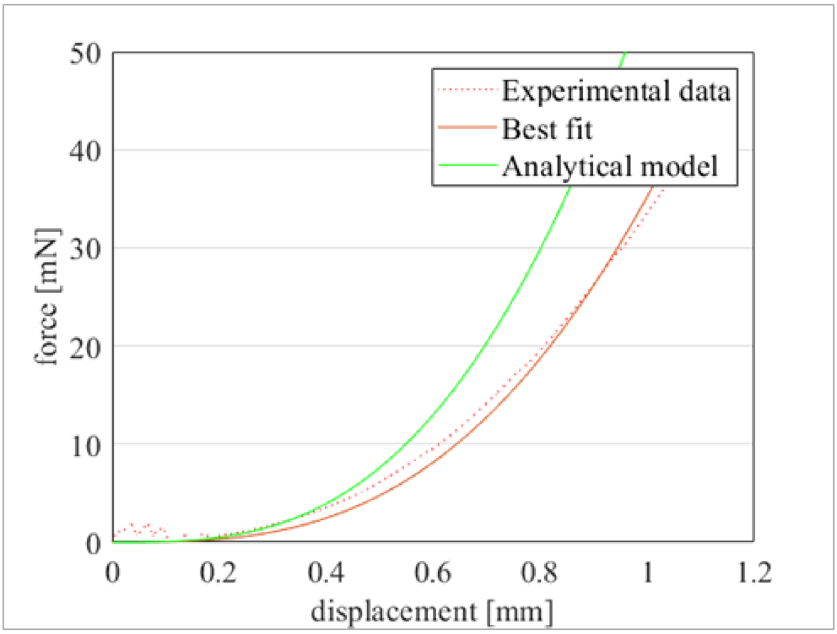

Figure 2.6 Comparison of the force-displacement plots of the sample with one x and one y-directed fibre resulting from: tensile test on a carbon MF (Experimental data), the best fit on the experimental data using equation 2.17, and the analytical model.

3.4. *Numerical model results*

After an initial transient regime characterized by damped oscillations, the system assumed the configuration shown in Figure 2.7, in which all the fibres are progressively stretched in a quasi-static regime without oscillations. Naming P the trailing edge of *y*-fibre that is shifted at a constant rate, the main observables are:

- The total force F_P applied on *P*, corresponds to the force measured in a tensile test.
- The total strain ε_y of the *y*-fibre fibre along *x* axis, is calculated as the total stretching normalized with the total length, i.e., $\varepsilon_y = (x_P - x_{J1} - L_y)/L_y$.
- Strain distribution along all fibres: given two neighboring points *i,j*, the local strain can be calculated as $(d_{ij} - l)/l$, where d_{ij} is the distance between the two points.
- Displacements δ_i are the ones of the first *x*-fibre from the original position.

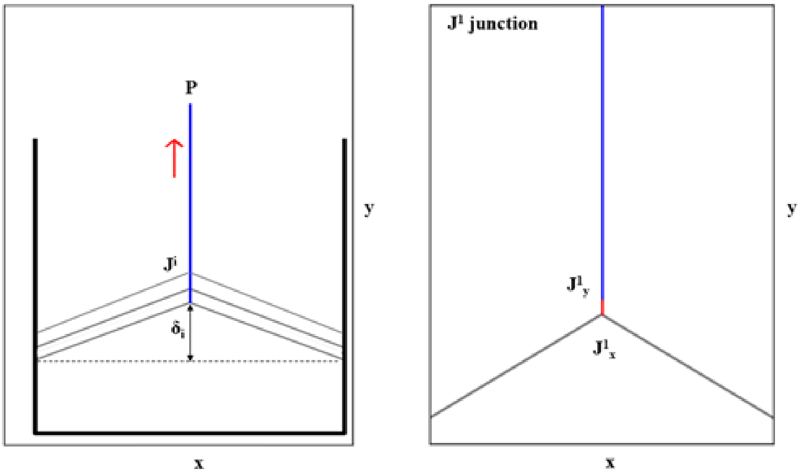

Figure 2.7 Configuration of the simplified model after an initial transient regime of damped oscillations and consequent application of a y-directed load (left) and focus on one junction (right).

Considering a sample composed of one x and one *y*-directed fibre, Figure 2.8 summarises the force-displacement plots obtained with the three approaches: the experimental tensile test, the best fit performed on the experimental data using equation 2.17 (which originated from equation 2.10), the analytical model and the numerical model. Considering the simplified numerical model with one *x*-directed fibre, after the initial stage, the increase of the forces is roughly linear with the time, as could be expected from the analytical solution, although a nonlinear phase of various durations depending on the observables is found. This behaviour for the case of one *x*-fibre is perfectly consistent with the analytical solution.

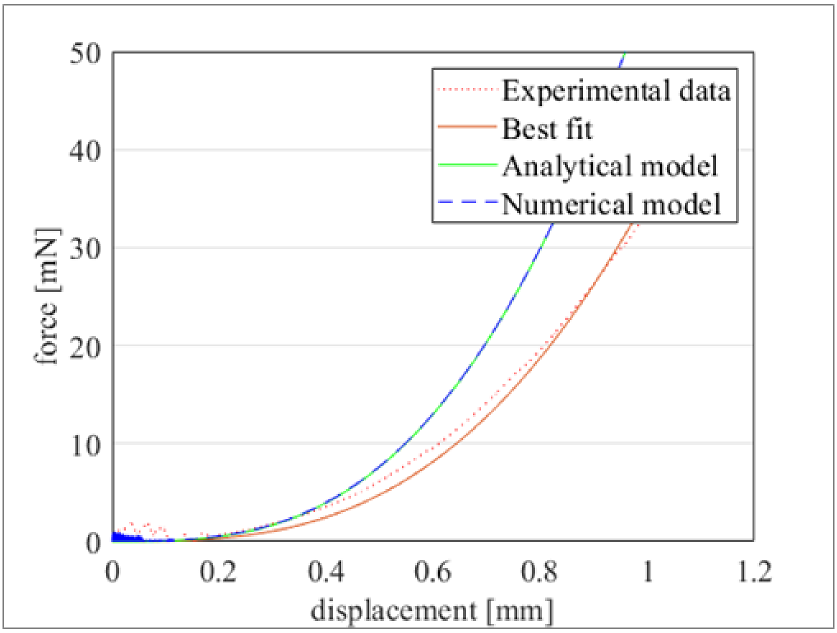

Figure 2.8 Comparison of the force-displacement plots of the sample with one x and one y-directed fibre resulting from: tensile test on a carbon MF (Experimental data), the best fit on the experimental data using equation 16, the analytical and the numerical model.

Considering the configuration with 3 *x*-fibres, stretching is increasing from the first to the last one ordered towards the positive direction of the *y* axis (from 1 to 3), but there are only a few percent deviations between them, due to the assumption that all the *x*-fibres are equally stretched. The model was also checked in the configuration with 5 *x*-fibres. The results obtained considering 1, 3, and 5 *x*-fibres are summarised in Figure 2.9.

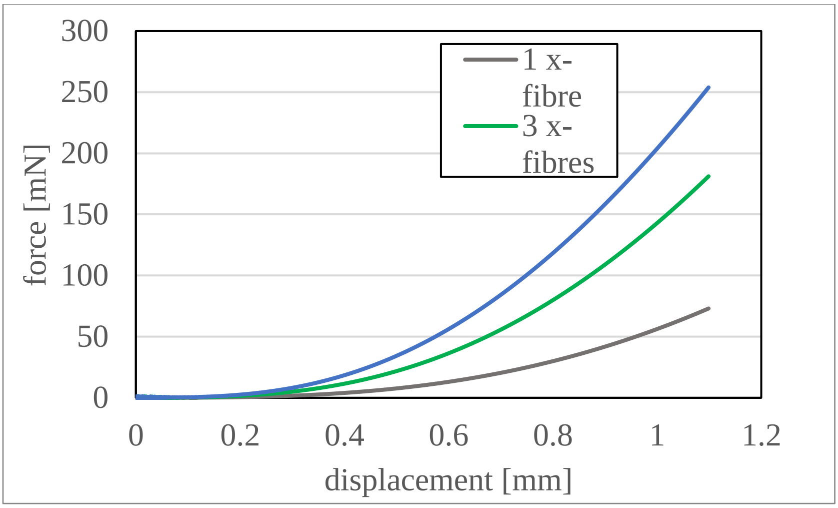

Figure 2.9 Results of the numerical model obtained considering three configurations: 1 (grey), 3 (green), and 5 (blue) x-fibres.

In Figure 2.10 the strain distribution along the fibres is shown as a function of the normalized length, for four applied displacements. Assuming perfect attachments and junctions, the maximum strain is found for *x*-fibres at the early stage of the tensile test, whereas for large displacement applied, the maximum strain is found for the *y*-fibre. Thus, if the x and y fibres break at the same maximum strength, the point with a larger rupture probability depends on the total applied displacement. Moreover, the strain distribution appears approximately uniform for the *x*-fibres, whereas is increasing towards the tip of the y fibre, but with a stepwise shape across each junction.

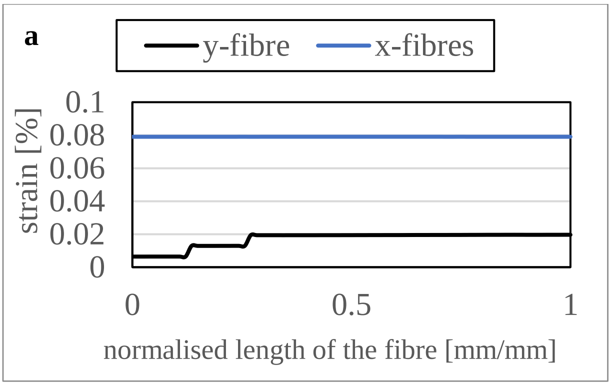

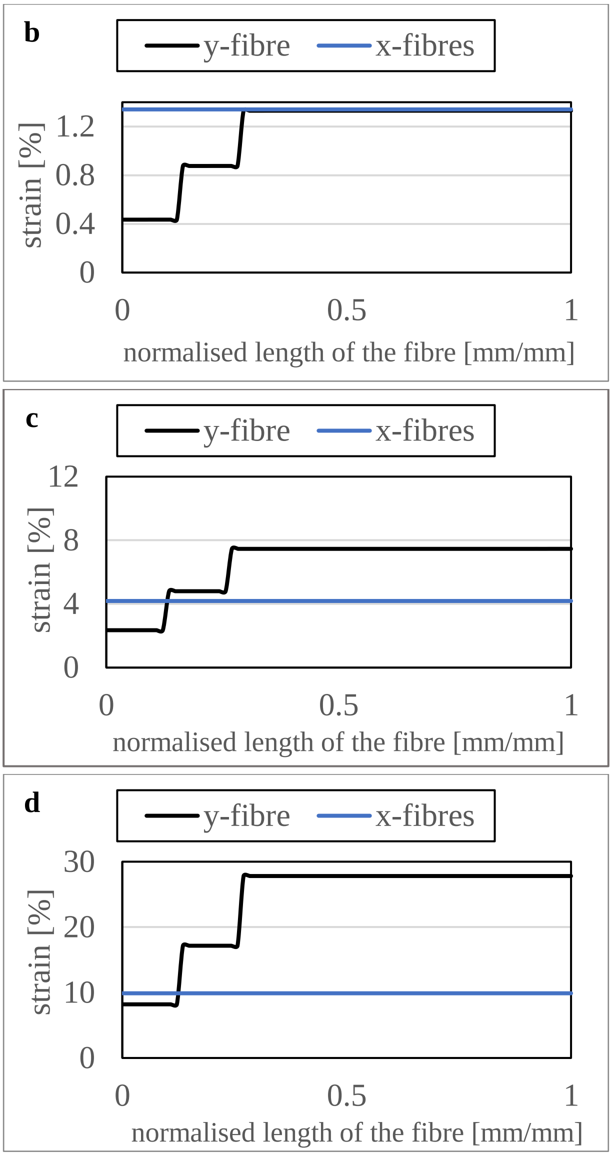

Figure 2.10 Strain field (modulus) for y (black) and x (blue) fibres as a function of their normalised length, corresponding to different displacement δ during the application of a tensile force. a) δ=0.22 mm, b) δ=0.99 mm, c) δ=2.1 mm, d) δ=4.3 mm.

4. Conclusions

The work here described is part of the ISMS device designing process. The tensile tests performed on different types of MFs and the analytical parameters endorsed carbon microfibres as the electrodes with the best mechanical performance. Table 2.2 shows that carbon MFs are firsts in the ranking of several mechanical properties, such as strength, strain at break, Young's modulus, and toughness modulus. Carbon MFs were also the bare fibres with the highest curvature. Carbon MFs coated with PEDOT:PSS-co-MA resulted first in the rankings of the majority of the considered properties.

An easy-to-use template to follow for the evaluation of the performance of different electrodes and to support the choice of the best product was provided. Through this procedure, the assessment of the mechanical performance of the electrodes is not limited to the choice of an electrode with a stiffness similar to the spinal cord tissue and/or high enough to enable the insertion without breaking [18], [19], [136]. Indeed, the method includes three analytical parameters to define the behaviour and limits of the electrodes in specific practical scenarios, such as the insertion of the electrode in the tissue, the maximal curvature possible prior braking, and eventual issues due to the contact between the electrodes. The table could be a useful hint to plan the best strategies for the device design and grafting. For example, EIP and X could be in contrast, since EIP increases with the radius of the fibre, and to obtain high curvature and avoid breakage small radii are needed. The golden mean solution could be using electrodes with a small radius and implanting them in the tissue as a bundle, checking the threshold imposed by the EM. Grafting a device made of a group of MFs close to each other, thus creating a bundle of bigger radius, could permit the use of compliant MFs.

The coating treatment of the MFs showed a general decrease in the strength and stiffness concerning the corresponding bare fibres, suggesting possible damages. Comparing PEDOT:PSS-co-MA and PEDOT:BFFE, the latter resulted in higher adhesion energies with the bare fibre, even though considering only one test for each type of bare fibre-coating couples.

The value of Young's modulus obtained from the best fit of the two interconnected MFs was slightly different from the modulus calculated from the tensile tests (220 vs 270 GPa circa). This difference can be ascribed to the bending stiffness of real fibres that was not considered in the simplified model and to the simplification of considering the displacement of the joint as the total displacement recorded during a tensile test, thus not considering the deformation of the *y*-directed fibre. However, the analytical model well fitted (R^2>0.9) the evolution of the force during tensile tests on two interconnected MFs, thus describing the behaviour of the joint. Moreover, by fitting the experimental data with equation 2.17, the calculated stiffness (i.e., parameter a) was consistent with the expected K, within the experimental uncertainty.

The force-displacement plots obtained with the tensile test, the analytical model, the numerical model, and the best fit performed on the experimental data well coincided. The force reached by the numerical model of the three different configurations of the simplified device (1, 3, and 5 x-fibres) increased when increasing the number of fibres. Dividing the force corresponding to large displacements by the number of x-fibres, the forces obtained corresponded with the one recorded when considering 1 x-fibre. This result was expected by the analytical model.

Work performed in collaboration with Dr. Gianluca Costagliola (Civil Engineering Institute, Materials Science and Engineering Institute, École Polytechnique Fédrale de Lausanne (EPFL), CH-1015 Lausanne, Switzerland), who performed the analytical and numerical calculations, and Jorge Collazos-Castro (Neural Repair and Biomaterials Laboratory, Hospital Nacional de Parapléjicos (SESCAM), Finca la Peraleda s/n, 45071 Toledo, Spain) who provided the MFs and the samples coated with conducting poly

Chapter 3 Coating carbon microfibres with graphene: an experimental study of mechanical and surface properties

1. Introduction

Carbon microfibres have been studied as implantable electrodes for ISMS due to their combination of favorable small dimensions, mechanical properties, and high electrical conductivity (104 S/m circa) [137]. However, these properties could be improved with graphene. Since graphene-based interfaces were proven suitable for neural applications [138], coating carbon MFs with graphene could lead to high-performance electrodes for ISMS. This work aims to investigate eventual modifications in the bulk and surface properties of polyacrylonitrile (PAN) carbon MFs after their coating with graphene. Tensile tests were performed to obtain the mechanical properties of the MFs. Through the Wilhelmy balance method, the dynamic advancing and receding contact angles were measured [25], [26]. Finally, the surface free energy of fibres was calculated using the Lewis acid/base multicomponent approach [27].

2. Materials and methods

2.1. Samples

Five types of graphene-coated PAN carbon MFs were provided by Cambridge Graphene Center (UK): carbon MFs (Goodfellow) with a patchy spray coating of GO, carbon MFs with a patchy spray coating of reduced GO (RGO), carbon MFs fully spray-coated with RGO, Chemical Vapor Deposition (CVD) graphene-coated carbon MFs, and High Pressure Homogenization (HPH) graphene ink coated MFs. The diameter of the bare and coated MFs was 7 µm circa (the coating was a few nm thick). These samples and the bare carbon fibres were characterised with tensile tests to evaluate their mechanical properties. The coated MFs with the most different mechanical properties with respect to the bare ones were selected to undergo surface analysis.

2.2. Tensile tests

Tensile tests were performed to assess the mechanical properties of the bare and coated MFs. The fibres were mounted on a paper frame with an 11x11 mm square window. The samples were tested with an Agilent T150 UTM nanotensile machine imposing a testing speed of 0.1%-gauge length/second. The force-displacement curves obtained with the tensile tests were processed to obtain the ultimate strength (σ_u), the strain at break (ε_u), Young's modulus (E), and the toughness modulus (T). The engineering strength was computed by dividing the force for the cross-sectional area (circular) of the microfibre, and the engineering strain was obtained by dividing the displacement for the gauge length of the sample (i.e., initial length, 11 mm). The ultimate strength was the engineering stress reached before fracture and the strain at break was the corresponding strain. Young's modulus was calculated as the slope of the stress-strain curve. The toughness modulus was considered as the area under the stress-strain curve, divided for the volumetric density (ρ_{carbon}=2.25 g/cm^3).

2.3. Surface analysis

The surface energy (i.e., wettability) of MFs was estimated starting from the Wilhelmy Balance method. It is a widely used technique that indirectly measures dynamic advancing and receding contact angle on a solid sample [25], [26]. Figure 3.1 shows a simplified scheme of the sample preparation and the experimental setup.

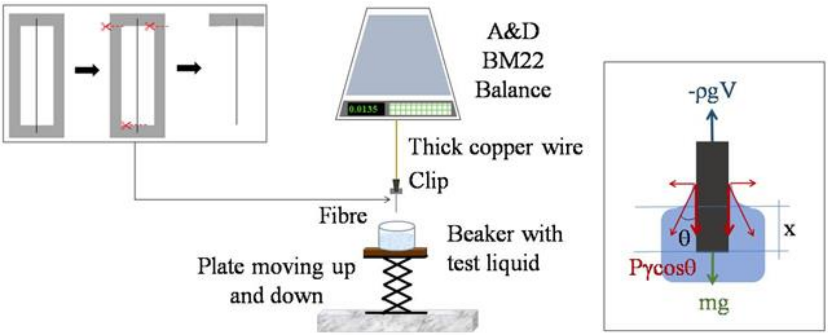

Figure 3.1 Sample preparation: the MF was mounted on an aluminium foil frame, that was cut along the red lines before testing (left). The sample was then hanged under the balance and the Wilhelmy measurement was performed (center). When the fibre is in contact with the test liquid, the change in its weight is detected by a balance and this force depends on the combination between weight force (mg), wetting force (Pγ), buoyancy (ρgV) (right).

Fibres were 15 mm in length. First, each fibre was mounted on an aluminium sample holder (Figure 3.1, left) and fixed through a minimum amount of glue on both ends. Aluminium was chosen since it does not absorb vapours. Indeed, in a microgram context, even the smallest noise disturbs the measurement. Before testing, one of the ends was cut, part of the holder was removed (Figure 3.1, left), and the sample was suspended to the Wilhelmy support (Figure 3.1, middle). Fibres were always discharged before being tested, to avoid electric noise. A&D BM22 Ion Series Microbalance was used to weigh fibres according to the Wilhelmy method during contact angle calculation. The sample was directly hung under the balance plate. The test liquid was inside a short-wall glass beaker to avoid solvent vapor formation and consequent absorption by the sample. 5 mm-distance of the sample from the borders of the container was observed to avoid the formation of a capillary bridge that could affect the measurement [26]. The beaker was placed under the sample, on a mobile plate. The sample was maintained, and a small engine moved the plate and the beaker full of liquid under it. The plate displacement was set at 10 mm back and forth, at a controlled speed (0.01 mm/s).

When the fibre is brought in contact with a liquid, the change in its weight (i.e., force) is detected by the balance. This force depends on the combination of weight force (mg), wetting force ($P\gamma$), buoyancy ($\rho g V$), and friction (*f(v)*) (Figure 3.1, right) [26]. The horizontal components of the surface tension of the liquid γ are equal and opposite due to the axisymmetry (cylindric) of the sample. The net final force is thus only vertical:

$$F(x) = mg + P\gamma cos\theta - \rho gV + f(v) \qquad (3.1)$$

Where *F(x)* is the force measured when the sample is immersed at depth x, m is the mass of the sample and g is the gravity acceleration. P is the wetted perimeter of the sample, θ is the contact angle at the interface between the test liquid, the sample, and air, ρ is the density of the liquid V is the immersed volume of the sample (i.e., $V = V(x)$). Friction can be neglected due to the low immersion speed. Due to the constant value of mg, $F(x) - mg = F'(x)$. Considering the condition of $x = 0$, the equation can be simplified as:

$$F'(0) = P\gamma cos\theta \tag{3.2}$$

The obtained contact angles were used to calculate the adhesion work (W_{adh}) between the solid-liquid interface [139]. Considering a liquid wetting a solid surface, the work of adhesion is defined as the difference between the surface tensions of the liquid/vapor (γ_{lv}) and solid/vapor (γ_{sv}) and the surface tension of the solid/liquid (γ_{sl}):

$$W_{adh} = \gamma_{lv} + \gamma_{sv} + \gamma_{sl} \tag{3.3}$$

Using Young's equation to express γ_{sv},

$$\gamma_{SV} = \gamma_{SL} + \gamma_{lv}\cos\theta \tag{3.4}$$

The work of adhesion becomes:

$$W_{adh} = \gamma_{lv}(1 + \cos\theta) \tag{3.5}$$

The work of adhesion of each of the three test liquids on the solid was calculated.

The Lewis acid/base multicomponent approach was adopted, which defines the surface energy of a solid as a sum of three components: one dispersive component due to Van der Waals forces (γ^{LW}), one acidic (γ^{+}) and one basic component (γ^{-}). The previously calculated work of adhesion resulted:

$$W_{adh} = 2(\sqrt{\gamma_l^{LW}\gamma_s^{LW}} + \sqrt{\gamma_l^{+}\gamma_s^{-}} + \sqrt{\gamma_l^{-}\gamma_s^{+}}) \tag{3.6}$$

Equation 3.6 was written for each test liquid, and the three equations were used to write a matrix with the three components of the surface free energy of the solid (γ_s^{LW}, γ_s^{+}, γ_s^{-}) as unknown quantities (the components of the liquid surface energy are known) [27], [140]. Finally, the total surface free energy was calculated through Van Oss-Chaudhury-Good Equation [140]:

$$\gamma_s = \gamma_s^{LW} + 2\sqrt{\gamma_s^{-}\gamma_s^{+}} \tag{3.7}$$

The liquids (Sigma Aldrich) used as testing solutions [27] were: Milli-Q Water (acid), Ethylene Glycol (EG, base), and 1-bromonaphtalene (BF, apolar). Moreover, hexadecane was used to measure the diameter of the MFs.

3. Results

3.1. Comparison between the mechanical properties of the MFs

The stress-strain curves obtained with tensile tests on bare and coated MFs are reported in Figure 3.2.

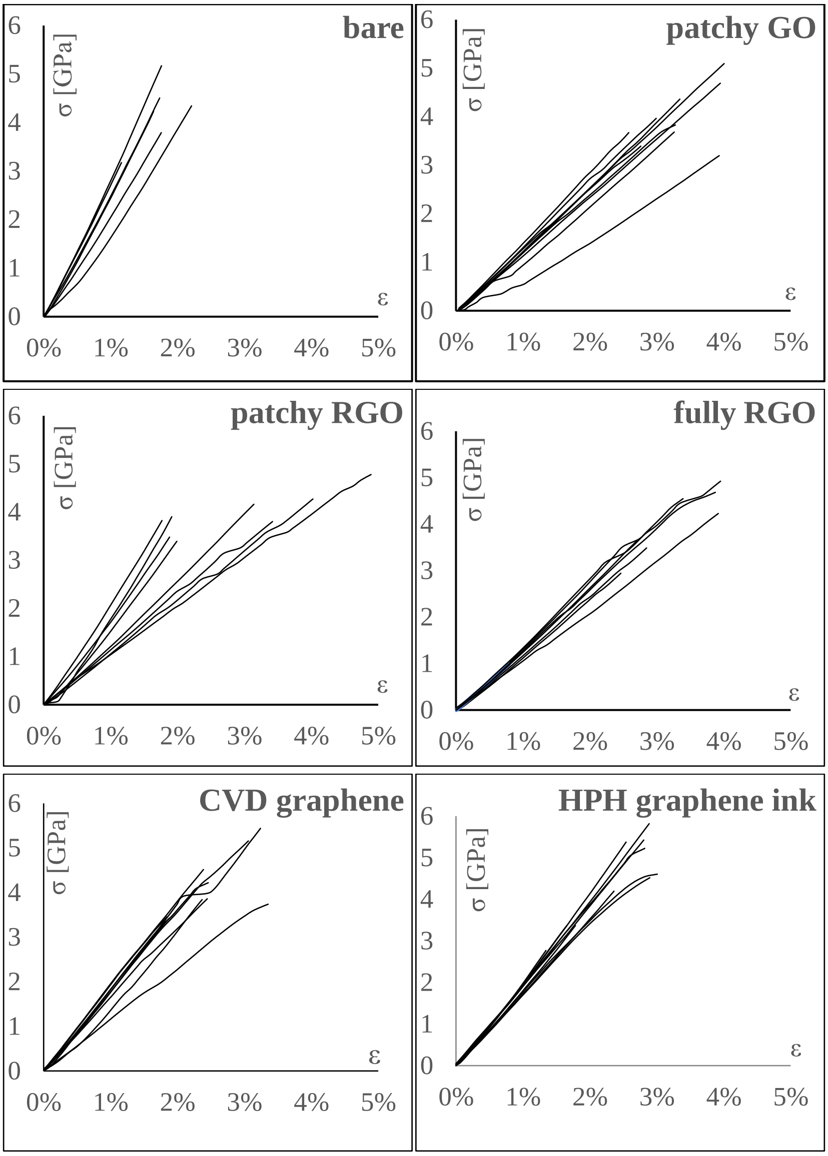

Figure 3.2 Stress (σ)-strain (ε) curves obtained performing tensile tests on bare carbon and GO coated carbon MFs.

Table 3.1 summarises the mechanical properties calculated from the results of the tensile tests. The stiffness decreased when coating the fibres. Even though the strength remained similar, by treating the surface of the MFs with GO, the strain and toughness increased.

Table 3.1 Mechanical properties of the bare and coated MFs.

Fibre	σ_u **[GPa]**	ε_u **[mm/mm]**	E **[GPa]**	T **[J/g]**
PAN carbon	4.203± 0.674	0.017± 0.003	272.478± 33.454	15.351± 4.240
PAN carbon coated with patchy GO	3.959± 0.589	0.033± 0.005	130.402± 14.861	28.660± 8.126
PAN carbon patchy coated with RGO	3.952± 0.448	0.029± 0.012	171.052± 54.632	25.766± 14.603
PAN carbon fully coated with RGO	4.066± 0.725	0.033± 0.006	137.767± 13.834	31.169± 11.811
PAN carbon CVD graphene coated	4.183± 0.722	0.026± 0.005	170.406± 23.802	24.718± 9.109
PAN carbon HPH graphene ink coated	4.655± 0.890	0.025± 0.005	192.350± 11.885	27.212± 9.442

Student t-test was performed to evaluate the difference between coated and bare fibres. The results obtained are presented in Table 3.2.

Table 3.2 p-values obtained performing the Student t-test between the mechanical properties of the bare and coated fibre.

Fibre	σ_u **[GPa]**	ε_u **[mm/mm]**	E **[GPa]**	T **[J/g]**
PAN carbon coated with patchy GO	0.460	0.000	0.000	0.002
PAN carbon patchy coated with RGO	0.418	0.037	0.002	0.119
PAN carbon fully coated with RGO	0.733	0.000	0.000	0.010
PAN carbon CVD graphene coated	0.959	0.005	0.000	0.036
PAN carbon HPH graphene ink coated	0.312	0.004	0.000	0.013

3.2. Surface free energy computation of the GO coated fibres

Given the data obtained with tensile tests and the Student t-test, the MFs coated with patchy GO were the most different from the bare fibres. Thus, the differences in the surface of bare and patchy GO coated MFs were experimentally investigated.

Figure 3.3 reports two measurements of the dynamic advancing and receding contact angles in water of bare and GO coated MFs.

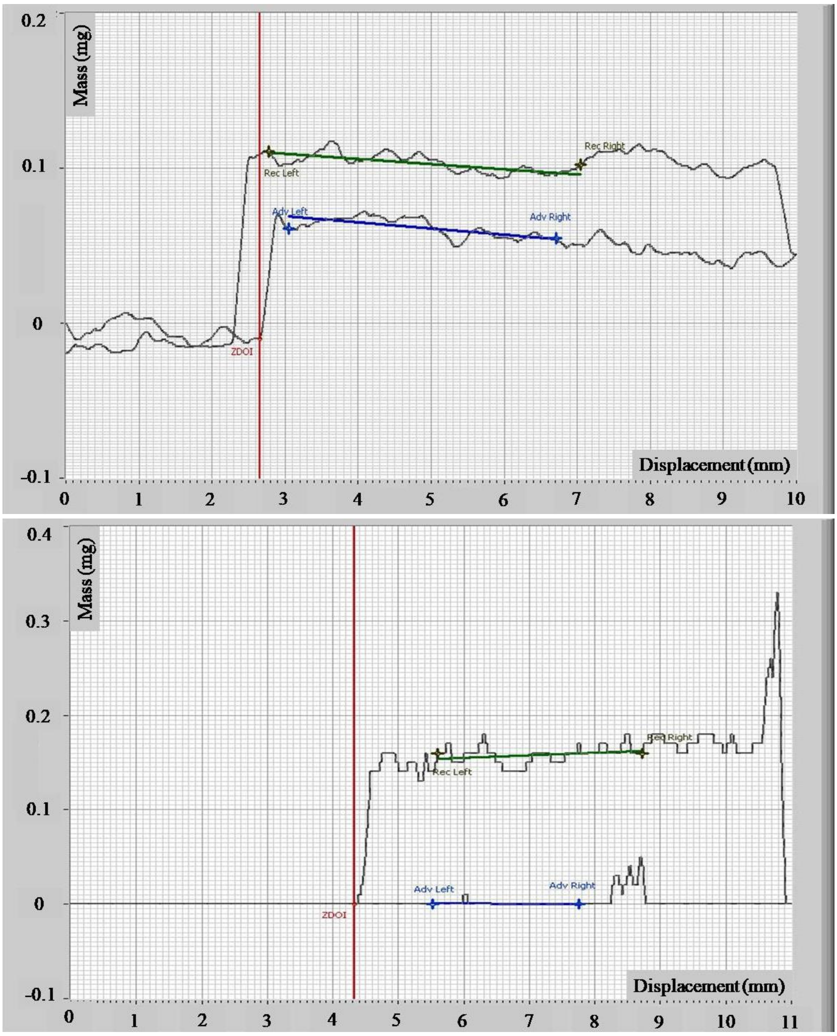

Figure 3.3 Measurement of the advancing and receding contact angle in water, of a bare (top) and GO coated (bottom) carbon fibre.

An increase of hysteresis in the measurement of the contact angles was recorded with coated MFs, when immersed in water and EG (polar)

(Figure 3.3). The hysteresis phenomenon decreased instead in BF (apolar).

Table 3.3 and Table 3.4 show the advancing and receding contact angles calculated with the Wilhelmy method on bare and coated MFs respectively. Hexadecane has been used exclusively for the direct determination of the wetted perimeter, estimating the fibre diameter 7.1 ± 0.2 μm.

Table 3.3 Advancing and receding contact angles of bare carbon MFs obtained with the Wilhelmy method.

	Advancing contact angle [°]	**Receding contact angle [°]**
Milli-Q water	69±7	46±6
Ethylene glycol	57±9	35±5
1-bromonaphtalene	38±3	9±15

Table 3.4 Advancing and receding contact angles of GO coated carbon MFs obtained with the Wilhelmy method.

	Advancing contact angle [°]	**Receding contact angle [°]**
Milli-Q water	88±5	19±13
Ethylene glycol	74±17	32±19
1-bromonaphtalene	32±23	31±23

Advancing and receding contact angles were used to calculate the advancing and receding MFs' acid-base surface free energy components [27]. Total surface free energy was calculated through Van Oss-Chaudhury-Good Equation [140] and the obtained results are presented in Table 3.5 and Table 3.6. As commonly considered, the advancing angle characterizes the lowest energy areas, while receding angles characterize the highest energy zone.

Table 3.5 Advancing (ADV) and receding (REC) surface energy components of bare carbon MFs.

	ADV [x 10^{-3} J/m^2]	**REC [x 10^{-3} J/m^2]**
LW Component (γ_S^{LW})	35±0	43±1
Basic Component (γ_S^-)	17±3	33±1
Acid Component (γ_S^+)	0±1	0±1
Total Surface Energy (γ_S)	36±4	46±3

Table 3.6 Advancing (ADV) and receding (REC) surface energy components of GO coated carbon MFs.

	ADV **[x 10^{-3} J/m^2]**	**REC** **[x 10^{-3} J/m^2]**
LW Component (γ_S^{LW})	38±2	38±1
Basic Component (γ_S^{-})	7±3	70±2
Acid Component (γ_S^{+})	1±3	0±2
Total Surface Energy (γ_S)	38±8	38±37

The surface energy of the bare MFs was thus between 36 and 43 mJ/m2. Moreover, results showed a significant basic component and a negligible acidic component of fibre surface energy in terms of the acid-base theory of surfaces, based on a generalized Lewis acid-base definition. Considering the coated fibres, significant variations in the measurements were recorded. Again, a significant basic component was found. As an effect of the difficult experimental conditions, the square roots of some of the surface energy components resulted negative.

4. Conclusions

Student t-test showed a statistical difference ($p<0.05$) between the strain of the coated fibres compared to the bare ones. An overall significant decrease of stiffness was recorded when coating the carbon MFs ($p<0.001$). The toughness of the coated fibres resulted significantly higher ($p<0.05$) than the bare MFs, except for the patchy coated RGO fibres. Thus, the results obtained employing tensile tests showed changes in the bulk properties after coating.

The experimental evaluation of fibre surface is useful to define the composition of the solution that better wets fibres and to prepare the solvent in which to dissolve possible fibre-coating components.

Given the calculated surface free energy, a complete wettability of the fibres could be achieved using solutions with surface energy below 36 mJ/m_2 for the bare MFs and below 38 mJ/m^2 for the coated ones. The high variation of the results was due to the very small size and high compliancy of the samples.

Since both bare and coated fibres have a strong basic component and a null acid one, these results could represent both purely dispersive or dipolar interactions (e.g.: Van Der Waals Forces), or basic interactions.

Thus, acidic proteins or other acid components could be used to functionalise the surface of the fibres, obtaining strong interactions.

Experimental results showed that bare and coated fibres have similar surface properties, but the coated ones present a higher hysteresis. In particular, polar liquids seem to enhance the hysteresis, while non-polar ones have zero hysteresis. Since increasing heterogeneity and irregularities of the surface increases hysteresis, a possible cause could be that the immersions modify the GO layer, depending on the used solvent. Moreover, the coated fibres showed significant variations probably due to the polar liquid-GO interactions.

Wetting measurements revealed thus the stability of the coating during prolonged contact with non-polar liquids. Considering the specific application of the tested fibres, these results showed that a hydrophilic tissue could attack the coating. However, since the extracellular matrix of the spinal cord tissue is mostly composed of collagen, which is a hydrophobic matrix due to the high presence of proline, the implanted coated fibres maintain their stability and thus their efficiency and efficacy.

It is important to underline that the here described measurements were performed even if the samples had a very low thickness, thanks to their high rigidity and/or their significant hydrophobicity. However, due to experimental limitations (e.g., micrometric dimensions of the fibres, low density, high curvature), the obtained preliminary results presented high variability.

Work performed in collaboration with prof. Andrea Ferrari (Cambridge Graphene Centre, University of Cambridge, 9 JJ Thomson Avenue, Cambridge CB3 0FA, UK) and the group of the Cambridge Graphene Center, who produced the different graphene-coated fibres and discussed the results; prof. Claudio Della Volpe (Department of Civil, Environmental and Mechanical Engineering, University of Trento, Via Mesiano 77, 38123 Trento, Italy) who guided the experimental and theoretical calculation of the surface energy, and revised the work; prof. Stefano Siboni (Department of Civil, Environmental and Mechanical Engineering, University of Trento, Via Mesiano 77, 38123 Trento, Italy) who helped in the theoretical calculation of surface energy.

Chapter 4 Tensile tests on prototypes of the final intraspinal microstimulation device

1. Introduction

The intraspinal microstimulation device designed by Neurofibres is composed of interconnected MFs. Two types of prototypes were produced by Axon' Cable SAS:

- Type 1: 30 or 10 *x*-directed electrodes and 3 *y*-directed wires (Figure 4.1, left)
- Type 2: 20 *x*-directed electrodes and 3 *y*-directed wires (Figure 4.1, right).

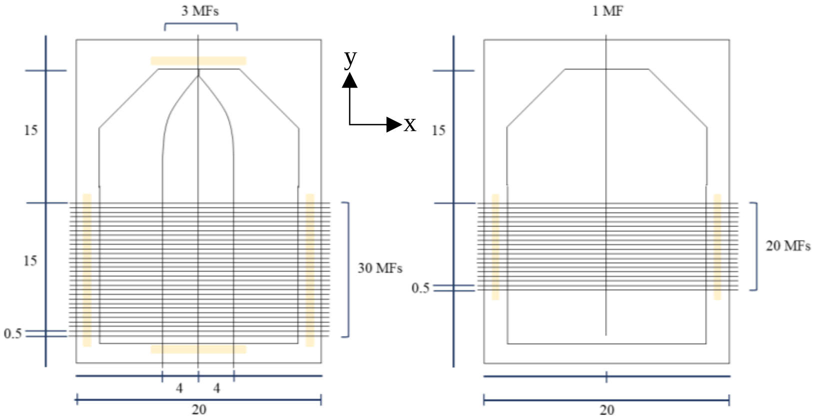

Figure 4.1 On the left, prototype type 1 with 30 x-MFs; on the right prototype type 2.

Type 2 is an optimisation of type 1. As explained in Chapter 1, the *y*-wires have two functions: transferring the electrical stimuli from the external generator and connecting the electrodes among each other. The *x*-MFs are the electrodes stimulating the neural networks. Prototypes with different combinations of MFs (cobalt-based alloy, stainless steel, carbon), microwires (cobalt-based alloy, stainless steel), and different interconnections (electric welding, UV glue, medical grade UV glue, medical grade conductive glue, chemical machining, silver-filled epoxy glue) were produced.

Tensile tests were performed to evaluate the mechanical characteristics of the prototypes. The maximum force recorded during the test was used to calculate the adhesion energy of the different types of interconnections.

2. Materials ad methods

2.1. Samples

Table 4.1 summarises the provided samples.

Table 4.1 Samples provided by Axon' Cable SAS and tested with the tensile tests.

Type 1			**Type 2**		
Microfibres (number, diameter)	*Microwires (number, diameter)*	*Joints*	*Microfibres (number, diameter)*	*Microwires (number, diameter)*	*Joints*
Cobalt-based alloy (10, 12.7 μm)	Cobalt-based alloy (3, 12.7 μm)	Electric welding	PAN carbon (20, 7 μm)	Cobalt-based alloy (1, 12.7 μm)	Silver-filled epoxy glue
Stainless steel (30, 12.7 μm)	Stainless steel (3, 12.7 μm)	Electric welding	PAN carbon (20, 7 μm)	Stainless steel (1, 12.7 μm)	Silver-filled epoxy glue
Cobalt-based alloy (30, 12.7 μm)	Cobalt-based alloy (3, 12.7 μm)	UV glue			
Stainless steel (30, 12.7 μm)	Stainless steel (3, 12.7 μm)	UV glue			
Stainless steel (30, 12.7 μm)	Stainless steel (3, 12.7 μm)	Medical grade UV glue			
Stainless steel (30, 12.7 μm)	Stainless steel (3, 12.7 μm)	Medical grade conductive glue			
Stainless steel (30, 12.7 μm)	Stainless steel (3, 12.7 μm)	Chemical machining			

Except for the specimen produced from the stainless steel film, type 1 prototypes came in a plastic sample holder. Type 1 prototypes were fixed on a metallic sample holder. One sample of each listed prototype in Table 4.1 was provided and thus tested.

2.2. Tensile tests

Tensile tests were performed by pulling the 3 (type 1) or 1 (type 2) microwires, to evaluate the adhesion energy of the interconnections.
The prototypes type 1 were tested with an Agilent T150 UTM nanotensile machine, except for the chemical machined sample, which was tested with Messphysik MIDI 10-20 Tensile Machine (Mettler Toledo cell load of 2 Kg). The plastic sample holder was cut with the blade of a cutter, previously heated with a heat gun. This precaution was taken to avoid the recoil on the sample due to scissor cutting, which was potentially harmful to the joints. The cut part was then covered with paper tape, which helped to mount the sample in the nanotensile machine and was removed before starting the test. To test the type 2 prototypes, the *y*-directed wire was detached from the sample holder and attached to paper support to increase the friction with the grip of the tensile machine. The top part of the metallic sample holder frame was bent to avoid friction with the microwire during tensile tests. Force-displacement curves were obtained imposing a testing speed of 0.1%-gauge length/second. The failure of the system was considered when the tensile load was zero, thus when all the junctions or the *y*-fibres broke.

3. Results

3.1. Cobalt-based (35N LT) alloy microfibres connected with electric welding

The joints between *x*-MFs and *y*-wires were performed by electric welding. Unfortunately, the sample was partially damaged upon manipulation: one *y*-MF was detached from all ten *x*-MFs and one *x*-MF was broken. Moreover, when the plastic sample holder was cut and during and the mounting procedure, 7 *x*-MFs broke. The breakage of the interconnections was reported during the tensile test (Figure 4.2).

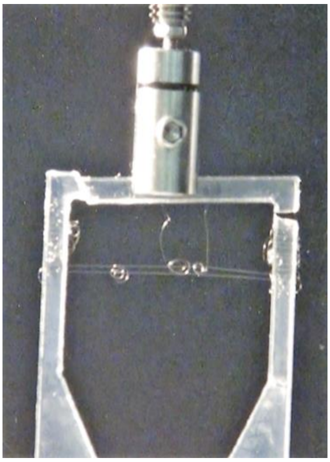

Figure 4.2 Cobalt-based alloy MFs interconnected using electric welding before the tensile test.

The resulting force-displacement plot is showed in Figure 4.3.

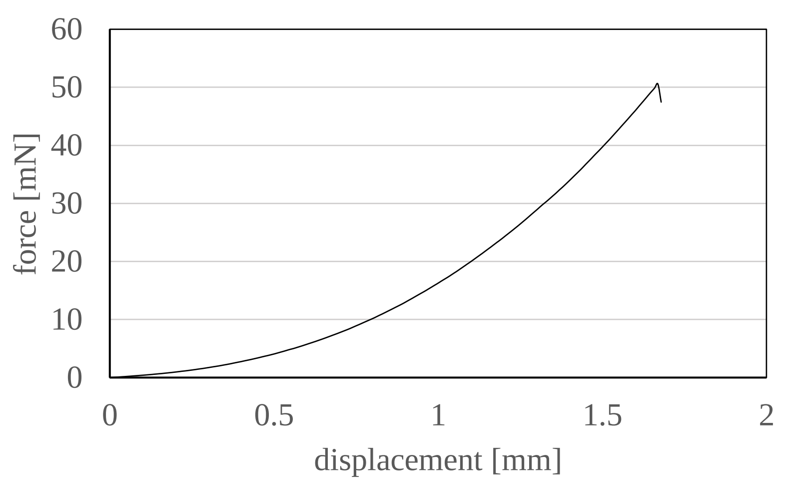

Figure 4.3 Force-displacement curve of cobalt-based alloy MFs interconnected using electric welding.

3.2. Stainless steel microfibres connected with electric welding

The first *y*-fibre from the right was broken upon manipulation. When the remaining two *y*-MFs were released from the rigid support, another *y*-MF and many joints broke (Figure 4.4). However, the sample appeared in better conditions than the welded cobalt-based alloy MFs. The force-displacement plot resulting from the tensile test is reported in Figure 4.5.

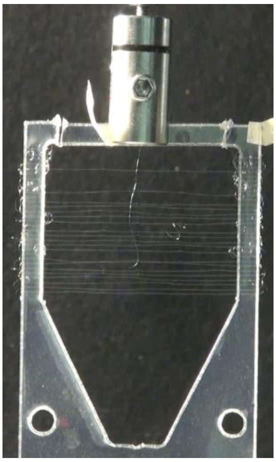

Figure 4.4 Stainless steel MFs interconnected using electric welding before the tensile test.

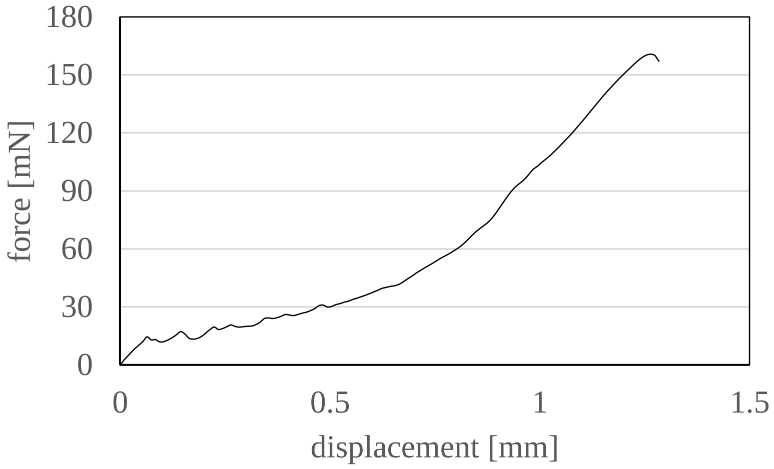

Figure 4.5 Force-displacement curve of stainless steel MFs interconnected using electric welding.

3.3. Cobalt-based (35N LT) alloy microfibres connected with UV glue

The sample was not intact before testing (Figure 4.6). The breakage of one *y*-MF occurred first, and then the pullout of two *y*-MFs from the joints.

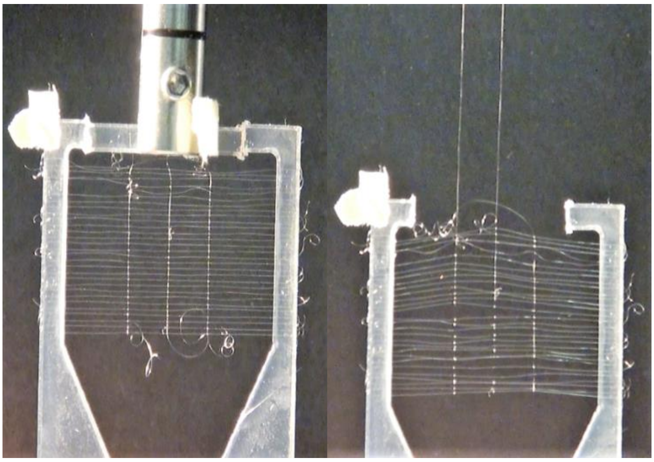

Figure 4.6 Cobalt-based alloy MFs interconnected with UV glue before (left) and during (right) the tensile test.

Figure 4.7 reports the force-displacement plot of the test.

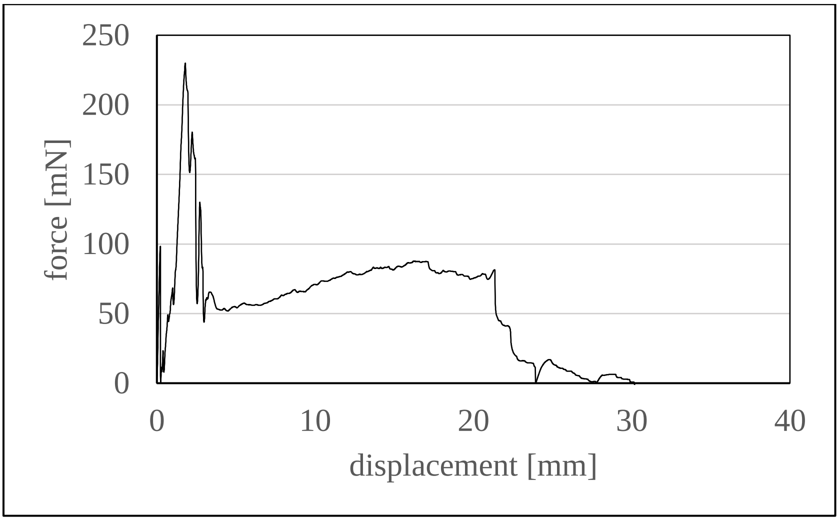

Figure 4.7 Force-displacement curve of cobalt-based alloy MFs connected with UV glue.

3.4. Stainless steel microfibres connected with UV glue

During the pre-test procedure, damages were observed in the sample. The three *y*-MFs and 26 *x*-MFs were initially intact (Figure 4.8).

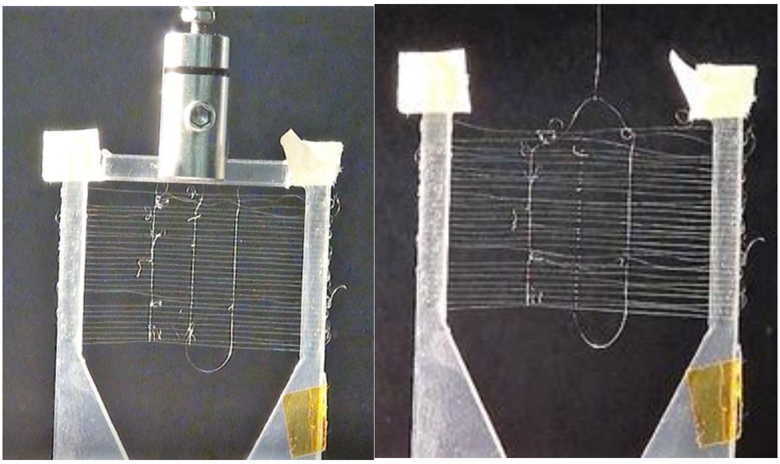

Figure 4.8 Stainless steel MFs interconnected with UV glue before (left) and after (right) the tensile test. Stainless steel MFs interconnected with UV glue before (left) and after (right) the tensile test.

When the test started, few events were observed. First, the breakage of two *y*-MFs and then of one *x*-MF that remained fixed in the upper grip. The rupture of the last *y*-MF caused the final breakage and the end of the tensile test. The force-displacement plot is reported in Figure 4.9.

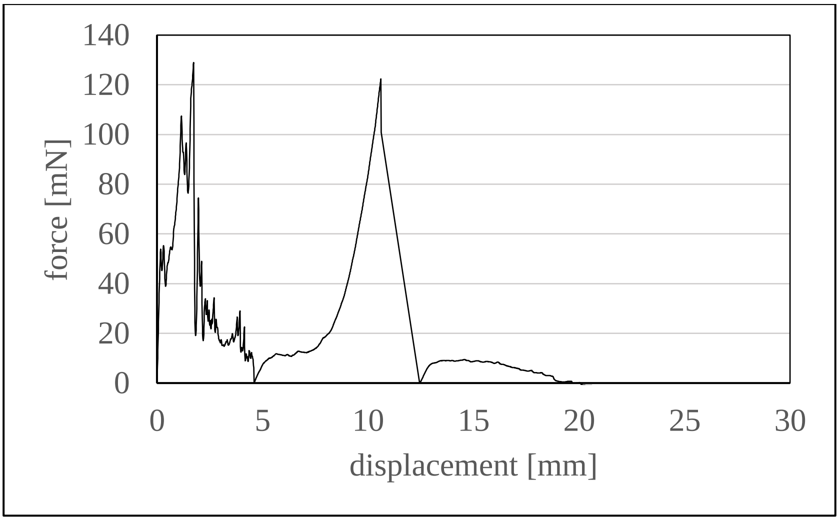

Figure 4.9 Force-displacement curve of stainless steel MFs interconnected UV glue.

3.5. Stainless steel microfibres connected with medical grade UV glue

The MFs of this sample were connected through a medical grade UV glue. The sample was intact at the beginning of the tensile test (Figure 4.10, left).

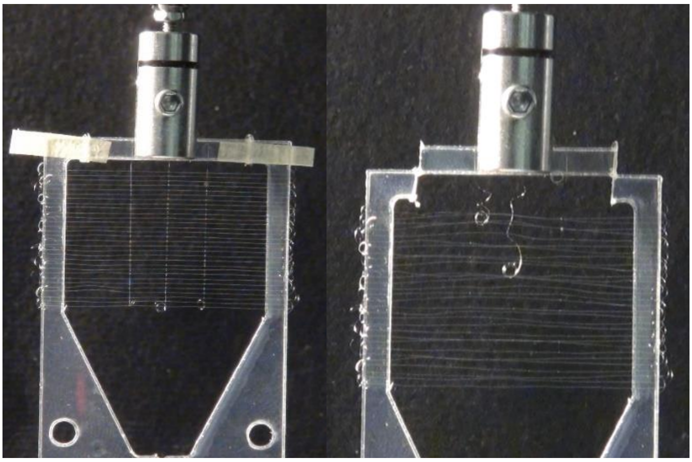

Figure 4.10 Stainless steel MFs interconnected with medical grade UV glue before (left) and after (right) the tensile test.

A few of the joints in the lower part of the sample broke first, and then a few in the middle. Subsequently, the *y*-MF on the right broke and then several joints (Figure 4.10, right).

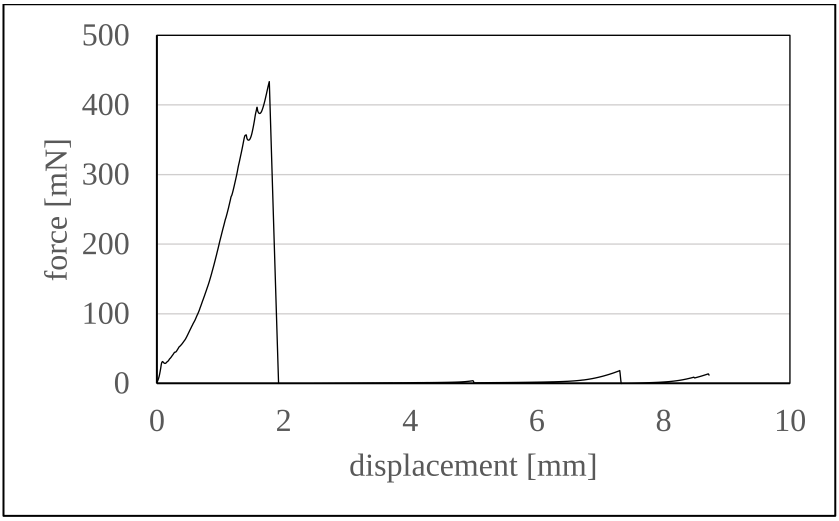

Figure 4.11 Force-displacement curve of stainless steel MFs connected with medical grade UV glue.

The force reached high values in the first part of the test when most of the joints and one *y*-fibre broke (Figure 4.11).

3.6. Stainless steel microfibres connected with medical grade conductive glue

The *x*-MF in the middle broke while the specimen was being prepared for the test (Figure 4.12). During the test, all the joints broke randomly. A slip-out of the *y*-MFs from the joints starting from the lower part of the sample was also recorded. Figure 4.13 reports the force-displacement curve.

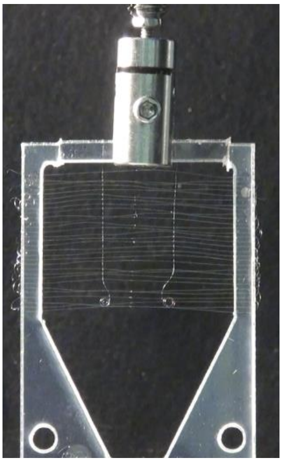

Figure 4.12 Stainless steel MFs interconnected with medical grade conductive glue before the tensile test.

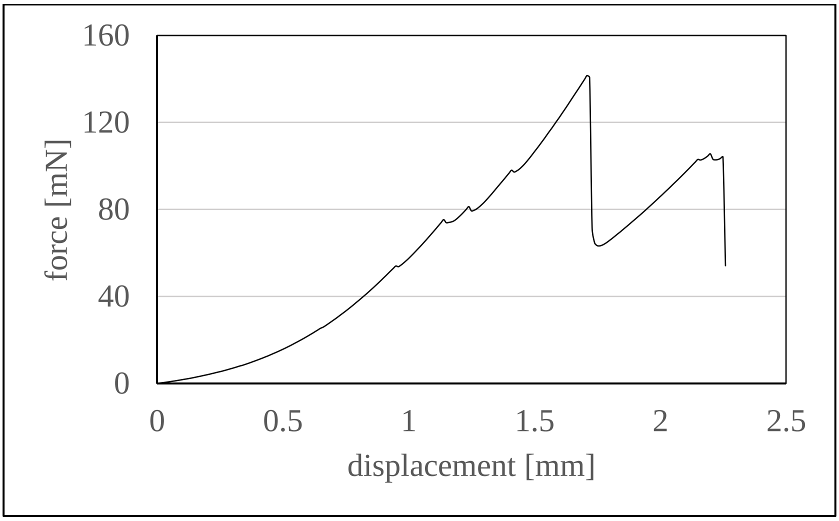

Figure 4.13 Force-displacement curve of stainless steel MFs connected with medical grade conductive glue.

3.7. Chemical machining

A stainless steel plate (thickness = 10 µm) underwent chemical machining to obtain an array of MFs with a resulting rectangular section (width = 25 µm, thickness = 10 µm). The obtained specimen had the configuration of type 1 prototypes: 3 y and 30 *x*-MFs, but with a rectangular cross-section (Figure 4.14). Due to the higher load recorded, Messphysik MIDI 10-20 Tensile Machine was used to characterise this sample. The *y*-MF on the right broke first. Few of the *x*-MFs detached from the sample holder on the left side, while on the right side all MFs remained intact. The *y*-MFs were deformed and broke at the level of the sample holder.

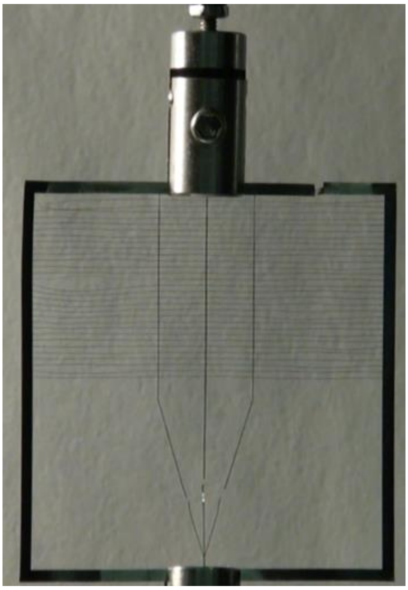

Figure 4.14 MFs-like sample obtained from the chemical machining of a stainless steel plate with a thickness of 10 µm before the tensile test.

The force recorded reached the highest values of the tested type 1 samples (Figure 4.15).

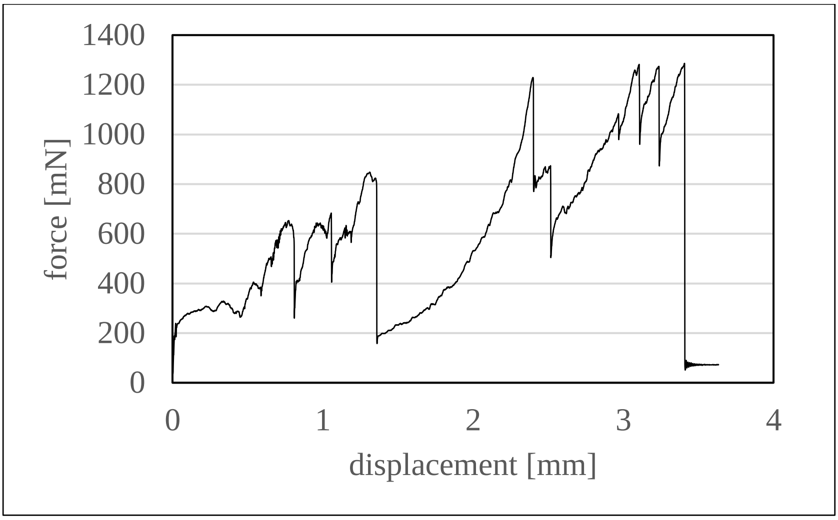

Figure 4.15 Force-displacement curve of the MFs-like sample obtained from the chemical machining of a stainless steel plate.

3.8. Carbon MFs connected to a stainless steel microwire with silver-filled epoxy glue

The sample was composed of 20 MFs interconnected through silver-filled epoxy glue with a stainless steel microwire (Figure 4.16).

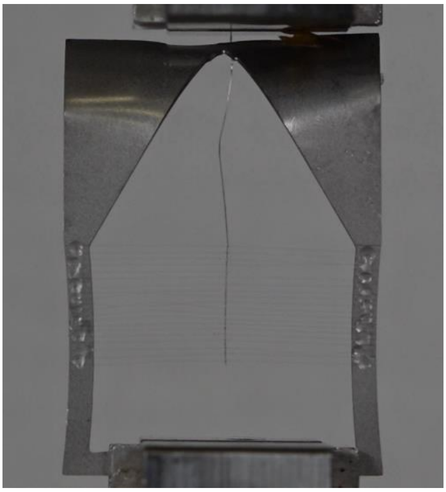

Figure 4.16 Prototype composed of carbon MFs and the stainless steel microwire, mounted in the tensile machine.

The obtained force-displacement curve is reported in Figure 4.17. The first breakages were recorded in the middle-right part of the sample (force peak), between the MFs and the frame. Then, the breakage occurred at the joints between the MFs and the microwire (i.e., at the joints).

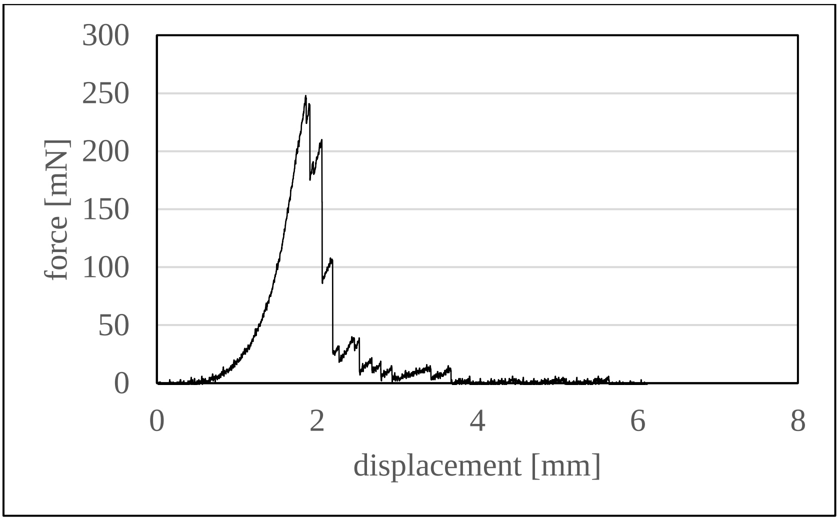

Figure 4.17 Force-displacement curve of carbon MFs connected with a stainless steel wire through silver epoxy glue.

3.9. Carbon MFs connected to a cobalt microwire with silver-filled epoxy glue

The junctions of these samples did not break under tensile load. Indeed, the prototype failed because the microwire broke (Figure 4.18).

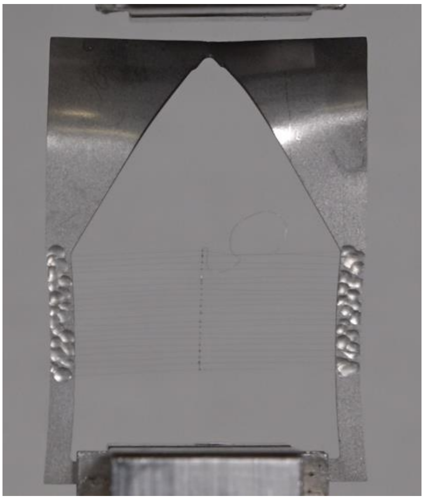

Figure 4.18 The sample composed of carbon MFs interconnected to the cobalt microwire through silver-filled epoxy glue after tensile test.

Figure 4.19 shows the force and displacement reached during tensile test.

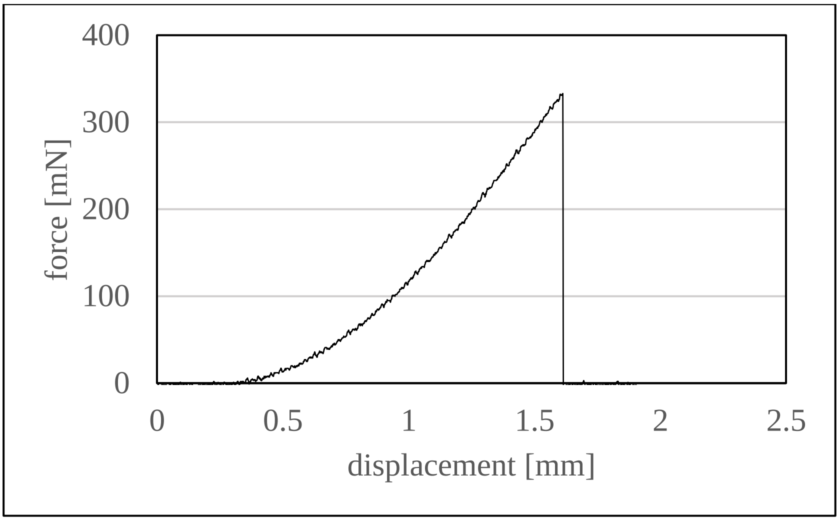

Figure 4.19 Force-displacement curve of carbon MFs connected with a cobalt alloy wire through silver epoxy glue.

3.10. The adhesion energy of the interconnections

The adhesion energy (G) was calculated as following [135]:

$$F = 2\pi R\sqrt{ERG} \tag{4.1}$$

Where F is the maximum force recorded during tensile tests, R is the radius of the MF, and E is the Young's modulus of the fibre. To obtain the adhesion energy of a single joint (G_n) the force F_j was considered:

$$F_j = \frac{F}{number\ of\ y\ fibres} \tag{4.2}$$

The adhesion energy was then calculated with equation 1 and then normalised for the number of intact joints (i.e., number of x-fibres) before the tensile test. Table 4.2 summarises the features of the different samples.

Table 4.2 Features of the different tested systems. The type of MFs, microwires, and joints used are specified. # y-MFs nominal and real are the number of y-MFs (microwires) right after production and right before being tested under tensile load, respectively. # x-MFs nominal and real are the number of x-MFs right after production *and right before being tested under tensile load, respectively. The overall adhesion energy was estimated for each type of sample (G) and the single joints (G_n).*

Microfibre (Microwire)	**Joint**	**# y-MFs nominal**	**# y-MFs real**	**# x-MFs nominal**	**# x-MFs real**	**G_n [N/m]**	**G [N/m]**
Cobalt-based alloy (Cobalt-based alloy)	Electric welding	3	1	10	2	0.64	1.28
Stainless steel (Stainless steel)	Electric welding	3	1	30	21	0.69	14.43
Cobalt-based alloy (Cobalt-based alloy)	UV glue	3	3	30	29	0.10	26.43
Stainless steel (Stainless steel)	UV glue	3	3	30	26	0.04	9.29
Stainless steel (Stainless steel)	Medical grade UV glue	3	3	30	30	0.39	104.94
Stainless steel (Stainless steel)	Medical grade conductive glue	3	2	30	30	0.09	11.20
Stainless steel (Stainless steel)	Chemical machining	3	3	30	30	1.23	333.21
Carbon (Stainless steel)	Silver-filled epoxy glue	1	1	20	20	1.64	32.86
Carbon (Cobalt-based alloy)	Silver-filled epoxy glue	1	1	20	20	2.77	55.44

One sample for each of the 9 types of prototypes was tested. Though an e*x*-post statistical treatment of data was not possible, due to the limited number of different samples, an estimation of possible sources of uncertainty was performed and by propagating them, overall uncertainties were calculated. Except for the sample obtained by chemical machining of a stainless steel plate, the estimated errors are one or two orders of magnitude smaller than the calculated values of G and G_n (between 2 and 4 % circa). Thus, according to this assessment, the data obtained by tensile testing the prototypes can be considered reliable. Table 4.3 summarises all the obtained results.

Table 4.3 G is the adhesion energy of the prototype; Gn is the adhesion energy of a single joint. dGn and dG are the errors calculated with the error propagation method.

Microfibre	Microwire	Joint	G_n [N/m]	dG_n [N/m]	G [N/m]	dG [N/m]
Cobalt-based alloy	Cobalt-based alloy	Electric welding	0.159	0.004	1.28	0.03
Stainless steel	Stainless steel	Electric welding	0.686	0.016	14.43	0.34
Cobalt-based alloy	Cobalt-based alloy	UV glue	0.101	0.002	26.43	0.58
Stainless steel	Stainless steel	UV glue	0.040	0.001	9.29	0.22
Stainless steel	Stainless steel	Medical grade UV glue	0.388	0.009	104.94	2.45
Stainless steel	Stainless steel	Medical grade cond. glue	0.093	0.002	11.20	0.26
Stainless steel	Stainless steel	Chemical machining	1.232	0.255	333.21	68.91
Carbon	Stainless steel	Silver-filled epoxy glue	1.643	0.072	32.86	0.80
Carbon	Cobalt-based alloy	Silver-filled epoxy glue	2.772	0.110	55.44	1.19

4. Conclusions

The results obtained with the two types of prototypes are commented separately.

Type 1. Considering the two specimens formed by welded MFs, the stainless steel sample resulted in higher adhesion energy than the cobalt MFs based prototype. It must be although considered that the latter was the first sample tested and it underwent significant stimuli. However, the prototype made of cobalt alloy MFs reached higher adhesion energy if compared to structures made of stainless steel MFs connected with the same glue. Electric welding and medical grade UV glue resulted in the best joint methods.

The stainless-steel sheet cut by electric welding showed the most resistant joints. However, this specimen was not characterised by interconnected MFs and should not be compared with the other samples.

The main failure cause of the welded and glued MF array was the pullout of the *y*-wire from the joint. The sample obtained from a stainless steel plate showed a different behaviour during the tensile tests, probably due to its different structure. Indeed, the final failure was caused by the breakage of the *y*-MFs.

Type 2. The breakage of junctions or other components was not recorded before testing and while mounting the samples in the tensile machine. The system composed of carbon MFs and stainless steel microwire broke at the junctions between the *x*-MFs (carbon) and the metallic frame. The tensile test on the system made of carbo MFs and cobalt wire caused the breakage of the cobalt wire instead. The maximum forces recorded with tensile tests on single stainless steel MFs and cobalt based alloy MFs are 293.78±11.48 and 345.56±39.17 mN, respectively. Thus, the x and *y*-fibres interconnections have maximum forces comparable to the single MFs.

Overall, the tested type 1 prototypes showed considerable rigidity and fragility, many were indeed damaged in the shipping and handling phases. Thus, the multiple MFs joints are potential breaking points leading to device failure and eas*y*-to-handle protection is needed with this design. Type 2 prototypes were easy to handle instead. The breakage of junctions or other components was not recorded before testing and while mounting the samples in the tensile machine. In conclusion, type 2 is more resistant to tensile load and easier to handle than type 1. It is thus possible to assert that the optimisation performed to produce type 2 prototypes is favourable. Indeed, the interconnections are stable and are as resistant as the material of the MFs composing the system. However, in most cases, maximum tensile loads were below 1 N, indicating that extreme care is needed during handling before and during implantation.

Chapter 5 The mechanical interplay of an intraspinal stimulation device and the spinal cord: an analysis of the possible causes of failure

1. Introduction

The ISMS device designed and developed by Neurofibres is grafted in the injured area of the spinal cord tissue. The spinal cord is contained in the vertebrae of the spine, which bends in specific ranges of movement employing the muscles. The vertebrae are connected to the spinal cord tissue with three membranes (the meninges), and the bending movements of the spine are thus transmitted to the nervous tissue. Thus, once described the device and its components, the mechanical interplay between the device and the host tissue (i.e., spinal cord) was studied. This chapter aims to investigate the interplay in terms of possible failure mechanisms of the device, caused by the interactions with the nervous tissue. Three failure mechanisms were considered: the breakage of the device due to the strains of surrounding host tissue, the migration and consequent dislocation of the electrodes caused by small movements of the spine, and the loss of adhesion between the device and the embedding matrix due to the pullout of the device.

Experimental tests on human cadavers were performed to investigate the dimensions of the strains imposed on the spinal cord during the physiological bending of the cervical and thoracic area [28], [45]. These studies showed that the cervical and thoracic tracts of the spinal cord undergo strains between 2 and 10 %. Data collected in the literature showed higher strains in the cervical tract of the spine and lower deformations in the thoracic one. Given these data, a study on the feasibility of implanting the prototypes tested in Chapter 3 was performed. Devices for the treatment of SCI are usually studied in vivo in the cervical and thoracic tracts of the spine [46], thus the study was limited to these segments of the spine.

The efficacy and efficiency of ISMS devices are based on the stimulation and activation of specific neural networks, reached by the electrodes. Consequently, once implanted the electrodes must stay fixed to the specific area. The second failure mechanism considered was thus the migration of the implanted electrodes due to the small movement of the spinal cord. To study this phenomenon, an ad hoc experimental setup was designed and developed. The setup aimed to simulate the small physiological movements of the spinal cord, such as bending, heart beating, or the cellular process associated with tissue healing. To simulate the embedding matrix, a solution of edible gelatin with rheological properties comparable to the injured spinal cord was used. The migration of carbon MFs was evaluated in terms of displacement and escape velocity.

External connections to an electric stimulator are needed to transmit the impulse to the electrodes and the neural networks [16]. The set of MFs electrodes is positioned parallel to the longitudinal axis of the spine, and the microwires perpendicular to these MFs connect the electrodes to an external wire, which in turn is connected to the impulse generator. The external wire and consequently the microwires connected to the electrodes could be subjected to tensile forces. This study aimed to evaluate the adhesion of the system to the embedding matrix when a possibly dangerous condition of pullout occurs. An experimental setup was designed to perform a pullout test with the nanotensile machine and measuring the forces with high precision. The forces needed to pullout single carbon fibres and simplified prototypes from a solution of edible gelatin (mimicking the injured spinal cord) were measured.

2. Materials and methods

2.1. Failure of the embedded electronic system

2.1.1. Samples

As described in Chapter 3, nine different samples provided by Axon' Cable SAS were tested: 35NLT cobalt alloy MFs (diameter 12.7 μm) connected with electric welding and UV glue; stainless steel MFs (diameter 12.7 μm) connected with electric welding, UV glue, medical-grade UV glue, medical-grade conductive glue; stainless steel film (thickness 10 μm) cut with chemical machining, carbon MFs (diameter 7 μm) connected to a stainless steel wire (diameter 12.7 μm) with silver-filled epoxy glue, and carbon MFs (diameter 7 μm) connected to a cobalt alloy wire (diameter 12.7 μm) with silver-filled epoxy glue. One specimen for each type of structure was tested.

2.1.2. Tensile tests on the prototypes

Tensile tests were performed to obtain the mechanical characterisation of the prototypes (Chapter 3). Agilent T150 UTM nanotensile machine and Messphysik MIDI 10-20 Tensile Machine were used; the testing speed was 0.1%-gauge length/second. Given the force and the displacement recorded, the failure strain (ε_f) was calculated considering the displacement corresponding to the complete failure of the system (i.e. the breakage of all the interconnections or the *y*-wires) as the final length (l_f):

$$\varepsilon_f = \frac{l_f - l_i}{l_i} \tag{5.1}$$

Where l_i is the gauge length (Chapter 4).

2.2. Migration of the electrodes

2.2.1. Samples

Bare carbon MFs were chosen to investigate migration phenomena of the electrodes after their implantation in the injured spinal cord. The analysed samples have a diameter of 7 µm and a length of 10 mm.

2.2.2. Experimental set-up

An ad hoc experimental setup was designed and developed to mimic the embedded electrodes system and the physiological bending movement of the spinal cord [28], [45] (Figure 5.1).

Figure 5.1 Final set-up of the experiments. The silicon chamber containing the fibre embedded in gelatin was placed under the object lens of the microscope. As highlighted

by the zoom in the top left corner, the left short side of the chamber was fixed to the stage of the microscope and the right side of the chamber was securely connected to the axle of the shaker.

The migration was observed with an optical microscope (Olympus BX61). A silicon chamber filled with a spinal cord-like matrix was used to reproduce the embedding injured spinal cord.

The milling machine was used to produce a polymethyl methacrylate (PMMA) mould of the chamber (Figure 5.2), that was filled with silicone made of a 1:1 mix of base and catalyst (Poolkemie Silimold AKP-08). The silicone polymerised overnight, and the chambers (length 30mm, height 10 mm, thickness 3 mm) were removed from the PMMA mould.

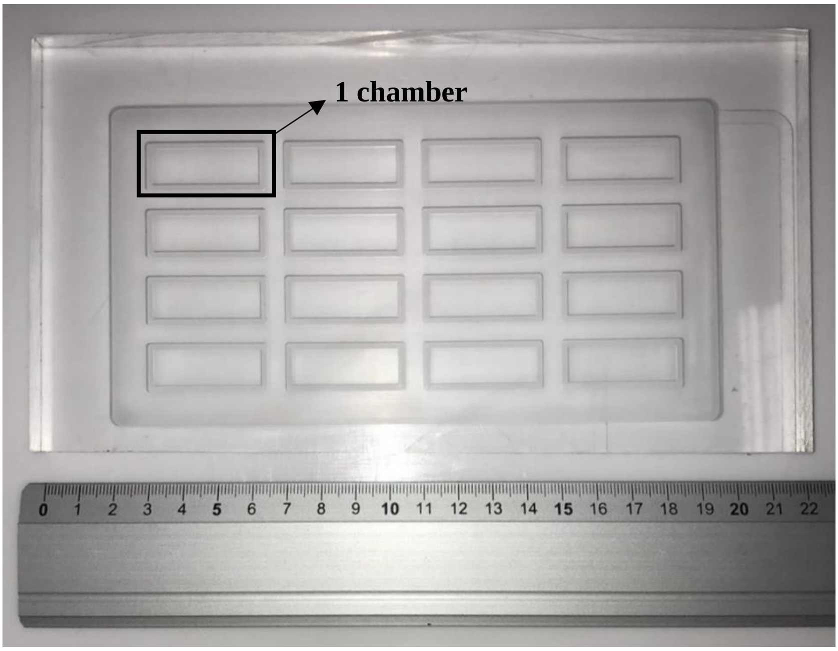

Figure 5.2 Polymethyl methacrylate (PMMA) mould used to produce 16 chambers.

The acute phase generated by SCI is characterised by hemorrhage, inflammation, and fluid build-up [143], which lead to a liquid environment, mostly composed of plasma. This liquid environment represents the worst scenario in terms of MFs migration and was replicated in the experiments. Rheological measurements were performed to define an edible gelatin-water solution that better reproduces the environment after SCI. A cone-plate rheometer (Discovery HR-2 – TA Instruments) was used, imposing 900 s-1 shear rate, at 37° C, for 30 minutes [144]. Edible gelatin was thus chosen as a transparent matrix (to check the movements of the MF with the microscope) with rheological properties similar to the spinal cord tissue after injury. The gelatin solution was poured into the silicone chamber immediately after being prepared and the carbon fibre was placed inside the filled chamber (Figure 5.3).

The setup was designed to simulate the bending movements of the spine. This movement was imposed by a shaker (TIRA GmbH) (Figure 5.1). The silicone chamber containing the MF was placed on the stage of the microscope and two PMMA casing structures were tightened on the two short sides of the chamber. One casing structure was useful to fix one side of the chamber to the stage of the microscope with double-sided tape, the other presented a tapped hole in which the axle of the shaker was screwed (Figure 5.3).

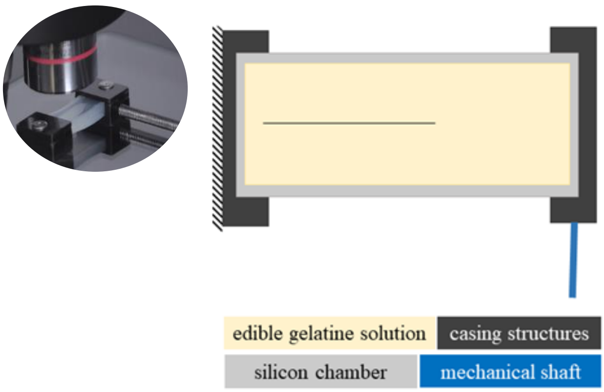

Figure 5.3 Scheme of the part of the setup in which the fibre is embedded in the gelatin matrix contained in the silicon chamber, which is fixed to the microscope stage on one side and on the other to the axle of the shaker thanks to two casing structures.

2.2.3. Migration tests

The shaker imposed a sinusoidal movement in the *x*-y plane, simulating the bending of the spinal cord during physiological movements of the body. The amplitudes of 5, 6, and 8 mm imposed by the shaker caused strains to the chamber between 1 and 2%, suitable to simulate the very small physiological movements of the spinal cord [145]. Larger amplitudes were not possible due to the small dimensions of the chamber and the limited space on the desk of the microscope. The imposed frequencies were 1 (the minimal frequency value supportable by the shaker), 4 (the eigen frequency of the system previously calculated with numerical simulations), and 8 Hz [146].

A picture of the chamber-fibre system was taken every 5 minutes, for 30 minutes in total with the microscope. ImageJ was used to process the results measuring the displacements in the x and y direction, concerning the initial position of the fibre [147]:

$$x = \frac{x_0 - x_{30}}{t}; y = \frac{y_0 - y_{30}}{t} \qquad (5.2)$$

Where x_0 and y_0 are the coordinates of the tip of the MF close to the axle of the shaker before the test, x_{30} and y_{30} are the coordinates of the same tip of the fibre after 30 minutes, and t is the total duration of the test. The displacement was considered positive if toward the axle of the shaker (positive x-direction) and upward (positive y-direction) (Figure 5.3).

The average escape velocities $(\bar{v}_x, \bar{v}_y)$) were calculated as the average of the velocities (v) recorded every 5 minutes ($\Delta t = 300s$) during the tests:

$$\bar{v}_x = \frac{1}{3}\sum_{i=1}^{3}\frac{1}{6}\sum_{j=1}^{6}\bar{v}_j^i = \frac{1}{3}\sum_{i=1}^{3}\frac{1}{6}\sum_{j=1}^{6}\frac{x_j^i - x_{(j-1)}^i}{\Delta t} \qquad (5.3)$$

and

$$\bar{v}_y = \frac{1}{3}\sum_{i=1}^{3}\frac{1}{6}\sum_{j=1}^{6}\bar{v}_j^i = \frac{1}{3}\sum_{i=1}^{3}\frac{1}{6}\sum_{j=1}^{6}\frac{y_j^i - y_{(j-1)}^i}{\Delta t} \qquad (5.4)$$

Where the index i identifies the sample, and j is the time interval.

2.3. *Electrodes-embedding matrix debonding: pullout of the ISMS device*

2.3.1. *Samples*

Single carbon MFs (Figure 5.4b) and a simplified prototype of the final device (Figure 5.4c) were subjected to pullout tests (Figure 5.4a). The simplified prototype was composed of three x-directed MFs connected perpendicularly to one y-directed MF. The fibres of the simplified prototype were connected with cyanoacrylate glue (Loctite Super

Attack). The samples were fixed on a plastic frame with an 11x11 mm square hole. The edges of all the MFs were initially fixed to the frame.

2.3.2. Experimental setup

A PMMA container was produced with the milling machine (Figure 5.4a). The purpose of this container was to enable pullout tests from a liquid matrix with the nanotensile machine. Indeed, the machine presents the cell load under the lower grip and minimal contact with the liquid could cause damages to the machine. The sample mounted on the plastic frame was inserted in the container and the edible gelatin-water solution was poured in the PMMA container up to 2 mm circa from the edge. The plastic frame was used instead of the paper one to avoid the wetting and damaging of the frame. Moreover, the frame was useful to maintain the position of the sample once it was inserted in the PMMA chamber, subsequently filled with the gelatine. The sample-container system was then mounted in the nanotensile machine. The container presented a 3x22x0.5 mm strip that was clamped with the lower grip of the nanotensile. The top grip was clamped to the plastic frame and the *y*-directed fibre. Before being inserted in the PMMA chamber, the lower edge of the *y*-directed MF and both the edges of the *x*-directed MFs were detached from the frame. Moreover, the frame was cut close to the upper grip, on both the right and left sides, to enable the measurement of the pullout force of the fibre/simplified system from gelatin (avoiding the noise given by the frame). The single fibres and the simplified prototype were embedded for 4 and 6 mm circa, respectively.

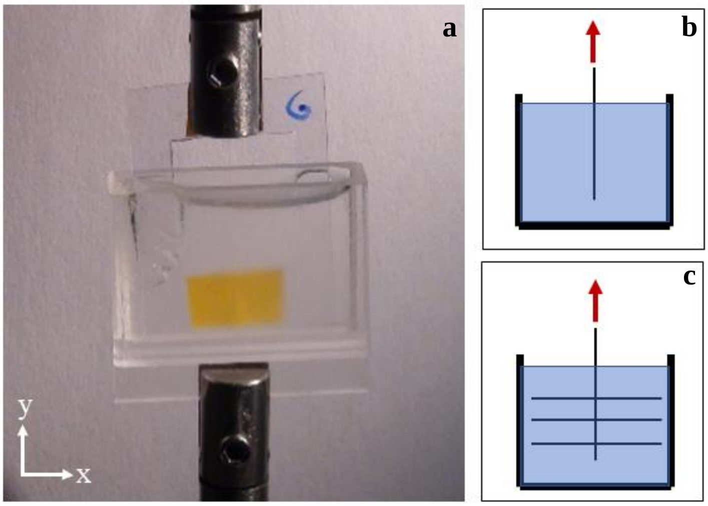

Figure 5.4 a) Picture of the experimental setup used to test the forces needed to pullout. b) Scheme of the single MF and c) the simplified prototype of the final device.

2.3.3. Pullout tests

Pull-out tests of single fibres and simplified prototypes were performed. The nanotensile machine (Agilient Technologies T150 UTM) was used to evaluate the force needed to pull the fibres out of a gelatine embedding matrix characterised by rheological properties comparable to the spinal cord environment after injury. The upper grip was clamped to the frame and the upper edge of the *y*-MF and pulled the MF/simplified system out of the gelatin in the *y*-direction. The tests were performed imposing a pullout velocity of 0.05% of strain/s.

3. Results

3.1. Failure of the embedded electronic system

Table 5.1 shows the failure strain and failure displacement reached by each type of tested prototype. Cobalt-based alloy MFs interconnected with UV glue reached the highest failure strain and displacement. However, during the tensile test on this sample, the *y*-MFs slipped out from the interconnections with the *x*-directed fibres. Thus, a proper breakage of the joints was not observed. Stainless steel MFs interconnected with UV glue and medical grade UV glue, and carbon MFs connected to the stainless steel microwire reached notable failure strains. The samples interconnected through electric welding were the weakest in terms of undergoing strains.

Table 5.1 Summary of the failure characteristics of the tested prototypes. The failure strain was calculated considering the displacement corresponding to the total failure of the tested system during tensile tests. The displacement reached when the total failure occurred during the test is reported as Failure displacement.

Microfibre (Microwire)	Joint	Failure strain [%]	Failure displacement [mm]
Cobalt-based alloy (Cobalt-based alloy)	Electric welding	5.6	1.7
Stainless steel (Stainless steel)	Electric welding	4.3	1.28
Cobalt-based alloy (Cobalt-based alloy)	UV glue	102.3	30.1
Stainless steel (Stainless steel)	UV glue	15.3	4.6
Stainless steel (Stainless steel)	Medical grade UV glue	26.6	8.0
Stainless steel (Stainless steel)	Medical grade conductive glue	7.5	2.25
Stainless steel (Stainless steel)	Chemical machining	11.6	5.4
Carbon (Stainless steel)	Silver-filled epoxy glue	23.3	6.1
Carbon (Cobalt-based alloy)	Silver-filled epoxy glue	7.3	1.6

These results were also exploited to perform an analysis of the feasibility of implanting the prototypes in specific portions of the spine. The failure strain measured during tensile tests was compared to the maximal strains measured in the cervical and thoracic area of the spine. As summarised in Table 5.2, cobalt MFs interconnected with UV glue, stainless steel MFs interconnected with medical-grade UV glue, the stainless steel plate cut with chemical machining, and the carbon MFs connected to a stainless steel microwire with silver-filled epoxy glue can be successfully inserted in each portion of the spinal cord as considered by Reid [28]. The other tested prototypes can be implanted in the thoracic tract of the spine and undergo physiological movements without breaking.

Table 5.2 Feasibility of implanting the considered device in the specific portion of the spinal cord. C is cervical, T is thoracic. Below each spinal cord segment, the maximum strain is specified in the brackets.

Microfibre (Microwire)	**Joint**	**Failure strain [%]**	**C2-5 (10.2%)**	**C5-T1 (9.7%)**	**C6-T1 (9.9%)**	**T1-5 (4.4%)**	**T5-10 (2.8%)**	**T10-12 (2.0%)**
Cobalt-based alloy (Cobalt-based alloy)	Electric welding	5.6				X	X	X
Stainless steel (Stainless steel)	Electric welding	4.3				X	X	X
Cobalt-based alloy (Cobalt-based alloy)	UV glue	102.3	X	X	X	X	X	X
Stainless steel (Stainless steel)	UV glue	15.3	X	X	X	X	X	X
Stainless steel (Stainless steel)	Medical grade UV glue	26.6	X	X	X	X	X	X
Stainless steel (Stainless steel)	Medical grade conductive glue	7.5				X	X	X
Stainless steel (Stainless steel)	Chemical machining	11.6	X	X	X	X	X	X
Carbon (Stainless steel)	Silver-filled epoxy glue	23.3	X	X	X	X	X	X

3.2. Migration of the electrodes

The rheological measurements on different gelatin-water solutions defined the 10% gelatine solution as the best candidate to mimic the spinal cord environment after SCI (Figure 5.5). The viscosity of the solution (1.92 ± 0.04 mPa·s) was indeed comparable to the viscosity of human plasma (1.43±0.02 mPa.s).

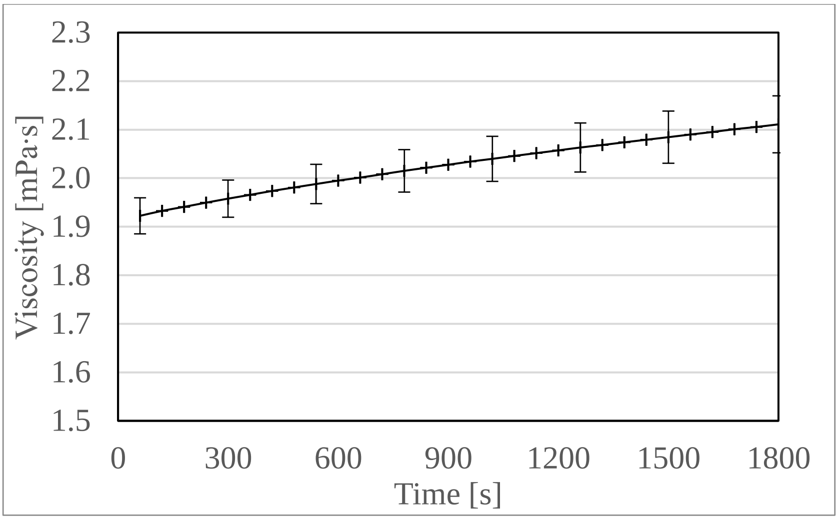

Figure 5.5 Viscosity of 10% gelatin solution measured with a cone-plate rheometer, imposing 900 s-1 shear rate, at 37° C, for 30 minutes.

The high strain transmitted to the silicon chamber when imposing 8 mm amplitude led to gelatin solution leak. By the same token, a frequency of 8 Hz caused fluid spilling. Due to these experimental limitations, amplitudes of 5 and 6 mm and frequencies of 1 and 4 Hz were imposed with the sinusoidal movement of the axle of the shaker to the silicon chamber, and hence to the gelatin and the MF. All the amplitude-frequency combinations were verified, and each combination was performed on three samples.

The analysed images showed an effective migration of the fibres in every tested condition (Figure 5.6). In 9 tests out of 10, the migration of the fibre was recorded toward the axle of the shaker (i.e., in the positive direction of *x*). The displacements and the average migration velocities in the *x* and *y* direction were calculated.

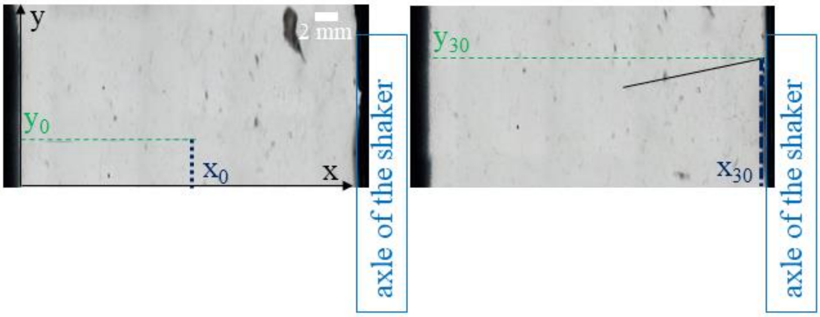

Figure 5.6 Example of how the displacements and consequently the escape velocities were calculated. The coordinates of the right (closer to the axle of the shaker) tip of the fibre were considered.

Table 5.3 summarises the results obtained.

Table 5.3 Summary of the results obtained during the experimental measurements. x and y are the mean displacements in the x and y direction respectively, $\bar{v}_x$ *is the average velocity in the x-direction and* $\bar{v}_y$ *is the average migration velocity in the y-direction*

Amplitude [mm]	**Frequency [Hz]**	x **[mm]**	y **[mm]**	$\bar{v}_x$ **[mm/s]**	$\bar{v}_y$ **[mm/s]**
5.0	1.0	0.594±0.432	0.358±0.489	0.0003±0.0002	0.0002±0.0003
5.0	4.0	6.190±4.202	1.888±2.841	0.0014±0.0005	0.0004±0.0005
6.0	1.0	0.116±0.034	0.047±0.052	0.00007±0.00005	0.00005±0.00006
6.0	4.0	7.393±4.073	2.122±1.612	0.0165±0.008	0.005±0.007

When increasing the frequency from 1 to 4 Hz, the displacement in the *x*-direction increased 10-fold (from 0.6 to 6 mm) or 70-fold (from 0.1 to 7 mm), if 5 mm or 6 mm amplitude were applied respectively. The escape velocities measured in the *y*-direction were not significant. Indeed, the standard deviations resulted higher than the mean values. Imposing 1 Hz frequency, the *x*-escape velocity resulted higher when 5 mm amplitude was used. On the contrary, stimulating the chamber with 4 Hz, the velocity in the *x*-direction increased when increasing the amplitude. Considering the tests performed with the same amplitude, the escape velocities increased by increasing the frequency. Few MFs stimulated at 4 Hz reached the opposite side of the chamber (Figure 5.7). It is thus reasonable to hypothesise that further increases of the frequency could lead to higher escape velocities, reaching an average of few millimeters per second.

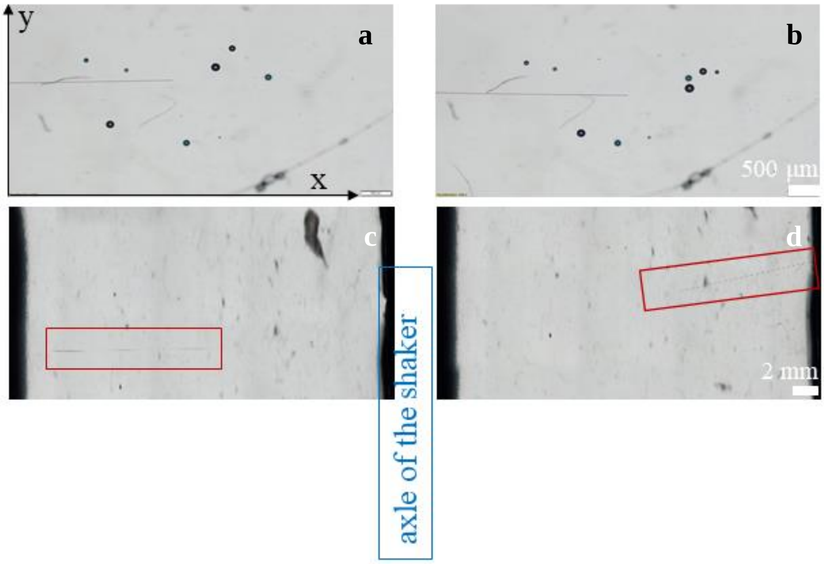

Figure 5.7 Two examples showing the migration of the fibre. Picture of the MF a) at time point 0 s and b) after 30 minutes, imposing a sinusoidal movement of 5 mm amplitude and 1 Hz frequency. Processes of a measurement in which the fibre reached the opposite border of the chamber, c) before and d) after the test.

3.3. Pullout of the eletrodes and simplified prototype

The average maximal force needed to pullout single carbon MFs from a spinal cord-like matrix was 0.334±0.134 mN (Figure 5.8). The nanotensile machine was programmed to stop when measuring a drop in the force that was 95% lower than the previously recorded value. Thus, the measurements of the tensile forces stopped at different values of displacement, due to high drops of the forces probably caused by the presence of bubbles in the matrix or light agglomerates of gelatin.

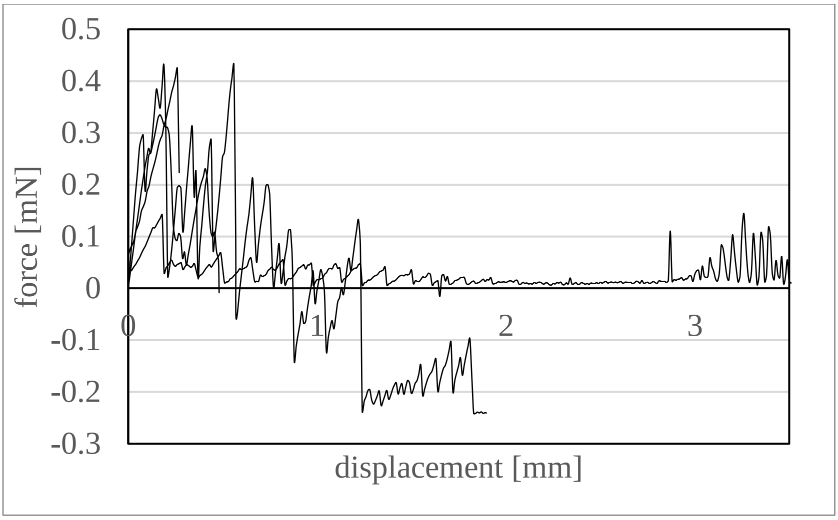

Figure 5.8 Force-displacement curves obtained during the pullout tests of single carbon MFs.

The pullout forces measured for the simplified prototype were higher than the ones recorded for single fibres. Unfortunately, the damage of the samples was also observed during the pullout, probably due to the high difficulty of making the interconnections with cyanoacrylate glue. However, the average maximal force recorded during the tests was 2.995±0.809 mN, almost 10 times higher than the single carbon MF (Figure 5.9).

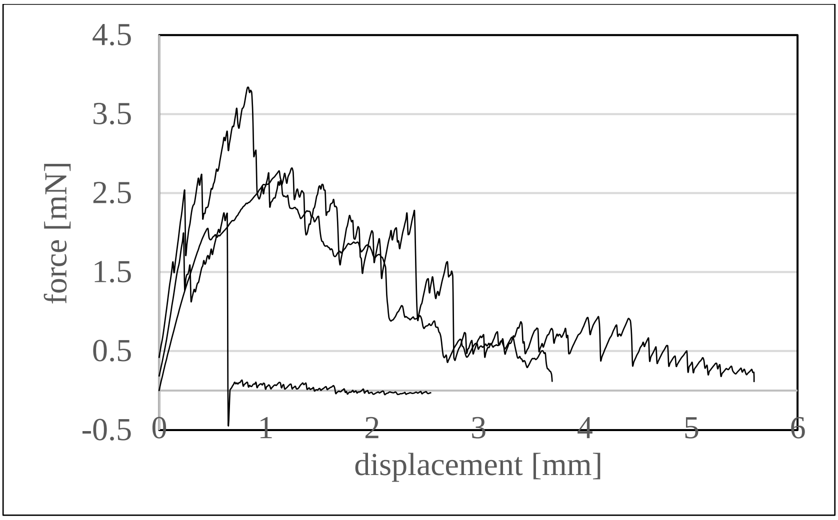

Figure 5.9 Force-displacement curves obtained during the pullout tests of a simplified prototype of the final device, composed of one y-directed carbon MF and three x-directed MFs.

An oscillating behaviour of the forces was observed, probably related to stick-slip phenomena (Figure 5.8 and Figure 5.9).

4. Conclusions

The analysis of the feasibility of implanting the device in specific segments of the spine is precautionary since the strain imposed at the single fibre is compared with the physiological strain. Despite this, the data collected give a realistic range in which every prototype maintains its integrity, while subjected to the physiological movement of the spine. Cobalt MFs interconnected with UV glue, stainless steel MFs interconnected with medical-grade UV glue, the stainless steel plate cut with chemical machining, and the carbon MFs connected to the stainless steel wire with silver-filled epoxy glue could be successfully inserted in each portion of the spinal cord, as considered by Reid [28].

Few limitations were imposed by the experimental setup designed to test the migration of the MFs (e.g., high amplitudes and frequencies were not tested). However, the here presented setup was the best solution found to simulate the small movements of the spine and simultaneously measuring the movement of the MF. During the 30 minutes of rheological measurements, the viscosity of the gelatin solution used to mimic the spinal cord increased. This change of viscosity likely occurred during the migration experiment. However, during the tests, the increase of the viscosity did not correspond to lower migration velocities and could thus be considered negligible.

The results of the experimental migration tests highlighted the possible dangerous condition of the migration of the implanted fibres, which might not maintain the designated position during the first phases of the injury. Moreover, results showed that the displacement and thus the escape velocity of the implanted microfibres are influenced by the frequency and the amplitude of the imposed bending movements. Assuming a total duration of one month of the acute phase [148] and an average movement of the spine for 1 hour per day, the fibre could migrate 7 mm circa far from the specific implantation point, longitudinally to the spinal cord. The aim of the work was also understanding the eventual precautionary measures to prevent the displacement of the fibres. Results clearly showed the need for an anchorage point or a system that could limit the movements or even immobilise the spine at least in the injured tract, during the first phases of patient recovery.

Even though experiments showed a reduced risk of pullout of simplified prototypes (and thus structures similar to the final configuration of the Neurofibres ISMS device) compared to single MFs, the possible failure due to the dislocation of the device caused by pullout forces was confirmed.

Given the results of the experiments, specific anchorage systems are needed to avoid the loss of efficiency of the ISMS device or, in the worst case, the complete failure of the treatment.

Work performed in collaboration with: Dr. Andrea Rodella (Laboratory for Bioinspired, Bionic, Nano, Meta Materials & Mechanics, Department of Civil, Environmental and Mechanical Engineering, University of Trento, Via Mesiano 77, 38123 Trento, Italy; currently at Sapienza, University of Rome) who performed the numerical simulation to investigate the eigen frequencies, prof. Diego Misseroni (Laboratory for Bioinspired, Bionic, Nano, Meta Materials & Mechanics, Department of Civil, Environmental and Mechanical Engineering, University of Trento, Via Mesiano 77, 38123 Trento, Italy) who was involved in the design and development of the experimental setups.

Chapter 6 Investigating the effect of electric fields on *bombyx-mori* silk fibroin hydrogels

1. Introduction

The electrical stimulation was proven capable of restoring anatomical and functional recovery after SCI [16]. Through the application of weak electric fields, direct current fields, and oscillating fields several studies showed an increase in axons and neurites growth and regeneration [17], [24], [149]–[151]. Electrical stimulations are thus studied to achieve a favourable environment for regeneration after the loss of functional and structural continuity due to SCI using different approaches, such as Functional Electrical Stimulation (FES) and ISMS [16]. Both these approaches require the use of electrodes implanted in specific spinal nerves (FES) or directly inserted in the injured spinal cord (ISMS) to reach specific neural circuits, and external devices to generate the electric stimulation [16]. The connection with external devices requires specific wires and connectors that are susceptible to many risks, such as the joints between different wires or possible infections.

Polymers with crystalline domain, which have non-centrosymmetric nature, can convert mechanical energy into electrical energy or vice versa, and show intrinsic piezoelectricity, an electrical polarization perpendicular to the deformation [31], [152]. The presence of an intrinsic current or a voltage produced during small deformations of the material in contact with the spinal cord tissue could avoid external stimuli supply. Among the different piezoelectric biomaterials available, silk shows piezoelectric properties. The intrinsic shear piezoelectricity of silk fibre bundles measured by Fukada et al. [31] revealed a value of ~1 pC/N, near to the quartz crystal (~2 pC/N). This intrinsic shear piezoelectricity of silk could be due to the overall β-sheets content and the uniaxial molecular alignment [32]. Indeed, silk fibres are well oriented and fibroin molecules form β-sheet structures when crystallizing [153]. Thus, a high degree of β-sheet crystallinity and high orientation improve the piezoelectric effects of silk. Many techniques have been studied to improve the β-sheet crystallinity of silk fibroin (SF). Exposing fibroin to hot water vapor [33], as well as icing methods [34] were proven efficient in augmenting the degree of β-sheet crystallinity. Yucel et al. [32] designed a processing toolkit to maximize silk crystallinity and crystal alignment. Recently, electric fields in alternating current (AC) were applied on casting fibroin films to manipulate the alignment of molecular dipoles [36].

However, the regeneration of the central nervous system requires the use of 3D of structures with soft mechanical properties and high deformability, such as hydrogels-based biomaterials [154]–[157]. *Bombyx mori* silk fibroin is a fibrillar protein composing the core part of the silkworm filament. It is a highly versatile material, largely investigated for tissue engineering applications.

The final aim of this work has been to fabricate a SF hydrogel with piezoelectric properties as a scaffold for the regeneration of the spinal cord. To obtain a piezoelectric structure, the approach of Servoli et al [36] was used, and thus electric fields were applied to SF solutions, and hydrogels were produced. An ad hoc experimental setup was built to stimulate a previously sonicated (50% amplitude, 1 minute) silk fibroin solutions with 24 and 220 V. The first step done to evaluate eventual changes in the structure of hydrogels was their mechanical characterization. Compression tests were performed and the obtained compressive Young’s modulus was used as a reference parameter to assess changes in the structures due to the electric treatments. Moreover, piezoelectric measurements were done with a specific experimental setup.

2. Materials and methods

2.1. *Preparation of silk fibroin solution*

Dried *Bombyx mori* silk cocoon (Chul 2 type, purchased from Chul Thai Silk Co., Phetchabun, Thailand) were degummed to eliminate sericin from silk following a standard protocol. *Bombyx mori* cocoons were treated twice with Na2CO3 aqueous solution (1.1 g/L) at 98 °C (1.5 h for each treatment) and rinsed with distilled water. The degummed silk fibroin was dried under the fume hood for 18 hours and dissolved in a lithium bromide (LiBr) 9.3 M solution (1 g/10 mL) at 65 °C for 4 h. The solution was dialyzed in a Slide-A-Lyzer Cassette (ThermoScientific, MWCO 3500 Da), against distilled water for 3 days. The concentration of the solution measured after filtration was 20 mg/ml (stock solution). For further steps, the solution has been concentrated by dialysis against polyethylene glycol to 3, 5, 7, and 9 % w/v.

2.2. Experimental setup

An ad hoc experimental setup was designed and developed to stimulate the fibroin solution with 24 and 220 V [36]. Five systems of 4 borosilicate chambers (57x25 mm, Lab-Tek® II Chambered #1.5 German Coverglass System) were used as containers (Figure 6.1) for the fibroin solutions, previously sonicated to start the gelation process (50% amplitude for 1 minute).

Figure 6.1 Borosilicate chamber used as a container for silk fibroin solutions.

Two stainless steel bars (100x4.6 mm) were glued to the longer sides of the systems, except for the system reserved for the controls (Figure 6.2). The bars were used to impose the electric field to the solution inside each chamber. The experiment consisted of the application of AC and DC electric fields through 24 and 220 V [4]. The system used to impose 220 V was directly connected to the socket. A voltage of 24 V was imposed with a transformer. The direct current was handled with a security system developed for these experiments (Figure 6.2). The connections between the transformer/socket and the two stainless steel bars of each chambered system were done with two fastons (one for the positive pole and one for the negative one) and insulated copper wires (Figure 6.2). The setup in toto was incubated at 37° C and the electric fields were imposed for 24 hours, until gelation. Given the geometrical and electrical features of the setup, the imposed electric fields were 0.27 (24V) and 2.51 (220V) V/mm.

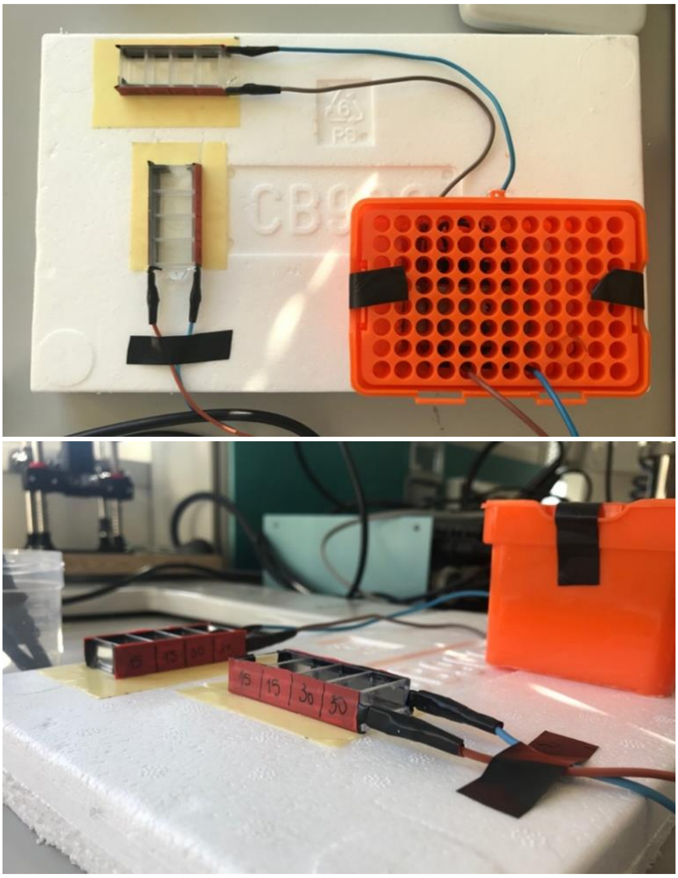

Figure 6.2 Experimental setup conceived to impose 24 and 220 V to silk fibroin solutions. The chambers reserved for the stimulation with 24 V are connected to a transformer which was isolated in the orange plastic box. The chamber used to impose 220 V was directly connected to the socket.

2.3. Preparation of hydrogels

Four solutions with different fibroin concentrations (3, 5, 7, 9 % w/v) were prepared, concentrating the stock solution. 1 ml of solution was poured in a 1.5 ml Eppendorf and sonicated at 50% amplitude for 1 minute. In each of the 4 borosilicate chambers was thus poured 1 ml of the sonicated solution. The chambers were covered with parafilm and with their caps to avoid water evaporation. After gelation with or without the electric field, the specimens were extracted from the original rectangular hydrogel formed in the borosilicate chamber. A die cutter was used to obtain cylindrical specimens with a 1:1 ratio between diameter and height, to avoid buckling during compression [158]. The specimens were extracted perpendicular (die cutter diameter=8mm) and parallel (die cutter diameter=4mm) to the electric field lines (or to the upward surface of the rectangular hydrogel for the controls) (Figure 6.3a and b). Different dimensions of die cutters were due to the geometry of the hydrogel produced in the borosilicate chamber. The specimens were kept at 4°C and immersed in distilled water up to the test.

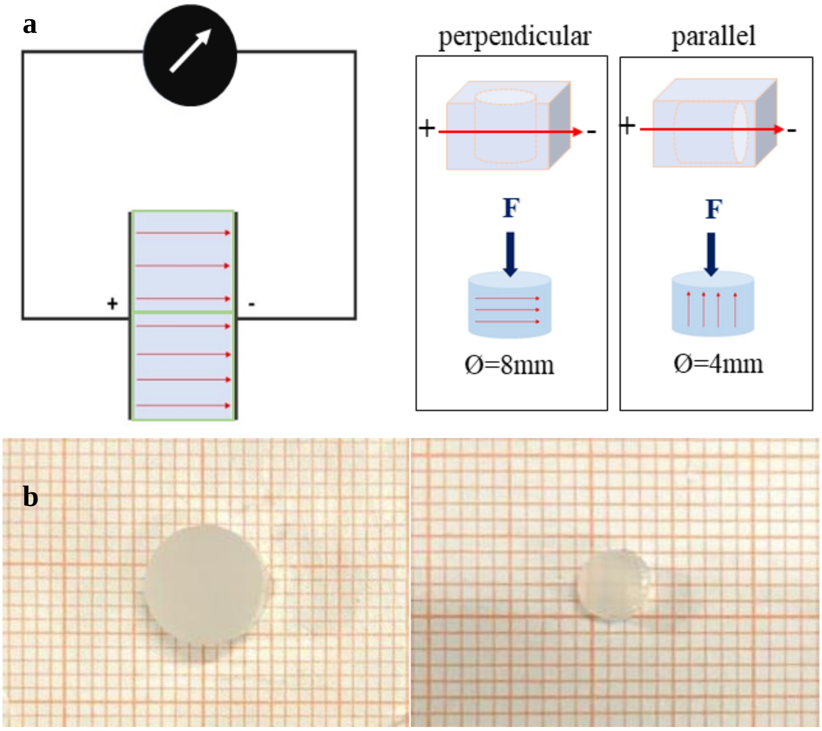

Figure 6.3 a) Scheme of the two types of samples extracted from the hydrogel formed in the borosilicate chambers. The specimens were extracted perpendicular (die cutter diameter=8mm) and parallel (die cutter diameter=4mm) to the electric field lines. b) Pictures of the perpendicular (left) and parallel (right) samples.

2.4. Compression test

The mechanical characterisation of the samples was performed to evaluate the eventual changes in the structural properties due to the treatment with the electric fields. Samples were tested with Messphysik MIDI 10-20 machine, equipped with a Leane DBBSM 1 kg load cell used with compression module (Figure 6.4). Unconfined compression tests were performed at room temperature at an extension-controlled rate of 0.02 mm/s [159]. Force and displacement were measured during the tests. The engineering strain was calculated by dividing the displacement by the initial height of the sample. The engineering stress was given by the ratio between the recorded force and the cross-sectional area of the sample. The compressive modulus of the samples was calculated as the slope of the initial linear elastic region of the stress-strain curve after the initial assessment of the sample [160]. The cross-sectional areas of each sample were precisely measured with ImageJ [161]. A digital caliper was used to measure the thickness (i.e., height) of the samples. The flat bottom part of the caliper was utilized and close attention was paid to avoid the deformation of the tissue while measuring.

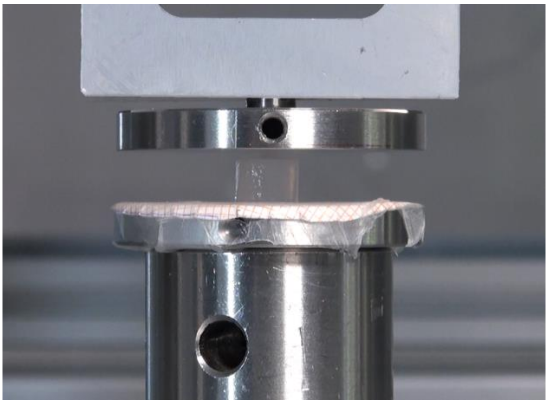

Figure 6.4 Setup for the compression tests performed on the hydrogels.

3. Results

3.1. Compression test

The stress-strain curves obtained with the compression tests on all types of samples revealed a sigmoid increase of the stress (Figure 6.5). An initial assessment of the sample was followed by a linear elastic behaviour up to the formation of the cracks, and consequent permanent damage of the sample, and decrease of the recorded stress.

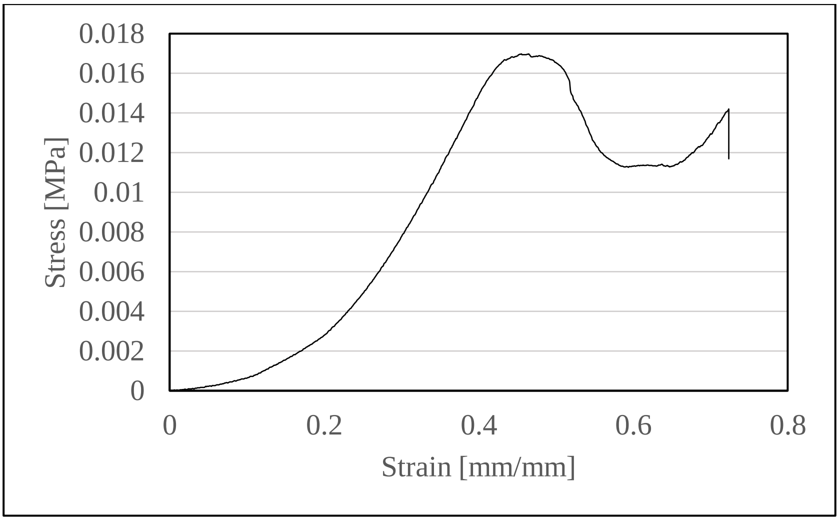

Figure 6.5 Stress-strain curve obtained during a compression test on a 3% SF hydrogel, treated with 24 V AC.

The parallel and perpendicular specimens were first tested and compared to the controls to investigate structural changes due to the applied electric field. The results obtained with compression tests are summarized with histograms.

The 3% SF samples treated with electric fields showed higher stiffness (Figure 6.6). Samples stimulated with DC were stiffer than the ones treated with AC if the load was applied perpendicularly to the field lines, but the opposite situation happened if the load was applied parallel to the field lines. 24 and 220 DC treated samples resulted significantly different from the control.

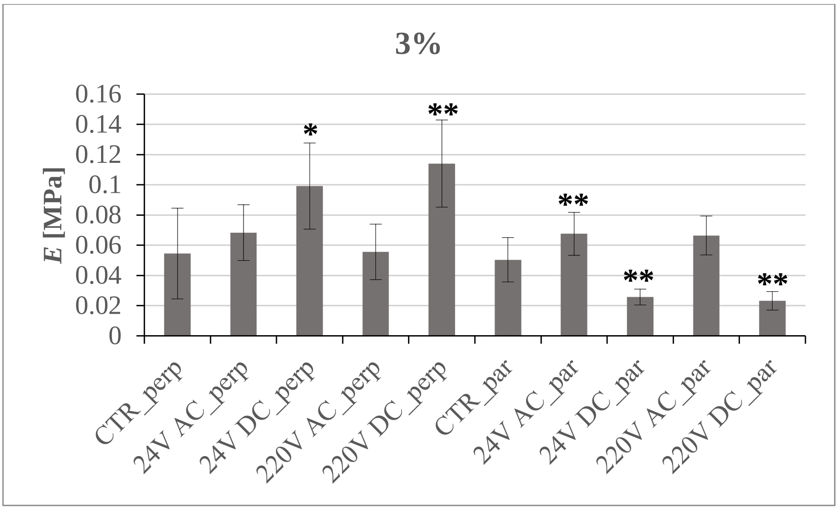

*Figure 6.6 Average elastic modulus (E) of each type of sample obtained with 3% fibroin solution. The samples labelled with "perp" are the ones tested applying the compressive load perpendicular to the electric field; the samples labelled with "par" are the ones tested applying the compressive load parallel to the electric field. Student t-test was performed to evaluate the difference between treated samples and the corresponding control: * $p<0.05$, **$p<0.01$. T-test was also executed to assess the asymmetry of the structures, i.e., statistically significant difference between samples that underwent the same treatment but loaded perpendicular and parallel to the electric field lines (ex. 24 V, AC, perp VS 24V, AC, par): * $p<0.05$, **$p<0.01$.*

Considering the samples composed of 5% SF (Figure 6.7), unfortunately very high standard deviations were reported. However, all the treated samples loaded parallel to the electric field lines resulted different from the corresponding control. Samples treated with DC showed asymmetry (i.e., significant difference in the stiffness measured in the two different compression testing configurations). DC seemed to produce stiffer hydrogels.

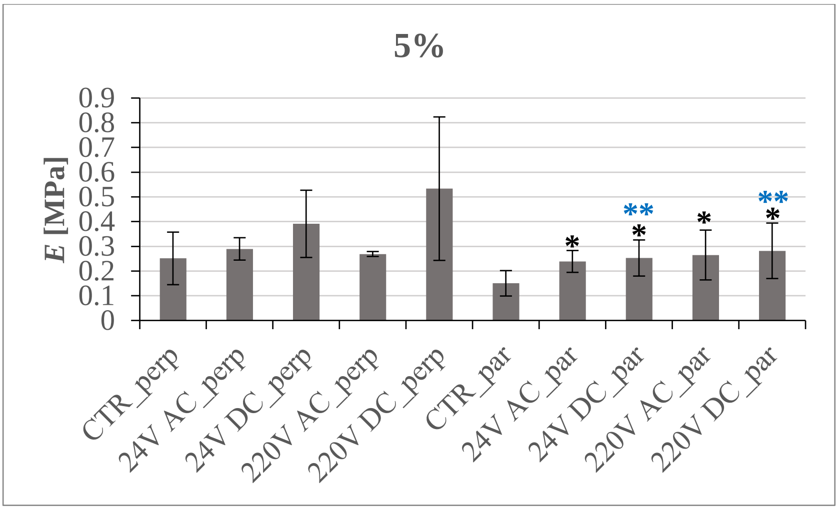

*Figure 6.7 Average elastic modulus (E) of each type of sample obtained with 5% fibroin solution. The samples labelled with "perp" are the ones tested applying the compressive load perpendicular to the electric field; the samples labelled with "par" are the ones tested applying the compressive load parallel to the electric field. Student t-test was performed to evaluate the difference between treated samples and the corresponding control: * $p<0.05$, **$p<0.01$. T-test was also executed to assess the asymmetry of the structures, i.e., statistically significant difference between samples that underwent the same treatment but loaded perpendicular and parallel to the electric field lines (ex. 24 V, AC, perp VS 24V, AC, par): * $p<0.05$, **$p<0.01$.*

Even if data showed an asymmetric structure of 7% samples (Figure 6.8), the asymmetry was also found in controls. Thus, these results are ambiguous since in this case, the asymmetry would be an intrinsic characteristic of the hydrogel in general.

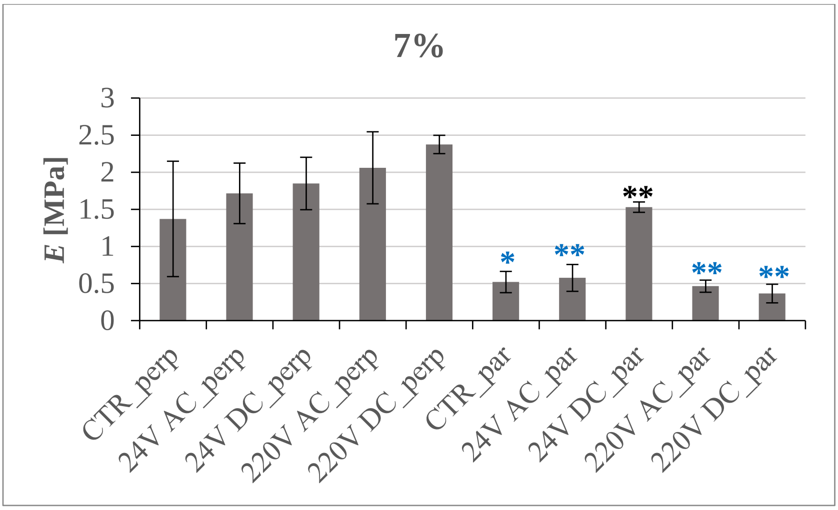

*Figure 6.8 Average elastic modulus (E) of each type of sample obtained with 7% fibroin solution. The samples labelled with "perp" are the ones tested applying the compressive load perpendicular to the electric field; the samples labelled with "par" are the ones tested applying the compressive load parallel to the electric field. Student t-test was performed to evaluate the difference between treated samples and the corresponding control: * $p<0.05$, **$p<0.01$. T-test was also executed to assess the asymmetry of the structures, i.e., statistically significant difference between samples that underwent the same treatment but loaded perpendicular and parallel to the electric field lines (ex. 24 V, AC, perp VS 24V, AC, par): * $p<0.05$, **$p<0.01$.*

Significant different Young's moduli were found for 9% samples treated with 24V, tested perpendicular to the field lines and samples treated with 24V, and tested parallel to the lines (Figure 6.9).

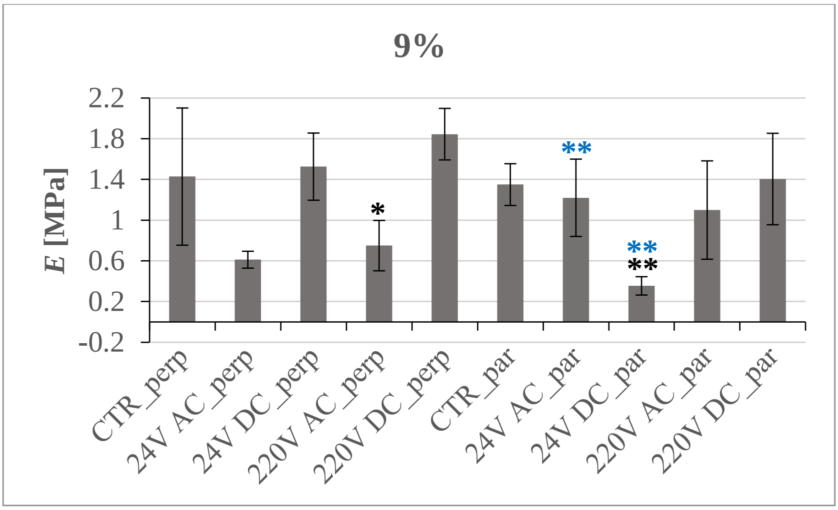

*Figure 6.9 Average elastic modulus (E) of each type of sample obtained with 9% fibroin solution. The samples labelled with "perp" are the ones tested applying the compressive load perpendicular to the electric field; the samples labelled with "par" are the ones tested applying the compressive load parallel to the electric field. Student t-test was performed to evaluate the difference between treated samples and the corresponding control: * $p<0.05$, ** $p<0.01$. T-test was also executed to assess the asymmetry of the structures, i.e., statistically significant difference between samples that underwent the same treatment but loaded perpendicular and parallel to the electric field lines (ex. 24 V, AC, perp VS 24V, AC, par): * $p<0.05$, ** $p<0.01$.*

3.2. New experimental setup

An improved setup was designed and developed to decrease the high variations in the results obtained with the first experimental setup (Figure 6.10). This new approach aimed to obtain samples with flat surfaces and homogeneous heights. The new setup was based on a series of 10 chambers obtained using the milling machine from a piece of PMMA. These chambers did not have a cap and the bottom. The caps series was milled from PMMA (thickness 5mm) and presented 10 steps (2mm) that wedged in each chamber. The bottom was a simple milled PMMA slab (thickness 5mm).

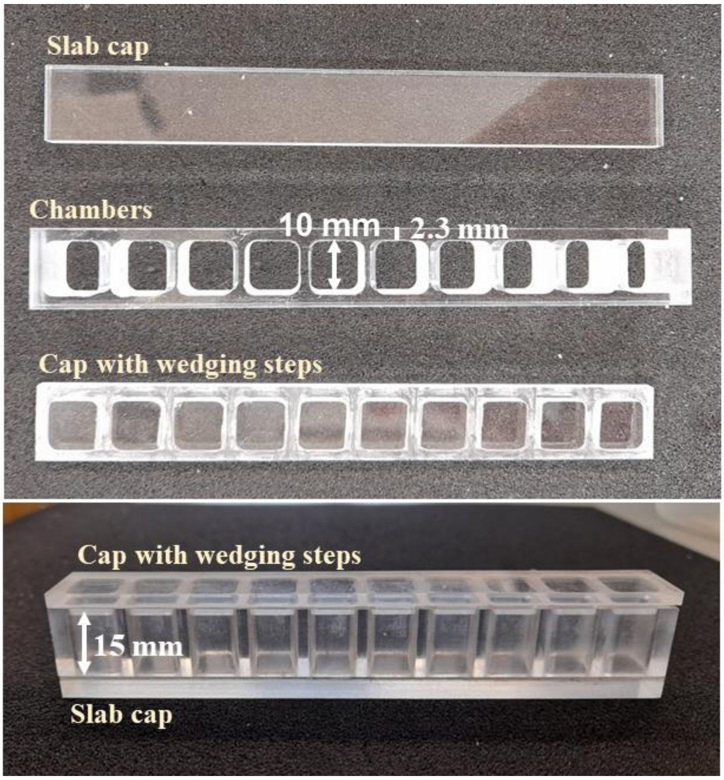

Figure 6.10 Components of the improved experimental setup.

The caps were wedged, and the silk fibroin solution was poured into the chambers. The slab was positioned. This double cap approach was needed to obtain regular geometrical shapes and avoid the formation of an air layer when turning upside down the chamber-cap system. Moreover, removing the formed hydrogels after gelation was easier: the slab was pulled out and regular cubes were extracted from the chambers. The electric field was imposed with aluminium bars (Figure 6.11). The dimensions of the chambers were defined to obtain the same value of the electric field imposed with the first experimental setup. The samples produced with this setup were hydrogels with 3% fibroin, treated with 24V C, 220V AC, and not treated.

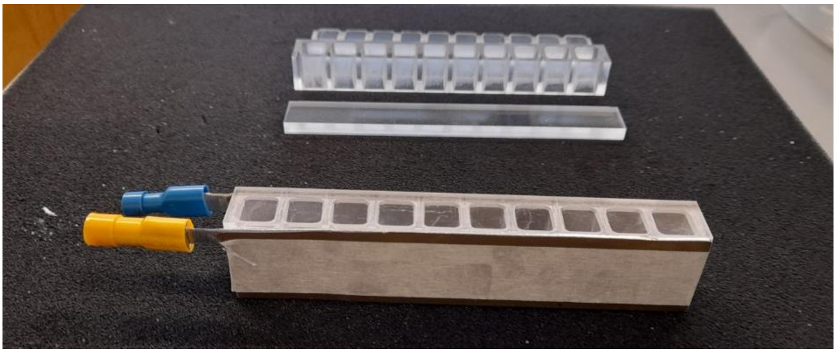

Figure 6.11 The electric field was imposed with aluminium bars even in the improved version of the experimental setup.

The obtained hydrogels were characterised with compression tests, following the protocol of the first samples obtained with the first experimental setup. However, the die-cut was not used and the whole specimens were tested. To impose the compression, load parallel to the electric field lines, the samples were turned and compress on the lateral side (Figure 6.12).

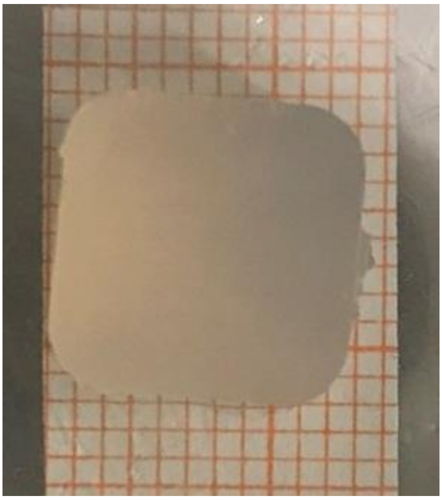

Figure 6.12 Sample produced with the new experimental setup, view from the top. The load was applied perpendicular to the surface here visible and thus to the electric field lines.

The stress-strain curves recorded during the compression tests are presented in Figure 6.13, Figure 6.14, Figure 6.15, Figure 6.16, Figure 6.17, and Figure 6.18.

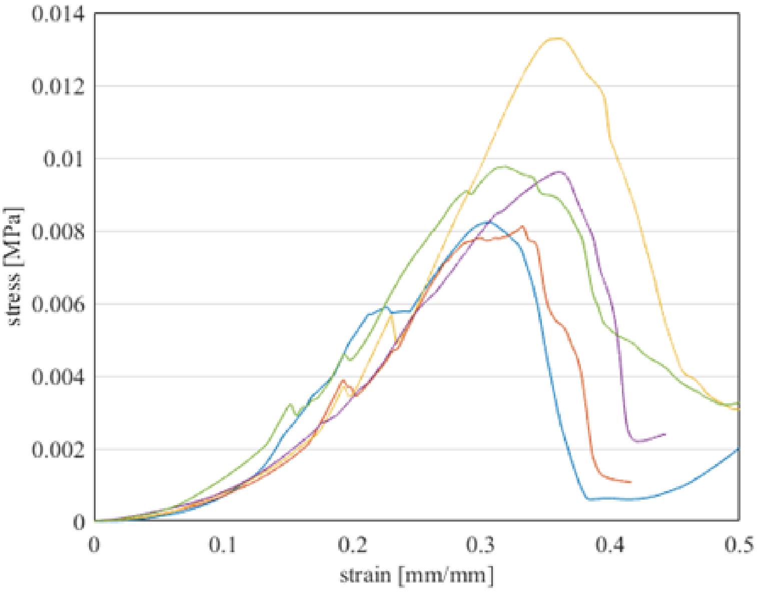

Figure 6.13 Stress-strain curves recorded with compression tests on 3% SF hydrogels (control), applying the load perpendicular to the electric field lines.

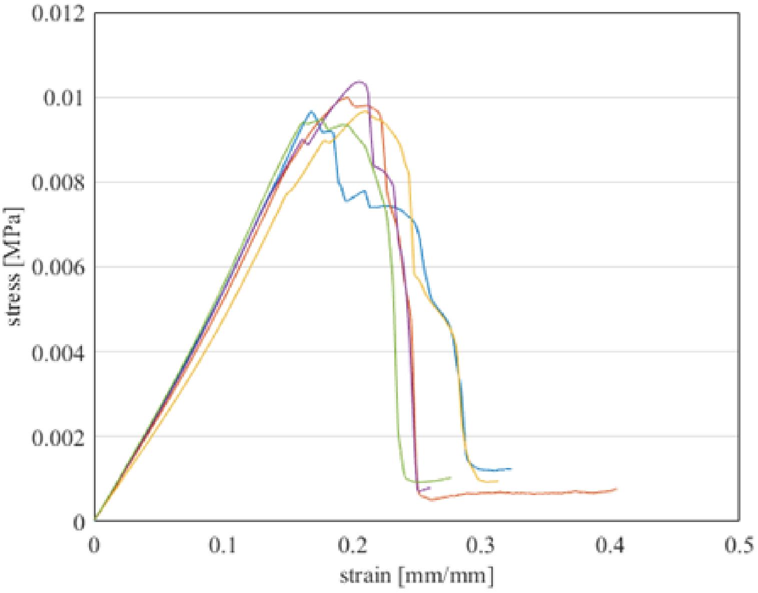

Figure 6.14 Stress-strain curves recorded with compression tests on 3% SF hydrogels (control), applying the load parallel to the electric field lines.

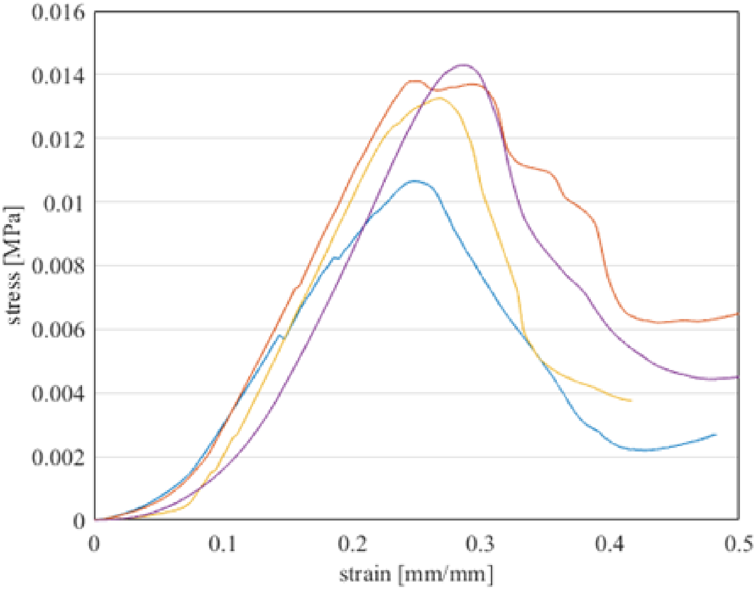

Figure 6.15 Stress-strain curves recorded with compression tests on 3% SF hydrogels treated with 24V AC, applying the load perpendicular to the electric field lines.

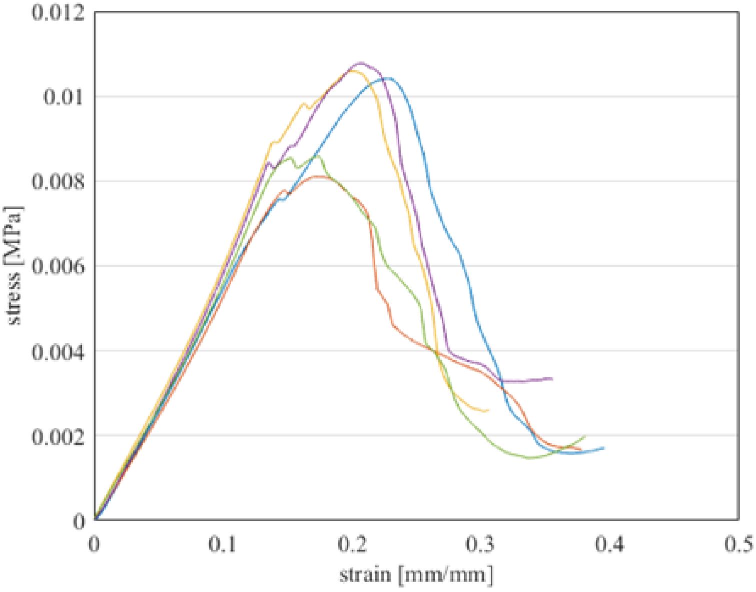

Figure 6.16 Stress-strain curves recorded with compression tests on 3% SF hydrogels treated with 24V AC, applying the load parallel to the electric field lines.

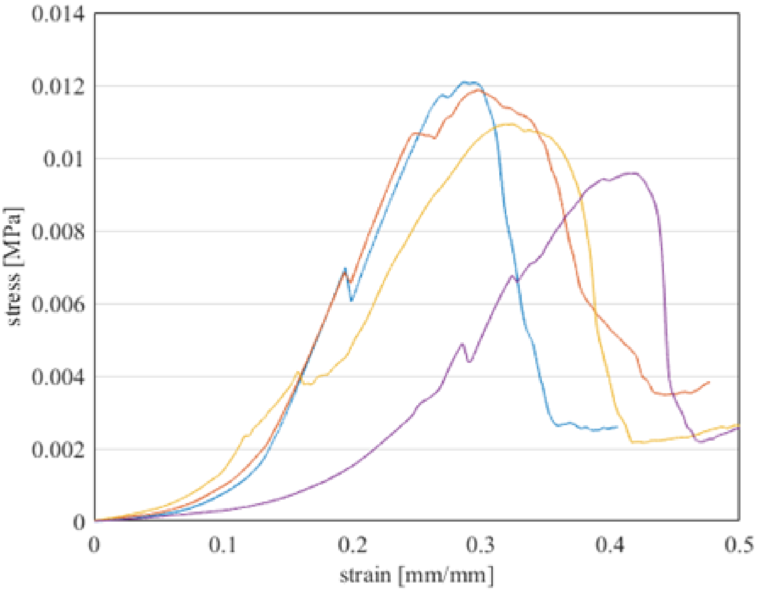

Figure 6.17 Stress-strain curves recorded with compression tests on 3% SF hydrogels treated with 2204V AC, applying the load perpendicular to the electric field lines.

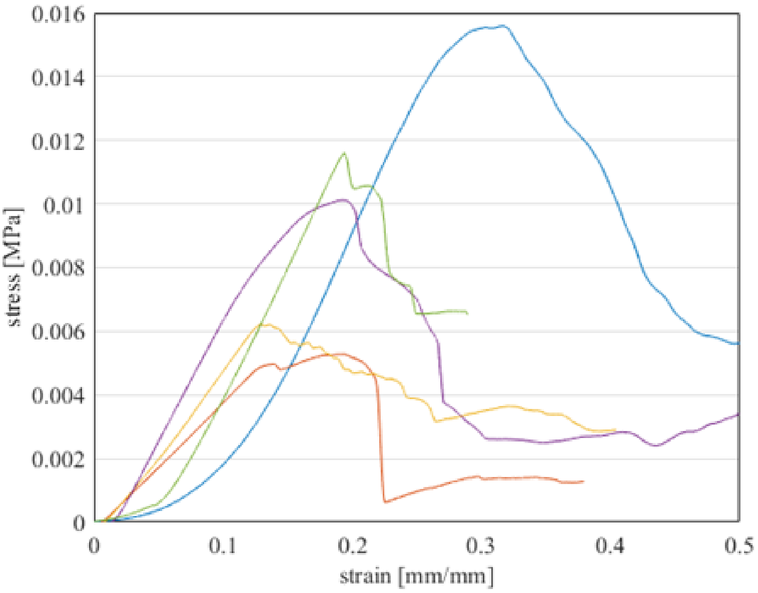

Figure 6.18 Stress-strain curves recorded with compression tests on 3% SF hydrogels treated with 220V AC, applying the load parallel to the electric field lines.

The obtained Young's moduli are summarised in Figure 6.19. The standard deviations decreased concerning the data obtained with the first experimental setup. Significant differences were found between the control and the treated samples, loaded perpendicular to the electric field lines.

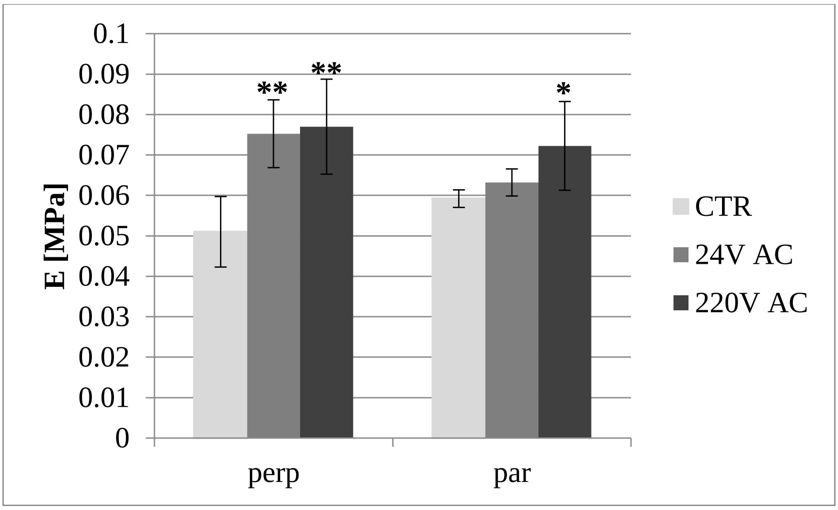

*Figure 6.19 Average elastic modulus (E) of each type of the samples obtained with the improved experimental setup. Only 3% SF solutions treated with 24 and 220V AC were used to test this new setup. The samples labelled with "perp" are the ones tested applying the compressive load perpendicular to the electric field; the samples labelled with "par" are the ones tested applying the compressive load parallel to the electric field. Student t-test was performed to evaluate the difference between treated samples and the corresponding control: * $p<0.05$, **$p<0.01$.*

4. Conclusions

Mechanical properties were studied to investigate possible changes in the structure to the electric field treatments. Compression tests were performed on the hydrogels, applying the load perpendicularly and parallel to the electric fields' lines. It was not possible to establish a common pattern for the four different concentrations of SF tested. The only result occurring in each concentration was the statistically significant difference of the samples treated with 24V DC and tested parallel to the electric field lines.

The variation in the stiffness measured with the two different loading configurations was hypothesized as proof of the asymmetric structure of the hydrogels, and thus of the possible alignment of the beta-structure.

A plausible cause of the variability of results could be the imperfect geometry of the cylindrical samples extracted with the die cutter. However, no alternatives were found to obtain samples from the first developed experimental setup for the different load configurations. Cutting the sample frozen in liquid nitrogen could have produced regular surfaces, however at the expense of artifacts due to conformation changes in the fibroin caused by temperature.

The improved experimental setup was proven successful in decreasing the variability of results. Significant differences were found between control and treated samples.

Work performed in collaboration with: Dr. Sofia Santi (BIOTech Research Center and European Institute of Excellence on Tissue Engineering and Regenerative Medicine, University of Trento, Via delle Regole 101, 38123 Trento, Italy) who was equally involved in the idea, design, and development of this study; prof. Claudio Migliaresi (BIOTech Research Center and European Institute of Excellence on Tissue Engineering and Regenerative Medicine, University of Trento, Via delle Regole 101, 38123 Trento, Italy) who guided the design, development, and characterisation of the hydrogels, and revised the work.

General conclusions

The first part of this thesis provides a comprehensive study on the mechanical behaviour of ISMS electrodes, their interconnections, and their interplay with the host tissue was performed.

An extensive literature research was done to investigate possible minimal invasive solutions. Injectable scaffolds seem to be promising to achieve this goal (Chapter 1).

The mechanical validation of a set of electrodes was performed using experimental measurements and analytical and numerical calculations (Chapter 2). A method was proposed to establish the electrode with the best mechanical performance, based on standard mechanical properties (strength, ultimate strain, Young's Modulus, toughness modulus) and practical features. Indeed, analytical calculations led to the definition of properties as the Easy Initial Penetration, the Easy Manipulations, or a simplified representation of curvature. These properties were defined from issues identified in handling and grafting the electrodes: possible damages when pulling the MFs in the tissue, the dangerous bending, contacts between the fibres, and the consequent possible harm. The proposed method is represented by a matrix in which a ranking of each property is presented. Thus, identifying the best electrodes for each property, and finally, the electrode with the best performance, is facilitated. Moreover, the matrix could be enriched with other properties (chemical, biological, etc.), and a comprehensive view of each electrode could be possible. Analytical and numerical models of the interconnection between fibres were also performed and enriched the knowledge on the mechanical behaviour of simplified prototypes of the ISMS system.

Tensile tests on bare carbon MF and carbon MFs coated with different types of graphene showed a decrease in the stiffness after the coating treatment (Chapter 3). Higher strains and toughness were measured in the graphene-coated fibres. The comparison between the surface properties of bare and GO-coated MFs gave interesting results. Slow and repeated immersion in polar liquids likely increased the heterogeneity of the coated surface. Thus, a hydrophilic tissue attacks the coating. However, the extracellular matrix of the spinal cord tissue is mostly composed of hydrophobic collagen, and the implanted coated fibres maintain their stability.

Both types of fibres showed a strong basic component of the surface free energy, and thus acid components might be the best candidates to functionalise the surface of these fibres.

The tested prototypes of the final device presented considerable rigidity and fragility (Chapter 4). Thus, the multiple MFs joints are potential breaking points leading to device failure, and protections for the handling and implanting of the systems are needed. However, electric welding, medical-grade UV glue, and silver-filled epoxy glue reached the highest adhesion energies and thus resulted in the best methods to interconnect the MFs. Considering the physiological strains of the spinal cord, cobalt MFs interconnected with UV glue, stainless steel MFs interconnected with medical-grade UV glue, the stainless steel plate cut with chemical machining, and the carbon MFs connected to the stainless steel wire through silver-filled epoxy glue could be successfully inserted in each portion of the cervical and thoracic spine (Chapter 5). The migration of the electrodes due to the physiological small movements of the spine were quantified around few millimiters in one month (considering 1 hour movement per day, during the acute phase) with an ad hoc experimental set up. Tests on single carbon MFs and a simplified prototype of the ISMS device underlined a common dangerous pullout condition when a force of 0.3 and 3 mN is applied respectively.

The second part of the thesis focused on the tissue engineering approach to SCI (Chapter 6). The experimental setups designed to stimulate the fibroin solution during gelation with electric fields resulted successful. Electric fields change the structure of hydrogels, but the results are affected by the irregularities of the sample geometry, especially the surface. Further tests should be performed to investigate why and how the structure of the hydrogel changes when an electric field is imposed. Moreover, a compression test on slices cut at different heights of the samples obtained with the second experimental setup should be performed. Through this study, the hypothesis of water evaporation could be confirmed or denied.

Concluding remarks and future perspectives

Nowadays, research is moving toward a more sustainable way of performing experiments and obtaining reliable results in terms of material and animal sacrifice. The proposed method is a valuable tool to evaluate the mechanical performance of the electrodes, avoiding the waste of material and the sacrifice of animals. Indeed, the presented evaluation method aims to overcome the definition on electrodes' feasibility limited to the stiffness and on the results obtained in the in vivo steps. Thus, this thesis combines the aim of performing a comprehensive mechanical characterisation of the innovative device for intraspinal stimulation developed in Neurofibres and performing a step forward in the definition of methods to obtain results useful for the design and developing stages of project focused on electrodes-based devices. Moreover, the failure mechanisms investigated in this work describe possible dangerous condition during the in vivo using of the device, quantifying these conditions and allowing consequent definition of missing features. In particular, the study defines the possible implanting area of the spine for each type of prototype tested, quantifies the displacement of the electrodes if not anchored, and proposes eventual features to avoid pullout phenomena. In conclusion, this work of thesis represents a step forward in defining a method to evaluate the feasibility of using specific electrodes (material, shape, dimensions) for intraspinal microstimulation devices. However, further improvements could be performed to achieve a complete mapping and consequent prevention of the failure mechanisms of the device. The study on the migration could include the investigation of other movements as well as the flection of the spine. This measurement could be improved by designing an experimental setup mimicking the macro movements of the spine. The conditions of physiological and fibrotic spinal cord tissue could be analysed by using different edible gelatine solutions (i.e., stiffer). The use of Artificial Cerebrospinal Fluid (ACF) could be considered.

The here presented study on fibroin hydrogels represents a first step in the use of piezoelectric hydrogels as possible solution for the regeneration of nervous tissue to overcome the need of external stimulator to impose electrical stimuli to the injured spine. The mechanical tests show possible changes in the structure, meaning possible alignment of the nano and microstructure and consequent increase of the piezoelectricity. However, the investigation of eventual changes in the bulk structure of the gels due to the treatment with electrical fields must be enhanced with further analysis, such as differential scanning calorimetry (DSC, to evaluate the content of water in the different gels), infrared spectroscopy (IR, to assess the secondary structures), and describing the polymerisation of the hydrogels with specific techniques. Moreover, the variability of the mechanical properties should be addressed by investigating the structure of smaller layer of the hydrogels.

References

[1] International Perspectives on Spinal Cord Injury. 2013. doi: 10.1007/978-1-4899-1028-8_18.

[2] NSCISC, “Spinal cord injury facts and figures at a glance,” Facts and Figures at a Glance. p. 2, 2018. doi: 10.1179/204577212X13237783484262.

[3] “Global Health Estimates 2016: Disease burden by Cause, Age, Sex, by Country and by Region, 2000-2016,” Geneve, 2018.

[4] M. Gazdic et al., “Stem Cells Therapy for Spinal Cord Injury,” International Journal of Molecular Sciences, vol. 19, no. 4, p. 1039, 2018, doi: 10.3390/ijms19041039.

[5] M. T. Fitch and J. Silver, “CNS injury, glial scars, and inflammation: Inhibitory extracellular matrices and regeneration failure,” Experimental Neurology, vol. 209, no. 2, pp. 294–301, 2008, doi: 10.1016/j.expneurol.2007.05.014.

[6] A. Ertürk et al., “Three-dimensional imaging of the unsectioned adult spinal cord to assess axon regeneration and glial responses after injury,” Nature Medicine, vol. 18, no. 1, pp. 166–171, 2012, doi: 10.1038/nm.2600.

[7] N. A. Silva, N. Sousa, R. L. Reis, and A. J. Salgado, “From basics to clinical : A comprehensive review on spinal cord injury,” Progress in Neurobiology, vol. 114, pp. 25–57, 2014, doi: 10.1016/j.pneurobio.2013.11.002.

[8] A. Hurtado et al., “Robust CNS regeneration after complete spinal cord transection using aligned poly-l-lactic acid microfibers,” Biomaterials, vol. 32, no. 26, pp. 6068–6079, 2011, doi: 10.1016/j.biomaterials.2011.05.006.

[9] A. Alves-Sampaio, C. García-Rama, and J. E. Collazos-Castro, “Biofunctionalized PEDOT-coated microfibers for the treatment of spinal cord injury,” Biomaterials, vol. 89, pp. 98–113, 2016, doi: 10.1016/j.biomaterials.2016.02.037.

[10] T. Xia et al., “The combination of db-cAMP and ChABC with poly(propylene carbonate) microfibers promote axonal regenerative sprouting and functional recovery after spinal cord hemisection injury,”

Biomedicine and Pharmacotherapy, vol. 86, pp. 354–362, 2017, doi: 10.1016/j.biopha.2016.12.045.

[11] J. E. Collazos-Castro, G. R. Hernández-Labrado, J. L. Polo, and C. García-Rama, "N-Cadherin- and L1-functionalised conducting polymers for synergistic stimulation and guidance of neural cell growth," Biomaterials, vol. 34, no. 14, pp. 3603–3617, 2013, doi: 10.1016/j.biomaterials.2013.01.097.

[12] K. Sugai et al., "Neural stem/progenitor cell-laden microfibers promote transplant survival in a mouse transected spinal cord injury model," Journal of Neuroscience Research, vol. 93, no. 12, pp. 1826–1838, 2015, doi: 10.1002/jnr.23636.

[13] T. L. Downing et al., "Drug-eluting microfibrous patches for the local delivery of rolipram in spinal cord repair," in Journal of Controlled Release, 2012, vol. 161, no. 3, pp. 910–917. doi: 10.1016/j.jconrel.2012.05.034.

[14] J. A. Roman, I. Reucroft, R. A. Martin, A. Hurtado, and H. Q. Mao, "Local Release of Paclitaxel from Aligned, Electrospun Microfibers Promotes Axonal Extension," Advanced Healthcare Materials, vol. 5, no. 20, pp. 2628–2635, 2016, doi: 10.1002/adhm.201600415.

[15] D. M. Thompson, A. N. Koppes, J. G. Hardy, and C. E. Schmidt, "Electrical stimuli in the central nervous system microenvironment," Annual Review of Biomedical Engineering, vol. 16, pp. 397–430, 2014, doi: 10.1146/annurev-bioeng-121813-120655.

[16] S. Hamid and R. Hayek, "Role of electrical stimulation for rehabilitation and regeneration after spinal cord injury: An overview," European Spine Journal, vol. 17, no. 9, pp. 1256–1269, 2008, doi: 10.1007/s00586-008-0729-3.

[17] R. Shi and R. B. Borgens, "Three-dimensional gradients of voltage during development of the nervous system as invisible coordinates for the establishment of embryonic pattern," Developmental Dynamics, vol. 202, no. 2, pp. 101–114, 1995, doi: 10.1002/aja.1002020202.

[18] S. Snow, K. W. Horch, and V. K. Mushahwar, "Intraspinal microstimulation using cylindrical multielectrodes," IEEE Transactions

on Biomedical Engineering, vol. 53, no. 2, pp. 311–319, 2006, doi: 10.1109/TBME.2005.857638.

[19] J. A. Bamford, R. Marc Lebel, K. Parseyan, and V. K. Mushahwar, “The fabrication, implantation, and stability of Intraspinal Microwire arrays in the spinal cord of cat and rat,” IEEE Transactions on Neural Systems and Rehabilitation Engineering, vol. 25, no. 3, pp. 287–296, 2017, doi: 10.1109/TNSRE.2016.2555959.

[20] A. Yousefpour and A. Erfanian, “A general framework for automatic closed-loop control of bladder voiding induced by intraspinal microstimulation in rats,” Scientific Reports, vol. 11, no. 1, pp. 1–16, 2021, doi: 10.1038/s41598-021-82933-7.

[21] V. Pikov, D. B. McCreery, and M. Han, “Intraspinal stimulation with a silicon-based 3D chronic microelectrode array for bladder voiding in cats,” Journal of Neural Engineering, vol. 17, no. 6, 2020, doi: 10.1088/1741-2552/abca13.

[22] M. D. Sunshine, C. N. Ganji, D. D. Fuller, and C. T. Moritz, “Respiratory resetting elicited by single pulse spinal stimulation,” Respiratory Physiology and Neurobiology, vol. 274, no. September 2019, p. 103339, 2020, doi: 10.1016/j.resp.2019.103339.

[23] “http://www.neurofibres.eu.”

[24] H. Vara and J. E. Collazos-Castro, “Enhanced spinal cord microstimulation using conducting polymer-coated carbon microfibers,” Acta Biomaterialia, vol. 90, pp. 71–86, 2019, doi: 10.1016/j.actbio.2019.03.037.

[25] A. Pegoretti, C. Della Volpe, M. Detassis, C. Migliaresi, and H. D. Wagner, “Thermomechanical behaviour of interfacial region in carbon fibre/epoxy composites,” Composites Part A: Applied Science and Manufacturing, vol. 27, no. 11, pp. 1067–1073, 1996, doi: 10.1016/1359-835X(96)00065-6.

[26] C. Della Volpe and S. Siboni, “The Wilhelmy method: A critical and practical review,” Surface Innovations, vol. 6, no. 3, pp. 120–132, 2018, doi: 10.1680/jsuin.17.00059.

[27] C. Della Volpe, D. Maniglio, M. Brugnara, S. Siboni, and M. Morra, “The solid surface free energy calculation: I. In defense of the

multicomponent approach," Journal of Colloid and Interface Science, vol. 271, no. 2, pp. 434–453, 2004, doi: 10.1016/j.jcis.2003.09.049.

[28] J. D. Reid, "Effects of flexion-extension movements of the head and spine upon the spinal cord and nerve roots," Journal of neurology, neurosurgery, and psychiatry, vol. 23, pp. 214–221, 1960, doi: 10.1136/jnnp.23.3.214.

[29] P. J. Grahn, G. W. Mallory, B. Michael Berry, J. T. Hachmann, D. A. Lobel, and J. Luis Lujan, "Restoration of motor function following spinal cord injury via optimal control of intraspinal microstimulation: Toward a next generation closed-loop neural prosthesis," Frontiers in Neuroscience, vol. 8, no. SEP. 2014. doi: 10.3389/fnins.2014.00296.

[30] M. R. Kasten, M. D. Sunshine, E. S. Secrist, P. J. Horner, and C. T. Moritz, "Therapeutic intraspinal microstimulation improves forelimb function after cervical contusion injury," Journal of Neural Engineering, vol. 10, no. 4, 2013, doi: 10.1088/1741-2560/10/4/044001.

[31] E. Fukada, "Piezoelectric properties of biological polymers," pp. 59–87, 1983.

[32] T. Yucel, P. Cebe, and D. L. Kaplan, "Structural Origins of Silk Piezoelectricity," pp. 779–785, 2011, doi: 10.1002/adfm.201002077.

[33] X. Hu, M. D. Tang-schomer, W. Huang, X. Xia, A. S. Weiss, and D. L. Kaplan, "Charge-Tunable Autoclaved Silk-Tropoelastin Protein Alloys That Control Neuron Cell Responses," pp. 3875–3884, 2013, doi: 10.1002/adfm.201202685.

[34] L. Valentini, B. Bon, and N. M. Pugno, "RSC Advances Ice-regenerated fl ame retardant and robust fi lm of," pp. 9063–9069, 2018, doi: 10.1039/c7ra13708g.

[35] D. R. Nisbet, K. E. Crompton, M. K. Horne, D. I. Finkelstein, and J. S. Forsythe, "Neural tissue engineering of the CNS using hydrogels," Journal of Biomedical Materials Research - Part B Applied Biomaterials, vol. 87, no. 1, pp. 251–263, 2007, doi: 10.1002/jbm.b.31000.

[36] E. Servoli, D. Maniglio, A. Motta, and C. Migliaresi, “Folding and Assembly of Fibroin Driven by an AC Electric Field : Effects on Film Properties,” pp. 827–835, doi: 10.1002/mabi.200800057.

[37] N. B. Jain et al., “Traumatic spinal cord injury in the United States, 1993-2012,” Journal of the American Medical Association, vol. 313, no. 22, pp. 2236–2243, 2015, doi: 10.1001/jama.2015.6250.

[38] H. Huang et al., “Clinical Neurorestorative Therapeutic Guidelines for Spinal Cord Injury (IANR/CANR version 2019),” Journal of Orthopaedic Translation, vol. 20, no. November 2019, pp. 14–24, 2020, doi: 10.1016/j.jot.2019.10.006.

[39] M. Bonnet, O. Alluin, T. Trimaille, D. Gigmes, T. Marqueste, and P. Decherchi, “Delayed Injection of a Physically Cross-Linked PNIPAAm-g-PEG Hydrogel in Rat Contused Spinal Cord Improves Functional Recovery,” ACS Omega, vol. 5, no. 18, pp. 10247–10259, 2020, doi: 10.1021/acsomega.9b03611.

[40] M. A. Kopp et al., “SCISSOR - Spinal Cord Injury Study on Small molecule-derived Rho inhibition: A clinical study protocol,” BMJ Open, vol. 6, no. 7, pp. 1–16, 2016, doi: 10.1136/bmjopen-2015-010651.

[41] R. C. Cornelison et al., “Injectable hydrogels of optimized acellular nerve for injection in the injured spinal cord,” Biomedical Materials, vol. 13, no. 3, pp. 1–14, 2018, doi: https://doi.org/10.1088/1748-605X/aaab82.

[42] A. Higuchi et al., “Biomaterials used in stem cell therapy for spinal cord injury,” Progress in Materials Science, vol. 103, no. 32, pp. 374–424, 2019, doi: 10.1016/j.pmatsci.2019.02.002.

[43] T. Führmann, P. N. Anandakumaran, and M. S. Shoichet, “Combinatorial Therapies After Spinal Cord Injury: How Can Biomaterials Help?,” Advanced Healthcare Materials, vol. 6, no. 10. p. 1601130, 2017. doi: 10.1002/adhm.201601130.

[44] M. A. Brimble and M. S. Levi, “A Review of Neuroprotective Agents,” Frontiers in Medicinal Chemistry, vol. 163, no. 194, pp. 163–194, 2006, doi: 10.2174/978160805206610603010163.

[45] J. F. Borisoff et al., “Suppression of Rho-kinase activity promotes axonal growth on inhibitory CNS substrates,” Molecular and

Cellular Neuroscience, vol. 22, no. 3, pp. 405–416, 2003, doi: 10.1016/S1044-7431(02)00032-5.

[46] J. T. Wilcox, D. Cadotte, and M. G. Fehlings, "Spinal cord clinical trials and the role for bioengineering," Neuroscience Letters, vol. 519, no. 2, pp. 93–102, 2012, doi: 10.1016/j.neulet.2012.02.028.

[47] W. Tetzlaff et al., "A Systematic Review of Cellular Transplantation Therapies for Spinal Cord Injury," Journal Of Neurotrauma, vol. 28, no. 8, pp. 1611–1682, 2011, doi: https://doi.org/10.1089/neu.2009.1177.

[48] K. T. Wright, W. El Masri, A. Osman, J. Chowdhury, and W. E. B. Johnson, "Concise review: Bone marrow for the treatment of spinal cord injury: Mechanisms and clinical applications," Stem Cells, vol. 29, no. 2, pp. 169–178, 2011, doi: 10.1002/stem.570.

[49] M. Tsintou, K. Dalamagkas, and A. M. Seifalian, "Advances in regenerative therapies for spinal cord injury: A biomaterials approach," Neural Regeneration Research, vol. 10, no. 5, pp. 726–742, 2015, doi: 10.4103/1673-5374.156966.

[50] A. Tuladhar et al., "Injectable hydrogel enables local and sustained co-delivery to the brain: Two clinically approved biomolecules, cyclosporine and erythropoietin, accelerate functional recovery in rat model of stroke," Biomaterials, vol. 235, p. 119794, 2020, doi: 10.1016/j.biomaterials.2020.119794.

[51] D. Macaya and M. Spector, "Injectable hydrogel materials for spinal cord regeneration: A review," Biomedical Materials, vol. 7, no. 1, p. 012001, 2012, doi: 10.1088/1748-6041/7/1/012001.

[52] Z. Z. Khaing, A. Ehsanipour, C. P. Hofstetter, and S. K. Seidlits, "Injectable Hydrogels for Spinal Cord Repair: A Focus on Swelling and Intraspinal Pressure," Cells, Tissues, Organs, vol. 202, no. 1–2. S. Karger AG, pp. 67–84, Oct. 01, 2016. doi: 10.1159/000446697.

[53] S. Okada, "The pathophysiological role of acute inflammation after spinal cord injury," Inflammation and Regeneration, vol. 36, no. 1, p. 20, 2016, doi: 10.1186/s41232-016-0026-1.

[54] M. B. Orr and J. C. Gensel, "Spinal Cord Injury Scarring and Inflammation: Therapies Targeting Glial and Inflammatory

Responses," Neurotherapeutics, vol. 15, no. 3, pp. 541–553, 2018, doi: 10.1007/s13311-018-0631-6.

[55] H. Lee, R. J. McKeon, and R. V. Bellamkonda, "Sustained delivery of thermostabilized chABC enhances axonal sprouting and functional recovery after spinal cord injury," Proceedings of the National Academy of Sciences, vol. 107, no. 8, pp. 3340–3345, 2010, doi: 10.1073/pnas.0905437106.

[56] A. P. Tran, P. M. Warren, and J. Silver, "The biology of regeneration failure and success after spinal cord injury," Physiological Reviews, vol. 98, no. 2, pp. 881–917, 2018, doi: 10.1152/physrev.00017.2017.

[57] M. Azizi et al., "ChABC-loaded PLGA nanoparticles: A comprehensive study on biocompatibility, functional recovery, and axonal regeneration in animal model of spinal cord injury," International Journal of Pharmaceutics, vol. 577, p. 119037, 2020, doi: 10.1016/j.ijpharm.2020.119037.

[58] R. Shechter et al., "Recruitment of Beneficial M2 Macrophages to Injured Spinal Cord Is Orchestrated by Remote Brain Choroid Plexus," Immunity, vol. 38, no. 3, pp. 555–569, Mar. 2013, doi: 10.1016/j.immuni.2013.02.012.

[59] P. Solár, A. Zamani, L. Kubíčková, P. Dubový, and M. Joukal, "Choroid plexus and the blood-cerebrospinal fluid barrier in disease," Fluids and Barriers of the CNS, vol. 17, pp. 1–29, 2020, doi: 10.1186/s12987-020-00196-2.

[60] R. M. Ransohoff, P. Kivisäkk, and G. Kidd, "Three or more routes for leukocyte migration into the central nervous system," Nature Reviews Immunology, vol. 3, no. 7, pp. 569–581, 2003, doi: 10.1038/nri1130.

[61] L. Arnold et al., "Inflammatory monocytes recruited after skeletal muscle injury switch into antiinflammatory macrophages to support myogenesis," Journal of Experimental Medicine, vol. 204, no. 5, pp. 1057–1069, 2007, doi: 10.1084/jem.20070075.

[62] L. Filli et al., "Bridging the gap: A reticulo-propriospinal detour bypassing an incomplete spinal cord injury," Journal of Neuroscience,

vol. 34, no. 40, pp. 13399–13410, 2014, doi: 10.1523/JNEUROSCI.0701-14.2014.

[63] M. S. Beattie et al., “Endogenous Repair after Spinal Cord Contusion Injuries in the Rat,” Experimental Neurology, vol. 148, no. 2, pp. 453–463, 1997, doi: 10.1006/exnr.1997.6695.

[64] Q. Wang et al., “A Thermosensitive heparin-poloxamer hydrogel bridges aFGF to treat spinal cord injury,” ACS Applied Materials and Interfaces, vol. 9, no. 8, pp. 6725–6745, 2017, doi: 10.1021/acsami.6b13155.

[65] H. Z. Hu, N. Granger, S. Balakrishna Pai, R. V. Bellamkonda, and N. D. Jeffery, “Therapeutic efficacy of microtube-embedded chondroitinase ABC in a canine clinical model of spinal cord injury,” Brain, vol. 141, no. 4, pp. 1017–1027, 2018, doi: 10.1093/brain/awy007.

[66] Z. Hassannejad, A. S. Zadegan, A. R. Vaccaro, V. Rahimi-Movaghar, and O. Sabzevari, “Biofunctionalized peptide-based hydrogel as an injectable scaffold for BDNF delivery can improve regeneration after spinal cord injury,” Injury, vol. 50, no. 2, pp. 278–285, 2019, doi: 10.1016/j.injury.2018.12.027.

[67] D. Cigognini, D. Silva, S. Paloppi, and F. Gelain, “Evaluation of mechanical properties and therapeutic effect of injectable self-assembling hydrogels for spinal cord injury,” Journal of Biomedical Nanotechnology, vol. 10, no. 2, pp. 309–323, 2014, doi: 10.1166/jbn.2014.1759.

[68] V. M. Tysseling et al., “Self-assembling peptide amphiphile promotes plasticity of serotonergic fibers following spinal cord injury,” Journal of Neuroscience Research, vol. 88, no. 14, pp. 3161–3170, 2010, doi: 10.1002/jnr.22472.

[69] M. Sever-Bahcekapili et al., “Neuroactive Peptide Nanofibers for Regeneration of Spinal Cord after Injury,” Macromolecular Bioscience, pp. 1–9, 2020, doi: 10.1002/mabi.202000234.

[70] D. Macaya and M. Spector, “Injectable hydrogel materials for spinal cord regeneration: A review,” Biomedical Materials, vol. 7, no. 1, 2012, doi: 10.1088/1748-6041/7/1/012001.

[71] “Neurofibres.” https://cordis.europa.eu/project/id/732344

[72] M. C. Joo et al., “Effect of electrical stimulation on neural regeneration via the p38-RhoA and ERK1/2-Bcl-2 pathways in spinal cord-injured rats,” Neural Regeneration Research, vol. 13, no. 2, p. 340, 2018, doi: 10.4103/1673-5374.226404.

[73] H. Vara and J. E. Collazos-Castro, “Enhanced spinal cord microstimulation using conducting polymer-coated carbon microfibers,” Acta Biomaterialia, vol. 90, pp. 71–86, 2019, doi: 10.1016/j.actbio.2019.03.037.

[74] K. H. Lee, K. Chung, J. M. Chung, and R. E. Coggeshall, “Correlation of cell body size, axon size, and signal conduction velocity for individually labelled dorsal root ganglion cells in the cat,” Journal of Comparative Neurology, vol. 243, no. 3, pp. 335–346, 1986, doi: 10.1002/cne.902430305.

[75] H. Vara and J. E. Collazos-Castro, “Biofunctionalized Conducting Polymer/Carbon Microfiber Electrodes for Ultrasensitive Neural Recordings,” ACS Applied Materials and Interfaces, vol. 7, no. 48, pp. 27016–27026, 2015, doi: 10.1021/acsami.5b09594.

[76] P. Zhuang, A. X. Sun, J. An, C. K. Chua, and S. Y. Chew, “3D neural tissue models: From spheroids to bioprinting,” Biomaterials, vol. 154, pp. 113–133, 2018, doi: 10.1016/j.biomaterials.2017.10.002.

[77] T. Führmann et al., “Injectable hydrogel promotes early survival of induced pluripotent stem cell-derived oligodendrocytes and attenuates longterm teratoma formation in a spinal cord injury model,” Biomaterials, vol. 83, pp. 23–36, 2016, doi: 10.1016/j.biomaterials.2015.12.032.

[78] I. Vismara et al., “Selective Modulation of A1 Astrocytes by Drug-Loaded Nano-Structured Gel in Spinal Cord Injury,” ACS Nano, vol. 14, no. 1, pp. 360–371, 2020, doi: 10.1021/acsnano.9b05579.

[79] C. Wang et al., “An injectable heparin-Laponite hydrogel bridge FGF4 for spinal cord injury by stabilizing microtubule and improving mitochondrial function,” Theranostics, vol. 9, no. 23, pp. 7016–7032, 2019, doi: 10.7150/thno.37601.

[80] L. T. A. Hong et al., “An injectable hydrogel enhances tissue repair after spinal cord injury by promoting extracellular matrix

remodeling," Nature Communications, vol. 8, no. 1, pp. 1–14, 2017, doi: 10.1038/s41467-017-00583-8.

[81] M. Boido, M. Ghibaudi, P. Gentile, E. Favaro, R. Fusaro, and C. Tonda-Turo, "Chitosan-based hydrogel to support the paracrine activity of mesenchymal stem cells in spinal cord injury treatment," Scientific Reports, vol. 9, no. 1, pp. 1–16, 2019, doi: 10.1038/s41598-019-42848-w.

[82] X. L. Li et al., "A single dose of thermal-sensitive biodegradable hybrid hydrogel promotes functional recovery after spinal cord injury," Applied Materials Today, vol. 14, pp. 66–75, 2019, doi: 10.1016/j.apmt.2018.10.007.

[83] I. Elliott Donaghue, C. H. Tator, and M. S. Shoichet, "Sustained delivery of bioactive neurotrophin-3 to the injured spinal cord," Biomaterials Science, vol. 3, no. 1, pp. 65–72, 2015, doi: 10.1039/c4bm00311j.

[84] C. E. Kang, M. D. Baumann, C. H. Tator, and M. S. Shoichet, "Localized and sustained delivery of fibroblast growth factor-2 from a nanoparticle-hydrogel composite for treatment of spinal cord injury," Cells Tissues Organs, vol. 197, no. 1, pp. 55–63, 2012, doi: 10.1159/000339589.

[85] E. Ansorena et al., "Injectable alginate hydrogel loaded with GDNF promotes functional recovery in a hemisection model of spinal cord injury," International Journal of Pharmaceutics, vol. 455, no. 1–2, pp. 148–158, 2013, doi: 10.1016/j.ijpharm.2013.07.045.

[86] A. Jain, R. J. McKeon, S. M. Brady-Kalnay, and R. V. Bellamkonda, "Sustained delivery of activated rho GTPases and BDNF promotes axon growth in CSPG-rich regions following spinal cord injury," PLoS ONE, vol. 6, no. 1, p. e16135, 2011, doi: 10.1371/journal.pone.0016135.

[87] S. Chen et al., "Construction of injectable silk fibroin/polydopamine hydrogel for treatment of spinal cord injury," Chemical Engineering Journal, vol. 399, p. 125795, 2020, doi: 10.1016/j.cej.2020.125795.

[88] X. Li et al., "The effect of a nanofiber-hydrogel composite on neural tissue repair and regeneration in the contused spinal cord,"

Biomaterials, vol. 245, no. March, p. 119978, 2020, doi: 10.1016/j.biomaterials.2020.119978.

[89] C. Wang, H. Yue, Q. Feng, B. Xu, L. Bian, and P. Shi, “Injectable Nanoreinforced Shape-Memory Hydrogel System for Regenerating Spinal Cord Tissue from Traumatic Injury,” ACS Applied Materials and Interfaces, vol. 10, no. 35, pp. 29299–29307, 2018, doi: 10.1021/acsami.8b08929.

[90] Z. Z. Khaing et al., “Localized and sustained release of brain-derived neurotrophic factor from injectable hydrogel/microparticle composites fosters spinal learning after spinal cord injury,” Journal of Materials Chemistry B, vol. 4, no. 47, pp. 7560–7571, 2016, doi: 10.1039/C6TB01602B.

[91] Z. Nazemi et al., “Co-delivery of minocycline and paclitaxel from injectable hydrogel for treatment of spinal cord injury,” Journal of Controlled Release, vol. 321, pp. 145–158, 2020, doi: 10.1016/j.jconrel.2020.02.009.

[92] L. M. Marquardt et al., “Designer , injectable gels to prevent transplanted Schwann cell loss during spinal cord injury therapy,” Science advances, vol. 6, no. 14, p. eaaz1039, 2020, doi: 10.1126/sciadv.aaz1039.

[93] S. Tavakol et al., “Self-Assembling Peptide Nanofiber Containing Long Motif of Laminin Induces Neural Differentiation, Tubulin Polymerization, and Neurogenesis: In Vitro, Ex Vivo, and In Vivo Studies,” Molecular Neurobiology, vol. 53, no. 8, pp. 5288–5299, 2016, doi: 10.1007/s12035-015-9448-z.

[94] K. Zweckberger, Y. Liu, J. Wang, N. Forgione, and M. G. Fehlings, “Synergetic use of neural precursor cells and self-assembling peptides in experimental cervical spinal cord injury,” Journal of Visualized Experiments, vol. 96, p. e52105, 2015, doi: 10.3791/52105.

[95] J. Ye et al., “Using primate neural stem cells cultured in self-assembling peptide nanofiber scaffolds to repair injured spinal cords in rats,” Spinal Cord (2016), vol. 54, pp. 933–941, 2016, doi: 10.1038/sc.2016.36.

[96] K. A. Tran, P. P. Partyka, Y. Jin, J. Bouyer, I. Fischer, and P. A. Galie, “Vascularization of self-assembled peptide scaffolds for

spinal cord injury repair," Acta Biomaterialia, vol. 104, pp. 76–84, 2020, doi: 10.1016/j.actbio.2019.12.033.

[97] D. Cigognini, A. Satta, B. Colleoni, D. Silva, and M. Donega, "Evaluation of Early and Late Effects into the Acute Spinal Cord Injury of an Injectable Functionalized Self- Assembling Scaffold," PLoS ONE, vol. 6, no. 5, p. e19782, 2011, doi: 10.1371/journal.pone.0019782.

[98] Y. Sun et al., "Functional Self-Assembling Peptide Nano fiber Hydrogels Designed for Nerve Degeneration," ACS Applied Materials and Interfaces, vol. 8, no. 3, p. 2348−2359, 2016, doi: 10.1021/acsami.5b11473.

[99] Y. Zhang, L. Li, J. Mu, J. Chen, S. Feng, and J. Gao, "Implantation of a functional TEMPO-hydrogel induces recovery from rat spinal cord transection through promoting nerve regeneration and protecting bladder tissue," Biomaterials Science, vol. 8, no. 6, pp. 1695–1701, 2020, doi: 10.1039/c9bm01530b.

[100] D. Gupta, C. H. Tator, and M. S. Shoichet, "Fast-gelling injectable blend of hyaluronan and methylcellulose for intrathecal, localized delivery to the injured spinal cord," Biomaterials, vol. 27, no. 11, pp. 2370–2379, 2006, doi: 10.1016/j.biomaterials.2005.11.015.

[101] B. H. Lee, Y. M. Lee, Y. S. Sohn, and S. C. Song, "A thermosensitive poly(organophosphazene) gel," Macromolecules, vol. 35, no. 10, pp. 3876–3879, 2002, doi: 10.1021/ma012093q.

[102] Y. Liang, X. Zhao, T. Hu, Y. Han, and B. Guo, "Mussel-inspired, antibacterial, conductive, antioxidant, injectable composite hydrogel wound dressing to promote the regeneration of infected skin," Journal of Colloid and Interface Science, vol. 556, pp. 514–528, 2019, doi: 10.1016/j.jcis.2019.08.083.

[103] S. Van Vlierberghe, P. Dubruel, and E. Schacht, "Biopolymer-based hydrogels as scaffolds for tissue engineering applications: A review," Biomacromolecules, vol. 12, no. 5, pp. 1387–1408, 2011, doi: 10.1021/bm200083n.

[104] L. Klouda, "Thermoresponsive hydrogels in biomedical applications A seven-year update," European Journal of Pharmaceutics

and Biopharmaceutics, vol. 97, pp. 338–349, 2015, doi: 10.1016/j.ejpb.2015.05.017.

[105] N. Comolli, B. Neuhuber, I. Fischer, and A. Lowman, “In vitro analysis of PNIPAAm-PEG, a novel, injectable scaffold for spinal cord repair,” Acta Biomaterialia, vol. 5, no. 4, pp. 1046–1055, 2009, doi: 10.1016/j.actbio.2008.10.008.

[106] L. Cai, R. E. Dewi, and S. C. Heilshorn, “Injectable hydrogels with in situ double network formation enhance retention of transplanted stem cells,” Advanced Functional Materials, vol. 25, no. 9, pp. 1344–1351, 2015, doi: 10.1002/adfm.201403631.

[107] C. Zhang et al., “Nanoparticles guided precise transplantation of varying numbers of mesenchimal stem cells into post-traumatic syrinx in spinal cord injury rat,” Bulletin of Russian State Medical University, vol. 6, pp. 49–56, 2018, doi: 10.24075/brsmu.2018.084.

[108] X. Li et al., “The effect of a nanofiber-hydrogel composite on neural tissue repair and regeneration in the contused spinal cord,” Biomaterials, vol. 245, no. March, p. 119978, 2020, doi: 10.1016/j.biomaterials.2020.119978.

[109] X. Li et al., “Nanofiber-hydrogel composite–mediated angiogenesis for soft tissue reconstruction,” Science Translational Medicine, vol. 11, no. 490, pp. 1–12, 2019, doi: 10.1126/scitranslmed.aau6210.

[110] G. A. Silva et al., “Selective Differentiation of Neural Progenitor Cells by High-Epitope Density Nanofibers,” Science, vol. 303, no. 5662, pp. 1352–1355, 2004, doi: 10.1126/science.1093783.

[111] V. M. Tysseling-Mattiace et al., “Self-assembling nanofibers inhibit glial scar formation and promote axon elongation after spinal cord injury,” Journal of Neuroscience, vol. 28, no. 14, pp. 3814–3823, 2008, doi: 10.1523/JNEUROSCI.0143-08.2008.

[112] F. Gelain, D. Bottai, A. Vescovi, and S. Zhang, “Designer self-assembling peptide nanofiber scaffolds for adult mouse neural stem cell 3-dimensional cultures,” PLoS ONE, vol. 1, no. 1, p. e119, 2006, doi: 10.1371/journal.pone.0000119.

[113] Z. X. Zhang, Q. X. Zheng, Y. C. Wu, and D. J. Hao, “Compatibility of neural stem cells with functionalized selfassembling

peptide scaffold in vitro,” Biotechnology and Bioprocess Engineering, vol. 15, no. 4, pp. 545–551, 2010, doi: 10.1007/s12257-009-3076-2.

[114] T. Cheriyan et al., “Spinal cord injury models: A review,” Spinal Cord, vol. 52, no. 8, pp. 588–595, 2014, doi: 10.1038/sc.2014.91.

[115] V. Krishna et al., “A contusion model of severe spinal cord injury in rats.,” Journal of visualized experiments, no. 78, p. e50111, 2013, doi: 10.3791/50111.

[116] J. A. Gruner, “A Monitored Contusion Model of Spinal Cord Injury in the Rat,” Journal of Neurotrauma, vol. 9, no. 2, pp. 123–128, 1992, doi: 10.1089/neu.1992.9.123.

[117] N. L. Banik, J. M. Powers, and E. L. Hogan, “The Effects of Spinal Cord Trauma on Myelin,” Journal of Neuropathology & Experimental Neurology, vol. 39, no. 3, pp. 232–244, 1980, doi: doi.org/10.1097/00005072-198005000-00002.

[118] A. R. Blight and V. Decrescito, “Morphometric analysis of experimental spinal cord injury in the cat: The relation of injury intensity to survival of myelinated axons,” Neuroscience, vol. 19, no. 1, pp. 321–341, 1986, doi: 10.1016/0306-4522(86)90025-4.

[119] W. Young, “Spinal cord contusion models,” in Progress in Brain Research, vol. 137, 2002, pp. 231–255. doi: 10.1016/S0079-6123(02)37019-5.

[120] W. Qin et al., “Wallerian degeneration in central nervous system: Dynamic associations between diffusion indices and their underlying pathology,” PLoS ONE, vol. 7, no. 7, p. e41441, 2012, doi: 10.1371/journal.pone.0041441.

[121] I. Paterniti, E. Esposito, and S. Cuzzocrea, “An in vivo compression model of spinal cord injury,” in Neurotrophic Factors, New York, NY: Humana Press, 2018, pp. 379–384. doi: 10.1007/978-1-4939-7571-6_29.

[122] X. Li et al., “Scaffold-facilitated locomotor improvement post complete spinal cord injury: Motor axon regeneration versus endogenous neuronal relay formation,” Biomaterials, vol. 197, pp. 20–31, 2019, doi: 10.1016/j.biomaterials.2019.01.012.

[123] R. U. Ahmed, M. Alam, and Y. P. Zheng, “Experimental spinal cord injury and behavioral tests in laboratory rats,” Heliyon, vol. 5, no. 3, p. e01324, 2019, doi: 10.1016/j.heliyon.2019.e01324.

[124] L. Slovinska, J. Blasko, M. Nagyova, E. Szekiova, and D. Cizkova, “In Vitro Models of Spinal Cord Injury,” in Recovery of Motor Function Following Spinal Cord Injury, IntechOpen, Ed. InTech, 2016. doi: 10.5772/63459.

[125] J. Ganz et al., “Implantation of 3D constructs embedded with oral mucosa-derived cells induces functional recovery in rats with complete spinal cord transection,” Frontiers in Neuroscience, vol. 11, p. 589, 2017, doi: 10.3389/fnins.2017.00589.

[126] K. Fouad, C. Hurd, and D. S. K. Magnuson, “Functional testing in animal models of spinal cord injury: Not as straight forward as one would think,” Frontiers in Integrative Neuroscience, vol. 7, p. 85, 2013, doi: 10.3389/fnint.2013.00085.

[127] S. Pandamooz et al., “Modeling traumatic injury in organotypic spinal cord slice culture obtained from adult rat,” Tissue and Cell, vol. 56, pp. 90–97, 2019, doi: 10.1016/j.tice.2019.01.002.

[128] M. Tadie et al., “Partial return of motor function in paralyzed legs after surgical bypass of the lesion site by nerve autografts three years after spinal cord injury,” Journal of Neurotrauma, vol. 19, no. 8, pp. 909–916, 2002, doi: 10.1089/089771502320317069.

[129] K. R. Ko and J. P. Frampton, “Developments in 3D neural cell culture models: the future of neurotherapeutics testing?,” Expert Review of Neurotherapeutics, vol. 16, no. 7, pp. 739–741, 2016, doi: 10.1586/14737175.2016.1166053.

[130] A. V. Krassioukov, A. Ackery, G. Schwartz, Y. Adamchik, Y. Liu, and M. G. Fehlings, “An in vitro model of neurotrauma in organotypic spinal cord cultures from adult mice,” Brain Research Protocols, vol. 10, no. 2, pp. 60–68, 2002, doi: 10.1016/S1385-299X(02)00180-0.

[131] F. Donnelly, “Regulatory Science Regulatory Science as a Means to Respond to EU Healthcare Challenges and Global Market Needs,” Journal of Regulatory Science, vol. 4, no. 4, pp. 21–28, 2016, doi: https://doi.org/10.21423/jrs-v04n04p021.

[132] C.-W. Chiu, H. Cheng, and S.-L. Hsieh, “Contusion Spinal Cord Injury Rat Model,” Bio-Protocol, vol. 7, no. 12, pp. 1–8, 2017, doi: 10.21769/bioprotoc.2337.

[133] J. A. Bamford and V. K. Mushahwar, “Intraspinal microstimulation for the recovery of function following spinal cord injury,” Progress in Brain Research, vol. 194, pp. 227–239, 2011, doi: 10.1016/B978-0-444-53815-4.00004-2.Intraspinal.

[134] K. L. Johnson, Contact mechanics. Cambridge university press, 1987.

[135] N. M. Pugno and A. Carpinteri, “Tubular Adhesive Joints Under Axial Load,” Journal of Applied Mechanics, vol. 70, pp. 832–839, 2003, doi: 10.1115/1.1604835.

[136] P. S. Motta and J. W. Judy, “Multielectrode microprobes for deep-brain stimulation fabricated with a customizable 3-D electroplating process,” IEEE Transactions on Biomedical Engineering, vol. 52, no. 5, pp. 923–933, 2005, doi: 10.1109/TBME.2005.845225.

[137] D. Budai, “Carbon fiber-based microelectrodes and microbiosensors,” in Intelligent and Biosensors, 2010, pp. 269–288.

[138] A. Fabbro et al., “Graphene-Based interfaces do not alter target nerve cells,” ACS Nano, vol. 10, no. 1, pp. 615–623, 2016, doi: 10.1021/acsnano.5b05647.

[139] T. F. Tadros, “11. Wetting and spreading,” Interfacial Phenomena and Colloid Stability, no. i, pp. 247–276, 2015, doi: 10.1515/9783110283433-012.

[140] R. J. Good and C. J. van Oss, “The modern theory of contact angles and the hydrogen bond components of surface energies,” in Modern approaches to wettability, Springer, Ed. 1992, pp. 1–27.

[141] Q. Yuan, L. Dougherty, and S. S. Margulies, “In Vivo Human Cervical Spinal Cord Deformation and Displacement in Flexion,” Spine, vol. 23, no. 15, pp. 1677–1683, 1998.

[142] S. Santi, I. Corridori, N. M. Pugno, A. Motta, and C. Migliaresi, “Injectable Scaffold-Systems for the Regeneration of Spinal Cord: Advances of the Past Decade,” ACS Biomaterials Science and

Engineering, vol. 7, no. 3, pp. 983–999, 2021, doi: 10.1021/acsbiomaterials.0c01779.

[143] M. D. Norenberg, J. Smith, and A. Marcillo, “The Pathology of Human Spinal Cord Injury: Defining the Problems,” Journal of Neurotrauma, vol. 21, no. 4, pp. 429–440, 2004, doi: 10.1089/089771504323004575.

[144] N. Seringec, G. Guncu, O. Arihan, N. Avcu, and N. Dikmenoglu, “Investigation of hemorheological parameters in periodontal diseases,” Clinical Hemorheology and Microcirculation, vol. 61, no. 1, pp. 47–58, 2015, doi: 10.3233/CH-141892.

[145] A. Toossi, D. G. Everaert, A. Azar, C. R. Dennison, and V. K. Mushahwar, “Mechanically Stable Intraspinal Microstimulation Implants for Human Translation,” Annals of Biomedical Engineering, vol. 45, no. 3, pp. 681–694, 2017, doi: 10.1007/s10439-016-1709-0.

[146] S. Viljoen et al., “Apparatus for simulating dynamic interactions between the spinal cord and soft-coupled intradural implants,” Review of Scientific Instruments, vol. 84, no. 11. 2013. doi: 10.1063/1.4831801.

[147] C. A. Schneider, W. S. Rasband, and K. W. Eliceiri, “NIH Image to ImageJ: 25 years of image analysis,” Nature Methods, vol. 9, no. 7, pp. 671–675, 2012, doi: 10.1038/nmeth.2089.

[148] M. D. Norenberg, J. Smith, and A. Marcillo, “The Pathology of Human Spinal Cord Injury: Defining the Problems,” Journal of Neurotrauma, vol. 21, no. 4, pp. 429–440, 2004, doi: 10.1089/089771504323004575.

[149] K. H. Lee, K. Chung, J. M. Chung, and R. E. Coggeshall, “Correlation of cell body size, axon size, and signal conduction velocity for individually labelled dorsal root ganglion cells in the cat,” Journal of Comparative Neurology, vol. 243, no. 3, pp. 335–346, 1986, doi: 10.1002/cne.902430305.

[150] P. Zhuang, A. X. Sun, J. An, C. K. Chua, and S. Y. Chew, “3D neural tissue models: From spheroids to bioprinting,” Biomaterials, vol. 154, pp. 113–133, 2018, doi: 10.1016/j.biomaterials.2017.10.002.

[151] M. C. Joo et al., “Effect of electrical stimulation on neural regeneration via the p38-RhoA and ERK1/2-Bcl-2 pathways in spinal

cord-injured rats," Neural Regeneration Research, vol. 13, no. 2, p. 340, 2018, doi: 10.4103/1673-5374.226404.

[152] C. Ribeiro, V. Sencadas, D. M. Correia, and S. Lanceros-Méndez, "Piezoelectric polymers as biomaterials for tissue engineering applications," Colloids and Surfaces B: Biointerfaces, vol. 136, pp. 46–55, 2015, doi: 10.1016/j.colsurfb.2015.08.043.

[153] B. Kundu, R. Rajkhowa, S. C. Kundu, and X. Wang, "Silk fi broin biomaterials for tissue regenerations ☆," Advanced Drug Delivery Reviews, vol. 65, no. 4, pp. 457–470, 2013, doi: 10.1016/j.addr.2012.09.043.

[154] E. Carletti, A. Motta, and C. Migliaresi, "Scaffolds for Tissue Engineering and 3D Cell Culture," in 3D Cell Culture: Methods and Protocols, Methods in Molecular Biology, 2011, pp. 17–39. doi: 10.1007/978-1-60761-984-0.

[155] M. Floren, C. Migliaresi, and A. Motta, "Processing Techniques and Applications of Silk Hydrogels in Bioengineering," Journal of Functional Biomaterials, vol. 7, no. 3, p. 26, 2016, doi: 10.3390/jfb7030026.

[156] Y. S. Zhang and A. Khademhosseini, "Advances in engineering hydrogels," Science, vol. 356, no. 6337, 2017, doi: 10.1126/science.aaf3627.

[157] J. M. Oliveira et al., "Hydrogel-based scaffolds to support intrathecal stem cell transplantation as a gateway to the spinal cord: clinical needs, biomaterials, and imaging technologies," npj Regenerative Medicine, vol. 3, no. 1, pp. 1–9, 2018, doi: 10.1038/s41536-018-0046-3.

[158] U. J. Kim, J. Park, C. Li, H. J. Jin, R. Valluzzi, and D. L. Kaplan, "Structure and properties of silk hydrogels," Biomacromolecules, vol. 5, no. 3, pp. 786–792, 2004, doi: 10.1021/bm0345460.

[159] A. Zuluaga-Vélez, D. F. Cómbita-Merchán, R. Buitrago-Sierra, J. F. Santa, E. Aguilar-Fernández, and J. C. Sepúlveda-Arias, "Silk fibroin hydrogels from the Colombian silkworm *Bombyx mori* L: Evaluation of physicochemical properties," PLoS ONE, vol. 14, no. 3, pp. 1–16, 2019, doi: 10.1371/journal.pone.0213303.

[160] M. Floren, W. Bonani, A. Dharmarajan, A. Motta, C. Migliaresi, and W. Tan, “Human mesenchymal stem cells cultured on silk hydrogels with variable stiffness and growth factor differentiate into mature smooth muscle cell phenotype,” Acta Biomaterialia, vol. 31, pp. 156–166, 2016, doi: 10.1016/j.actbio.2015.11.051.

[161] C. A. Schneider, W. S. Rasband, and K. W. Eliceiri, “NIH Image to ImageJ: 25 years of image analysis,” Nature Methods, vol. 9, no. 7, pp. 671–675, 2012, doi: 10.1038/nmeth.2089.

Credits of the cover image: Ilaria Corridori.

University of Trento
Doctoral School in Civil, Environmental and Mechanical Engineering
http://web.unitn.it/en/dricam
Via Mesiano 77, I-38123 Trento
Tel. +39 0461 282670 / 2611 - *dicamphd@unitn.it*

Spinal cord injury causes the partial or total loss of the anatomical and functional continuity of the spinal cord tissue, leading to the damage of the organs controlled by nerves that branch off downstream the injury.

This thesis analyses the mechanics of two possible treatments based on two different approaches: intraspinal microstimulation (ISMS) and tissue engineering. These two approaches have a common rationale, the delivery of electrical stimuli to the injured spinal cord. In the literature, the feasibility of the electrodes for ISMS is often limited to the analysis of stiffness. The mechanical validation of the device is then focused on the step after the *in vivo* implantation, considering the interplay with the surrounding tissue.

In this work, the mechanical performance of an innovative intraspinal microstimulation device is evaluated thoroughly before the *in vivo* step, to avoid the waste of material, animals, and time. The study involves the characterisation of the single components (electrodes), prototypes, and possible failure mechanisms.

A work on silk fibroin hydrogels for the regeneration of the spinal cord is also presented. Silk fibroin is a highly versatile material for biomedical purposes, and thus largely used in tissue engineering. Moreover, it has piezolectric properties subjected to micro and nanostructure. Given the proven benefits of electrical stimulation in the regeneration of the spinal cord after injury, different approaches studied in literature often require the use of external devices to generate electrical stimuli. This thesis aims to study the mechanical properties of silk fibroin hydrogels obtained by applying an electric field to silk fibroin solutions, to investigate the eventual increase of the microstructure orientation and consequent improvement of the piezoelectric effects of fibroin.

Ilaria Corridori has a Master of Biomedical Engineering and is a Ph.D. student in the Laboratory for Bioinspired, Bionic, Nano, Meta Materials & Mechanics at the University of Trento, Italy. She is currently working on the FET Horizon 2020 project "Neurofibres", focusing on the mechanical characterisation of an intraspinal microstimulation device for the treatment of spinal cord injury. She is also involved in the study of silk fibroin hydrogels as scaffolds for the regeneration of the central nervous tissue.